On the influence of turbulent inflow conditions on the wakes of floating offshore wind turbines

Author:
Michael Janssen
DTU Wind-M-0771
July 2024

Author:
Michael Janssen

Title:
On the influence of turbulent inflow conditions on the wake of floating offshore wind turbines

DTU Wind-M-0771
July 2024

ECTS: 45

Education: Master of Science

Supervisors:

Søren Juhl Andersen
DTU Wind & Energy Systems

Axelle Viré
TUDelft

Remarks:
This report is submitted as partial fulfillment of the requirements for graduation in the above education at the Technical University of Denmark.

DTU Wind & Energy Systems is a department of the Technical University of Denmark with a unique integration of research, education, innovation and public/private sector consulting in the field of wind energy. Our activities develop new opportunities and technology for the global and Danish exploitation of wind energy. Research focuses on key technical-scientific fields, which are central for the development, innovation and use of wind energy and provides the basis for advanced education at the education.

Technical University of Denmark Department of Wind Energy Frederiksborgvej 399
4000 Roskilde
Denmark
www.wind.dtu.dk

On the influence of turbulent inflow conditions on the wakes of floating offshore wind turbines

by

Michael Janßen

to obtain the degrees of

Master of Science
in Wind Energy
at Technical University of Denmark

Master of Science
in Aerospace Engineering
at Delft University of Technology

Supervisors:	Axele Viré	TU Delft
	Søren Juhl Andersen	DTU
Start date:	November 1st, 2023	
End date:	July 31st, 2024	
Student numbers:	TU Delft:	5833418
	DTU:	S223466

ABSTRACT

Floating offshore wind farms are a promising technological development that can help provide large amounts of energy from sites previously not feasible for wind farm development. To successfully develop floating wind farms, knowledge about the involved aerodynamics are crucial. A first building block of this is the understanding of the wake of a single floating wind turbine undergoing floating motion in turbulent wind fields.

Using an actuator line model within the Large Eddy Simulation framework YALES2 the wake of a floating wind turbine undergoing surge motion has been investigated at varying amplitudes and frequencies. Special attention was given to the inflow conditions, comparing laminar and low turbulent inflow conditions modeled using Mann turbulence boxes.

Varying the surge amplitude at a surge frequency equivalent to $St = 0.4$, the investigations show that the influence of the motion on the wake is greatly reduced even when low turbulence levels are present. Already at a turbulence intensity of 2.5% the wake deficit and wake turbulence intensity were indistinguishable from a fixed turbine's wake for lower surge amplitudes. Large surge amplitudes were required to significantly change these wake statistics, starting from an amplitude of $A/D = 0.16$ rotor diameters.Using proper orthogonal decomposition the dynamics in the wake have been analyzed. It was found that the effect of the rotor motion on the wake is lower when the inflow turbulence intensity is increased.

Varying the motion frequency in the range of $St \in [0.2, 0.8]$ at a amplitude of $A/D = 0.04$, it was shown that a surge motion at a frequency corresponding to $St = 0.6$ has the highest impact on the wake in terms of the reduction of modal time series correlations. However, even in that case the wake deficit and turbulence intensity in the wake are not changed significantly.

ACKNOWLEDGEMENTS

After two years of studying in Denmark and the Netherlands, the chapter of my academic journey is coming to a close. As this thesis marks the end of my studies, I want to express my gratitude to all those who have supported me along the way.

First, I want to thank my supervisors, Axelle Viré and Søren Juhl Andersen. Your insightful discussions and continuous support have been invaluable for this thesis. Additionally, I am grateful to Ricardo Amaral for his significant help in getting me started with the practical work and simulations.

I also thank my friends: Those who have been with me in the Netherlands and Denmark, making the challenging time and long hours enjoyable. Those back at home and spread across Europe, that supported me from afar and are still there when life gets busy. I especially want to thank Giannis for the great company, going through wins and losses together, and the mutual support in stressful times.

I am grateful for my (former) colleagues in Bremen who sparked my interest in wind energy, supported me in my academic development, and allowed me to be curious.

Lastly, I want to thank my family for supporting me on every path that I decided to take in every way possible. All of this wouldn't have been possible without you.

CONTENTS

LIST OF FIGURES ix

LIST OF TABLES xiii

ABBREVIATIONS xvii

1 INTRODUCTION 1
- 1.1 State of Research 2
  - 1.1.1 Wind Turbine Wakes 2
  - 1.1.2 Ambient Conditions at Offshore Wind Farm Sites 3
  - 1.1.3 Floating Motion 4
  - 1.1.4 Influence of Turbulence on the Wake 4
  - 1.1.5 Influence of Floating Motion on the Wake 6
  - 1.1.6 FOWT Wakes in Turbulent Inflow Conditions 6
- 1.2 Literature Summary 8
- 1.3 Research Questions 9

2 THEORY AND METHODOLOGY 11
- 2.1 Large Eddy Simulations 11
- 2.2 Actuator Line Method 12
- 2.3 Atmospheric Flows 13
- 2.4 Synthetic Turbulence Generation 14
- 2.5 Proper Orthogonal Decomposition 15

3 SETUP 19
- 3.1 CFD Code 19
- 3.2 Computational Domain and Boundaries 19
- 3.3 Discretization 20
  - 3.3.1 Computational Mesh 20
  - 3.3.2 Schemes 22
- 3.4 Actuator Line Model 22
  - 3.4.1 Limitations of the Turbine Setup 24
- 3.5 Computing and Data Management 25
- 3.6 Inflow Conditions 25
  - 3.6.1 Synthetic Turbulence Generation in YALES2 26
  - 3.6.2 Pre-computed Turbulence Fields 26
- 3.7 Influence of Grid Partitioning 28

- 3.8 Grid Independence Study 30
  - 3.8.1 Convergence of Thrust and Power 30
  - 3.8.2 Grid Convergence Index 32
- 3.9 Simulation Times 35
- 3.10 Mesh Selection 36
- 3.11 Global POD 38
  - 3.11.1 Correlations of Modal Time Series 38
- 3.12 Eigenvalue Convergence of POD Modes 39

4 RESULTS 41
- 4.1 Validation 41
- 4.2 Variation of the Surge Amplitude 45
  - 4.2.1 Deficit and Turbulence Intensity in the Wake 45
  - 4.2.2 Loads 46
  - 4.2.3 Added Power 49
  - 4.2.4 POD 50
  - 4.2.5 Correlations Between Different Flow Cases 56
  - 4.2.6 Correlations of Different Planes 60
  - 4.2.7 Section Summary 64
- 4.3 Variation of the Surge Frequency 65
  - 4.3.1 POD 65
  - 4.3.2 Threshold 67
- 4.4 Investigation on the Background Flow 70

5 CONCLUSION 73
- 5.1 Discussion of the Main Issues within the Research 73
- 5.2 Answers to the Research Questions 74
- 5.3 Summary 75

6 APPENDIX 77
- 6.1 Unstructured Grid 77
- 6.2 Dissipation of Synthetic Turbulence 78
- 6.3 POD Baseline - Base Components 80
- 6.4 POD Basis for Low Numbers of Samples 82
- 6.5 Correlations of POD Modal Time Series 83
  - 6.5.1 Comparison of Different Planes within one Case 83
  - 6.5.2 Comparison of Different Cases 91

BIBLIOGRAPHY 95

LIST OF FIGURES

1.1 Visualization of the flow field around a wind turbine, from Porté-Agel et al., 2019 2
1.2 Degrees of freedom of the FOWT motion, from Sebastian and Lackner, 2012 . . 5

3.1 Coordinate system of the domain. The rotor center is placed in the origin of the domain. 19
3.2 Simulation domain including the wind turbine model 20
3.3 Cross-section (y-z plane) of the computational mesh 21
3.4 Twist, chord, and thickness/chord ratio distribution of the DTU10MW RWT . 23
3.5 Airfoil polars including lift and drag coefficient for the airfoils with different thickness/chord ratios (T/C). 24
3.6 Velocity field of an empty box (no wind turbine) using the Mann turbulence generation boundary condition in YALES2. The high periodicity of the flow is shown. 26
3.7 Time averaged center-line turbulence intensity for an empty box at an inflow TI of $I_{in} = 2.5\%$ 28
3.8 Comparison of the streamwise velocity (u_x) field between simulations conducted with different numbers of cores. The cases are identical in initial and boundary conditions, and only differ by the number of cores. The given instantaneous fields are at the same time instance. The upper figure (a) is mirrored in the horizontal plane, such that a comparison is easier to make. 29
3.9 (a) Comparison of the velocity component u_x at a probe at location $2D$ downstream of the rotor and (b) difference of the stream-wise velocity time series for different partitioning 29
3.10 Comparison of the loads along the blade span, including different structured meshes $dx = R/16$ ("16"), $dx = R/24$ ("24"), $dx = R/32$ ("32"), filtered-LL correction method ("16_ll") and results from HAWC2 as a reference 34
3.11 Velocity magnitude field a fixed turbine with inflow turbulence $I = 0\%$ 36
3.12 Velocity RMS magnitude field a fixed turbine with inflow turbulence $I = 0\%$. 37
3.13 Cross-flow planes in the wake sampled for the POD analysis 38
3.14 Relative energy content of the POD modes, where a) presents the relative contributions of a mode i to the energy in the global POD database from Table 4.5 and b) shows the cumulative energy contribution of the modes up to mode i . . 40

4.1 Rotor- and time-averaged velocity deficit $\frac{\Delta U}{U_\infty}$ as a function of the downstream distance from the rotor. Data in figures a), c), and e) are taken from Z. Li et al., 2022, while b), d), and f) are computed in the current study. With a) and b) $I_{in} = 0\%$, c) $I_{in} = 1.5\%$, d) $I_{in} = 2.5\%$, e) $I_{in} = 4.7\%$, f) $I_{in} = 5\%$ 42

4.2 Rotor- and time-averaged turbulence intensity as a function of the downstream distance from the rotor. Data in figures a), c), and e) are taken from Z. Li et al., 2022, while b), d), and f) are computed in the current study. With a) and b) $I_{in} = 0\%$, c) $I_{in} = 1.5\%$, d) $I_{in} = 2.5\%$, e) $I_{in} = 4.7\%$, f) $I_{in} = 5\%$ 43

4.3 Velocity magnitude for the sway case $A/D = 0.04$, $St = 0.25$, $I_{in} = 0\%$ . . . 44

4.4 Velocity magnitude for the sway case $A/D = 0.04$, $St = 0.25$, $I_{in} = 5\%$ . . . 44

4.5 Rotor- and time-averaged velocity deficit $\frac{\Delta U}{U_\infty}$ as a function of the downstream distance from the rotor for different motion amplitudes and inflow turbulence intensities. With a) $I_{in} = 0\%$, b) $I_{in} = 2.5\%$, c) $I_{in} = 5\%$ 45

4.6 Rotor- and time-averaged turbulence intensity $\langle\sqrt{\frac{2k}{3}}\rangle/U_\infty$ as a function of the downstream distance from the rotor for different motion amplitudes and inflow turbulence intensities. With a) $I_{in} = 0\%$, b) $I_{in} = 2.5\%$, c) $I_{in} = 5\%$ 46

4.7 Comparison of tangential and normal loads F_t and F_n, sampled velocity for the ALM U_x, angle of attack, and force coefficients C_L and C_D over the non-dimensional radial position r/R for different surge amplitudes 47

4.8 Relative squared eigenvalues of the POD basis (left), and its' cumulative representation (right) 51

4.9 Stream-wise component u_x of the global POD basis. Only the first 25 modes are depicted. 52

4.10 Estimates of the validity of POD modes based on two different threshold criteria for the Eigenvalues of the SVD. Modes with eigenvalues below the threshold are considered invalid. 53

4.11 Normalized variances of the modal time series for varying plane positions and modes for the following cases: a) fixed, $I_{in} = 2.5\%$; b) fixed, $I_{in} = 5\%$; c) $A/D = 0.02$ $St = 0.4$, $I_{in} = 2.5\%$; d) $A/D = 0.02$ $St = 0.4$, $I_{in} = 5\%$; e) $A/D = 0.04$ $St = 0.4$, $I_{in} = 2.5\%$; f) $A/D = 0.04$ $St = 0.4$, $I_{in} = 5\%$ . . 54

4.12 Normalized variances of the modal time series for varying plane positions and modes for the following cases: g) $A/D = 0.08$ $St = 0.4$, $I_{in} = 2.5\%$; h) $A/D = 0.08$ $St = 0.4$, $I_{in} = 5\%$; i) $A/D = 0.16$ $St = 0.4$, $I_{in} = 2.5\%$; j) $A/D = 0.16$ $St = 0.4$, $I_{in} = 5\%$; k) $A/D = 0.32$ $St = 0.4$, $I_{in} = 2.5\%$; l) $A/D = 0.32$ $St = 0.4$, $I_{in} = 5\%$ 55

4.13 Cross-correlation of the modal time series and time lag for the flow cases fixed ($A/D = 0$), $I_{in} = 2.5\%$ and $A/D = 0.04$, $I_{in} = 2.5\%$. Both are at the plane at 6D downstream of the rotor. 56

4.14 Correlation of planes and modes corresponding for fixed ($A/D = 0$), $I_{in} = 2.5\%$ and $A/D = 0.04$ at $I_{in} = 2.5\%$. The plot is generated by creating multiple plots comparable to Figure 4.13 for identical plane positions and extracting the main diagonal. 57

4.15 Comparison of the progression of correlation between the moving turbine flow cases ($St = 0.4$, varying amplitude) and the fixed turbine flow case, both at an inflow turbulence level of $I_{in} = 2.5\%$. The threshold criterion is used to find the ratio of the number of modes with high correlation $\rho > \tau_c$ 59

4.16 Comparison of the progression of correlation between the moving flow cases and the fixed turbine ($A/D = 0$) flow case, both at an inflow turbulence level of $I_{in} = 2.5\%$. The threshold criterion is used to find the ratio of the number of planes with high correlation $\rho > \tau_c$ 60
4.17 Correlation of the modal time series between the equal modes at the plane at $x = 10D$ and the upstream planes for the flow case $A/D = 0.04$ at $I_{in} = 2.5\%$. The plot is generated by creating multiple plots comparable to Figure 4.13 for different combinations of cross-correlations between modal time series of planes in the same flow case and extracting the main diagonal. 61
4.18 Comparison of the progression of correlation between the plane at $x = 10D$ and the upstream planes, for different motion amplitudes at a turbulence level of $I_{in} = 2.5\%$ and a motion frequency of $St = 0.4$. The threshold criterion is used to find the ratio of the number of planes with high correlation $\rho > \tau_c$. . . 62
4.19 Comparison of the progression of correlation between the plane at $x = 10D$ and the upstream planes, for different motion amplitudes and a motion frequency of $St = 0.4$ at a turbulence level of $I_{in} = 5\%$. The threshold criterion is used to find the ratio of the number of planes with high correlation $\rho > \tau_c$. 63
4.20 Wake statistics for varying surge motion frequencies 65
4.21 Normalized standard deviations of the modal time series for varying plane positions and modes for the following cases: a) $A/D = 0.04\, St = 0.2, I_{in} = 2.5\%$ b) $A/D = 0.04\, St = 0.6, I_{in} = 2.5\%$ c) $A/D = 0.04\, St = 0.8, I_{in} = 2.5\%$ d) empty channel, $I_{in} = 2.5\%$. 66
4.22 Comparison of the progression of correlation between the moving turbine flow cases and a fixed turbine flow case, both at an inflow turbulence level of $I_{in} = 2.5\%$. The threshold criterion is used to find the ratio of the number of planes with high correlation $\rho > \tau_c$. 67
4.23 Comparison of the progression of correlation modal time series between the plane at $x = 10D$ and the upstream planes at an inflow turbulence level of $I_{in} = 2.5\%$ for a variation of the motion frequency. The threshold criterion is used to find the ratio of the number of planes with high correlation $\rho > \tau_c$. . . 68
4.24 Correlation of the planar modal time series for an empty channel flow and a fixed turbine, both over the same turbulent inflow field realization 71
4.25 Correlation between the modal time series of the plane at $x/D = 10$ and the upstream planes for the empty flow case 71

6.1 Layout of the tetrahedral mesh. The rotor center is positioned at (0,0,0), where x is the streamwise coordinate. The mesh is symmetric in the xy-plane and xz-plane. 77
6.2 Turbulence intensity as a function of the downstream position. TI were computed along the center line of the domain. 78
6.3 Energy spectrum of the turbulence box as a function of the wavenumber. The spectrum is approximated using the Karman-spectrum. The resolved energy between the cut-off due to mesh resolution and domain size are depicted. The energy losses are beyond these bounds. 79

6.4 Horizontal cross-stream component u_y of the baseline POD. Only the first 25 modes of the global POD ortho-normal basis are depicted. 80
6.5 Vertical component u_z of the baseline POD. Only the first 25 modes of the global POD ortho-normal basis 81
6.6 Stream-wise component u_x of the modal basis derived from long sample times of 245.76s (every 2^{12}th time step). Only the first 25 modes of the basis are depicted. 82
6.7 Correlations between the plane at $x = 10D$ and the upstream planes for the case $A/D = 0$, $St = 0$ (fixed), $I_{in} = 2.5\%$ 83
6.8 Correlations between the plane at $x = 10D$ and the upstream planes for the case $A/D = 0$ (fixed), $I_{in} = 5\%$ 83
6.9 Correlations between the plane at $x = 10D$ and the upstream planes for the case $A/D = 0.02$, $St = 0.4$, $I_{in} = 2.5\%$ 84
6.10 Correlations between the plane at $x = 10D$ and the upstream planes for the case $A/D = 0.02$, $St = 0.4$, $I_{in} = 5\%$ 84
6.11 Correlations between the plane at $x = 10D$ and the upstream planes for the case $A/D = 0.04$, $St = 0.4$, $I_{in} = 2.5\%$ 85
6.12 Correlations between the plane at $x = 10D$ and the upstream planes for the case $A/D = 0.04$, $St = 0.4$, $I_{in} = 5\%$ 85
6.13 Correlations between the plane at $x = 10D$ and the upstream planes for the case $A/D = 0.08$, $St = 0.4$, $I_{in} = 2.5\%$ 86
6.14 Correlations between the plane at $x = 10D$ and the upstream planes for the case $A/D = 0.08$, $St = 0.4$, $I_{in} = 5\%$ 86
6.15 Correlations between the plane at $x = 10D$ and the upstream planes for the case $A/D = 0.16$, $St = 0.4$, $I_{in} = 2.5\%$ 87
6.16 Correlations between the plane at $x = 10D$ and the upstream planes for the case $A/D = 0.16$, $St = 0.4$, $I_{in} = 5\%$ 87
6.17 Correlations between the plane at $x = 10D$ and the upstream planes for the case $A/D = 0.32$, $St = 0.4$, $I_{in} = 2.5\%$ 88
6.18 Correlations between the plane at $x = 10D$ and the upstream planes for the case $A/D = 0.32$, $St = 0.4$, $I_{in} = 5\%$ 88
6.19 Correlations between the plane at $x = 10D$ and the upstream planes for the case $A/D = 0.04$, $St = 0.2$, $I_{in} = 2.5\%$ 89
6.20 Correlations between the plane at $x = 10D$ and the upstream planes for the case $A/D = 0.04$, $St = 0.6$, $I_{in} = 2.5\%$ 89
6.21 Correlations between the plane at $x = 10D$ and the upstream planes for the case $A/D = 0.04$, $St = 0.8$, $I_{in} = 2.5\%$ 90

LIST OF TABLES

1.1 Terminology used for the FOWT DOFs 4

3.1 Description of the basis vectors of the coordinate system. 19
3.2 Boundary conditions of the domain boundaries 20
3.3 Time steps used in the different grids in the grid independence study 22
3.4 Parameters of the DTU 10MW RWT 23
3.5 Parameters used for generating the the inflow turbulence box 27
3.6 Power and thrust for a fixed turbine in laminar inflow on various meshes, including unstructured ("tet"), and structured ("hex") meshes. For comparison, results from the BEM-code HAWC2S are given. 30
3.7 GCI error estimates for thrust and power coefficient for 3 different structured meshes 32
3.8 Simulation times for selected simulations. Simulation times are given as the time required to simulate a 10-minute time series of the flow. 35

4.1 Parameters used for the validation study. Values in comparison to Z. Li et al., 2022 41
4.2 Variation of the mean and standard deviation of the power and thrust coefficients for different surging cases at $St = 0.4$, varying surge amplitude and inflow TI . 48
4.3 Maximum rotor surge velocities for different combinations of amplitude and frequency 49
4.4 Power required for the surge motion, and comparison to the aerodynamic power for different motion amplitudes at a surge frequency of $St = 0.04$ and inflow turbulence level of $I_{in} = 2.5\%$. 50
4.5 Flow cases used for the generation of the global POD basis 51

6.1 Mesh parameters for tetrahedral mesh, with the rotor diameter D and the cell length LC. LC is approximately $^5/_{12}D$, as used in Combette, 2023. 77
6.2 Possible energy losses due to domain size and mesh resolution. The Mann model input parameters $ae^{2/3}$, l and Γ are taken from Table 3.5. 79

NOMENCLATURE

Numerics

Δ	filter length scale (m)
δ	Kronecker symbol $(-)$
ϵ	Smearing length scale (m)
η_ϵ	Smearing kernel $(-)$
ν	Kinematic viscosity (m^2/s)
ν_t	Eddy viscosity (m^2/s)
ρ_d	Fluid density (kg/m^3)
τ	Subgrid-scale stress tensor (m^2/s^2)
C_S	Smagorinsky constant $(-)$
dt	Time step (s)
dx	Cell size (m)
f_i	External volume force (m/s^2)
f_ϵ	Smeared blade forces (m/s^2)
f_b	Blade forces (m/s^2)
k_r	resolved turbulent kinetic energy (m^2/s^2)
N_{cells}	Number of cells $(-)$
p	Pressure (N/m^2)
p_m	Modified Pressure (Nm/kg)
r	Distance to the actuator point (m)
S	Strain rate tensor $(1/s)$
x	Stream-wise position (m)
y	Horizontal position (m)
z	Vertical position (m)

POD

μ_X	Mean of the time series X (m/s)
ρ	Correlation coefficient $(-)$
Σ	Eigenvalue matrix of the SVD (m/s)
σ	Eigenvalue of the SVD (m/s)
σ_X	Standard deviation of the time series X (m/s)
τ_c	Threshold of the correlation coefficient $(-)$
τ_M	Threshold of the eigenvalues $(-)$
τ_{lag}	Lag of the cross correlation (s)
A	Modal time series matrix (m/s)
a	modal time series (m/s)
M	Data matrix (m/s)
n	Number of modes $(-)$
S	Snapshot of the velocity field (m/s)
U	Left eigenvector matrix of the SVD $(-)$
V	Right eigenvector matrix of the SVD $(-)$
v	Right eigenvector $(-)$

Wind turbine

ω	Rotation speed (rad/s)

A	Amplitude (m)
a	axial induction $(-)$
C_P	Power coefficient $(-)$
C_T	Thrust coefficient $(-)$
D	Rotor diameter (m)
D_{Hub}	Hub diameter (m)
f_m	Motion frequency $(1/s)$
F_n	Normal (out-of-plane) force (N/m)
F_t	Tangential (in-plane) force (N/m)
I	Turbulence intensity $(-)$
I_{in}	Inflow turbulence intensity $(-)$
P	Mechanical power (W)
P_{Surge}	Power input of surge motion (W)
R	Rotor radius (m)
r	Radial position (m)
St	Strouhal number $(-)$
U_∞	Free stream velocity (m/s)
U_{rated}	Rated wind speed (m/s)
v_{max}	Maximum rotor surge velocity (m/s)

Synthetic turbulence

$\alpha\epsilon^{2/3}$	Turbulence scaling factor (m^2/s^3)
Γ	Shear parameter $(-)$
l	Turbulent length scale (m)
$L_{x,y,z}$	Length of the turbulence box (m)
$N_{x,y,z}$	Number of grid points) $(-)$

ABBREVIATIONS

ABL	Atmospheric boundary layer
ALM	Actuator line method
AOA	Angle of attack
BEM	Blade Element Momentum theory
CFD	Computational fluid dynamics
CFL	Courant-Friedirichs-Lewy
DNS	Direct numerical simualtions
DOF	Degrees of freedom
DWM	Dynamic wake meandering
FOWT	Floating offshore wind turbine
GCI	Grid convergence index
IEC	International Electrotechnical Commission
LCOE	Levelized Cost of Energy
LES	Large eddy simulation
LL	Lifting line
NSE	Navier-Stokes equations
PDF	Probabilitiy density function
POD	Proper orthogonal decomposition
RANS	Reynolds-averaged-Navier-Stokes
RMS	Root mean square
RWT	Reference wind turbine
SVD	Singular value decomposition
TI	Turbulence intensity
TKE	Turbulent kinetic energy

1 Introduction

In recent years, the drivers towards using green energy resources have become increasingly multifaceted. Firstly, the effects of climate change become visible in many areas of the world, forcing governments to take action to implement measures for climate change mitigation. Secondly, the recent energy crisis in Europe has revealed the strong dependence of conventional energy sources on potentially unstable countries, leading to political pressure. Thirdly, the Levelized Cost of Energy (LCOE) of renewables has been decreasing continuously, making them a strong competitor to conventional energy sources from an economical perspective. As a result, green energy projects are driven forward, especially solar and wind energy. Currently, the development of wind energy is constrained: Onshore, distance regulations are the main drivers of limiting the wind farm area, while offshore it is not economically viable to install bottom-fixed wind turbines in water depths beyond approximately 60m.

A solution to this is the deployment of floating wind farms that can circumnavigate the water depth restrictions. These are currently under development, but not yet deployed on a larger scale, and therefore there are still a lot of open questions regarding the physics, especially fluid dynamics involved on the wind turbine and wind farm scale. This knowledge is crucial for the development of engineering models, which enable the optimization of floating wind farms.

One specific challenge is the understanding of the wake behavior of floating wind turbines and their dependence on the inflow conditions. As floating wind farms are still rare and on-site wake measurements extremely difficult to obtain, most of the understanding of these wakes is derived from experimental studies that neglect the influence of turbulence. However, recent advancements in wind turbine wake research have shown that wake dynamics significantly change in different turbulent conditions. This research project addresses this knowledge gap, combining turbulent inflow conditions and the floating motion of the turbine in a numerical study.

The remainder of the report is structured as follows: First, the state of the research on floating wind turbines is being summarized, leading to the development of the research objectives. This is followed by an overview of the relevant theoretical frameworks used within the thesis in chapter 2. Thereafter chapter 3 describes the setup of the study, including aspects of modeling and post-processing. Chapter 4 then covers the obtained findings in the report. The report is concluded in chapter 5, where the results are critically reflected and the main findings are summarized.

1.1 STATE OF RESEARCH

The wakes of Floating offshore wind turbines (FOWTs) are currently gaining interest in research. To investigate FOWT wakes in turbulent inflow conditions, it is essential to first examine wind turbine wakes independently before assessing the impact of turbulence levels and floating motion, as well as their combined effects.

1.1.1 WIND TURBINE WAKES

A wake is the result of the extraction of energy from a stream tube, following the 1D momentum theory. Due to the extraction of kinetic energy, the flow is slowed down and a low-speed area arises downstream of the wind turbine, which is termed wake. The velocity gradient between wake and free stream leads to the development of a shear layer. This shear layer tends to break up at some downstream distance, caused by disturbances like e.g. inflow turbulence, tip vortices, and tower shadow which cause strong mixing in the wake. This mixing process goes together with velocity fluctuations, and hence, increased turbulence levels.

Studies on the wake are mostly concerned with how this velocity deficit changes due to different operational and environmental conditions, how the wake leads to increased turbulence in the flow, and what implications the wake has on other turbines downstream.

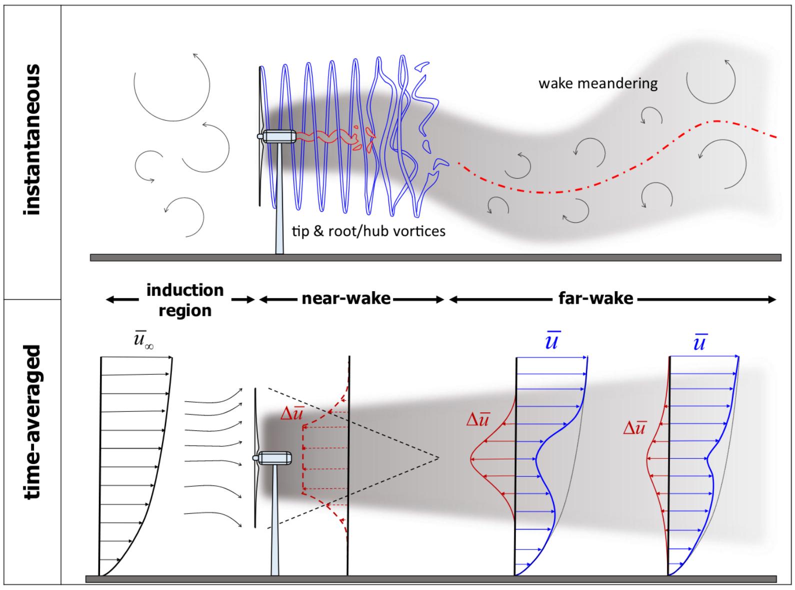

Figure 1.1: Visualization of the flow field around a wind turbine, from Porté-Agel et al., 2019

Following Vermeer et al., 2003 and Porté-Agel et al., 2019, a wind turbine wake consists of two parts. In the near-wake region, the characteristics of the wind turbine can have a strong impact, and the flow is dominated by the flow structures arising from the blades and nacelle (Vermeer et al., 2003). The far wake region, however, is less dependent on the actual geometry but depends on the operational parameters of the wind turbine like power and thrust coefficients (Porté-Agel et al., 2019). Near- and far-wake regions and the various flow phenomena assigned to them are depicted in Figure 1.1.

The cross-section of the wake deficit in the far wake region is often described as following a Gaussian shape (Bastankhah and Porté-Agel, 2014) and being self-similar, although deviations from a Gaussian can occur, e.g. when the turbine is yawed (Bastankhah and Porté-Agel, 2016), or when wind shear is present in the Atmospheric boundary layer (ABL).

In the transition region between near and far wake, the tip vortices break down. The stability of the tip vortices has been investigated and different effects can be identified that are related to the breakdown of the flow structures. Ivanell et al., 2010 investigated the conditions that cause tip vortex breakdown and found specific frequencies and modes associated with it.

Additionally, it has been found that under certain conditions the wake is found to develop large-scale cross-stream oscillations, called meandering, as depicted in Figure 1.1. Meandering is considered to be mostly caused by large-scale turbulent structures in the ABL, in which the wake is then transported as a passive tracer (Larsen, H. A. Madsen, Thomsen, et al., 2008). This is the underlying idea behind the Dynamic wake meandering (DWM) model (Larsen, H. A. Madsen, Bingöl, et al., 2007). Research in mechanisms causing meandering is ongoing.

This shows that, in practice, the behavior of the wake can be influenced by various factors, including wind turbine operational parameters and ambient conditions.

1.1.2 AMBIENT CONDITIONS AT OFFSHORE WIND FARM SITES

The relevant ambient conditions for a FOWT include wind speed distributions, turbulence intensity and and turbulence spectra, as well as wave heights and their distribution over different wave numbers (sea states).

Wind and waves are coupled: On one hand, due to the forces of the wind on the sea, waves develop. On the other hand, due to the waves, the surface roughness changes, which has an impact on the wind velocity profile. Additionally, wind and wave conditions are dependent on other factors like location, season, and large weather effects. As a result, it is an intricate task to derive general reference conditions and conditions can only described statistically.

IEC, 2005 outlines conditions for several load cases to be covered when designing an offshore wind turbine and gives a rough range of possible turbulence conditions.
Pollak, 2014 shows a comparison of Turbulence intensity (TI) vs height for multiple meteorological masts located at offshore sites. At a height of 100m, the mean values lie between 5% and 7%. The study suggests that the TI profile is logarithmically dependent on the height.

Marek et al., 2016 presents a Probabilitiy density function (PDF) of the TI at wind speeds from 8 m/s to 10 m/s at a height of 87m. The results suggest a peak between 4% and 7% TI. Additionally, they show a seasonal dependence of the mean TI, with ranges between 4% and 7% in different seasons.

1.1.3 Floating Motion

Like every rigid body, a FOWT can undergo motion in 6 Degrees of freedoms (DOFs), consisting of 3 translations and 3 rotations. In the context of floating structures, these are termed as shown in Table 1.1

Term	Translation
Surge	Streamwise translation
Sway	Horizontal, cross-stream translation
Heave	Vertical translation
Pitch	Rotation around the sway axis
Roll	Rotation around the surge axis
Yaw	Rotation around the heave/vertical/tower axis

Table 1.1: Terminology used for the FOWT DOFs

The motion is driven by excitation from wind, current, and waves. The response to these time-varying external forces depends on inertia (including gyroscopic effects), aero- and hydrodynamic damping, (elastic) restoring forces applied by the mooring. Additionally, the turbine controller leads to feedback between motion and forces. Hence, the FOWT motion is a *aero-servo-hydro-elastic* problem. From a state-space perspective the response of the wind turbine to the external forces can be lumped into a transfer function, which is then still dependent on actual design choices, e.g. the floater design strategy and sizing.

Messmer et al., 2024 summarizes, that a FOWT undergoes motion in a wide frequency range, where motion with high frequencies generally has low amplitudes and vice versa. The highest amplitudes are found for translation motion and are the order of 0.1 diameters.

1.1.4 Influence of Turbulence on the Wake

Studies concerning the wakes of (floating) wind turbines are often conducted assuming laminar inflow conditions. However, it has been revealed that wakes are strongly dependent on the inflow conditions. In an LES study, Wu and Porté-Agel (2012) showed the strong dependence of the wake characteristics like velocity deficit, turbulence intensity, and turbulent shear stress on the ambient turbulence levels.

Ivanell et al. (2010) analyzed the stability of tip vortices by means of Large eddy simulation (LES), applying a harmonic perturbation close to the blade tip. They found that specific excitation frequencies would lead to larger growth rate of instabilities and, hence, wake breakdown. Additionally, certain modes were identified that lead to faster growth. They derived that the instability is dependent on turbulence levels.

This was confirmed by LES simulations conducted by Y. Li et al. (2015) who found that by adding

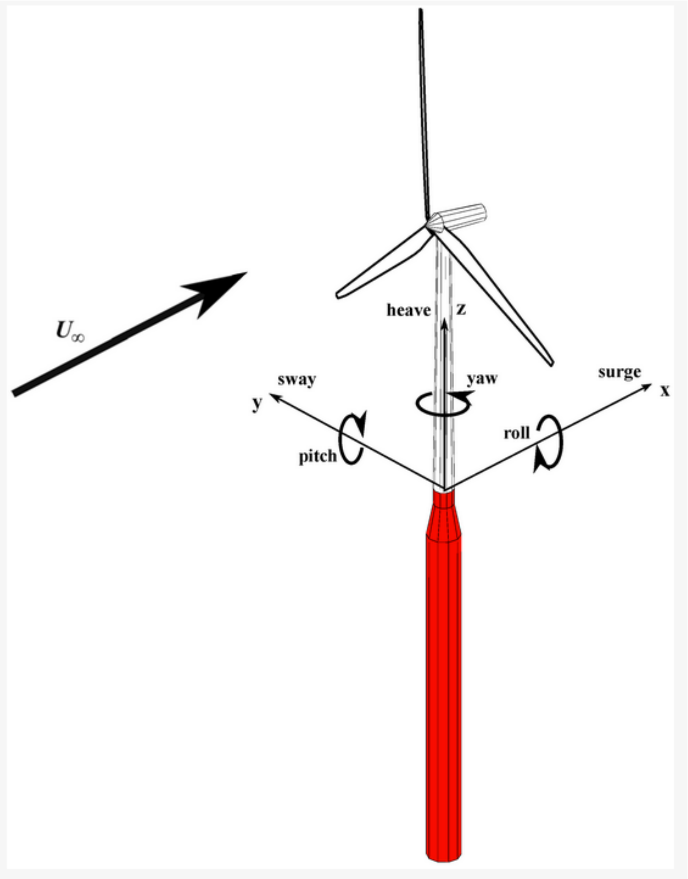

Figure 1.2: Degrees of freedom of the FOWT motion, from Sebastian and Lackner, 2012

turbulence to the inflow, instability of the blade tip vortices could be triggered. Hodgkin et al. (2022) extended on the stability analysis of Ivanell et al. (2010) and added stratification and shear effects to the inflow. They found that due to shear, at the bottom of the wake, the breakup is initiated first, as a result of the the smaller spacing between the tip vortices.

Hodgson, M. H. A. Madsen, et al. (2023) show the dependence of the wake breakdown on the scales of the turbulent inflow and their impact on the wake, showing distinct Strouhal numbers being responsible for the enhancement of the breakdown. When the inflow turbulence contained more energy in the range of $St \in [0.3, 0.7]$, then the wake breakdown and recovery are found to be enhanced.

Gambuzza and Ganapathisubramani, 2023 investigated the relation of TI and the scales of the turbulent inflow and link them to the near wake length and the occurrence of meandering. For high integral time scales, a slow wake evolution is found due to the high correlation of the flow.

Additionally, they found that the near wake length is small when TI is high, also for a variety of different turbulence spectra. They concluded that the strength of the shear layer is the dominant factor for the near wake length and the main reason for breakdown and meandering. Overall, the

recovery rate could be shown tho be a function of the Reynolds shear stress distribution in the center line.
Lastly, it is repeated, that wake meandering is generally associated with large turbulent structures (Larsen, H. A. Madsen, Thomsen, et al., 2008).

To conclude, ambient turbulence levels and shear have a significant effect on the wake. The influence is dependent on the turbulence intensity, hence the energy in the turbulence. Additionally, it is dependent on the frequencies of the disturbance, meaning the spectrum of the Turbulent kinetic energy (TKE) or scales involved. Shear plays an additional role, introducing asymmetry and changing locations of the wake breakdown. Turbulent inflow conditions do not only change the transition of the wakes but can also lead to meandering.

1.1.5 Influence of Floating Motion on the Wake

Different disturbances can affect the wake flow. Not only the turbulent inflow conditions, but also the motion adds such a disturbance.
Raibaudo et al. (2022) investigated the wake dynamics of a floating wind turbine model. By using Proper orthogonal decomposition (POD), they found that the spacial modes are not dependent on the frequency of the motion, while the temporal modes are. The temporal modes adapted to the forcing frequency and showed a lock-in-like behavior. When comparing floating and bottom fixed turbines, the floating has higher turbulence levels in the near wake, but lower turbulence levels in the far wake. This is in agreement with Zhou et al. (2022).

Using the same experimental setup as Raibaudo et al., 2022, Pardo Garcia et al. (2022) found that meandering is almost independent of the surge motion.
Messmer et al. (2024) quantified the dependence of the wake on the floating motions. Certain distinct Strouhal numbers of the motion could be found that lead to increased wake breakdown, for surge in the range of $St \in [0.3, 0.9]$ and for sway in the range $St \in [0.2, 0.6]$. Interestingly, these Strouhal number ranges for the motion are quite similar and partly overlap with the Strouhal number range of the inflow that would lead to increased recovery by Hodgson, M. H. A. Madsen, et al. (2023).

1.1.6 FOWT Wakes in Turbulent Inflow Conditions

As previously shown, there is evidence that turbulent flow conditions as well as floating motions do affect the wake characteristics. In a realistic scenario, often both conditions appear at the same time. Hence, research on the combined effects is relevant. However, it is not generally clear, in what way there is interaction and which parameters are relevant.

Belvasi et al. (2022) investigated a FOWT with surge, pitch, and heave motion in an ABL flow, and they could not find evidence for improved wake recovery due to the imposed motion. Other studies show, that indeed improved recovery can be found: Kopperstad et al., 2020 conducted analysis on spar and barge type substructures in laminar and turbulent inflow conditions using an actuator disc approach. They were able to find improvements of the recovery in both laminar and

turbulent inflow conditions. They highlight, that improvements were found to be higher for the spar type FOWT, as higher motion amplitudes could be found at higher frequencies.
Schliffke, Aubrun, et al. (2020) experimentally model the actuator disc approach in an ABL, varying amplitude and frequency of surge motion. Generally, the same mean velocity was found in the wake, but the turbulence intensity and turbulent kinetic energy profiles do change when amplitudes and frequencies reach extreme ranges.
Comparing laminar and turbulent inflow conditions by means of vortex methods, Ramos-García et al. (2022) found an interaction between turbulence and the floating motion. When comparing the laminar inflow computations, the breakdown is enhanced by the floating motion, leading to higher power production of a downstream turbine. However, the added benefits of floating motion for breakdown drastically decrease, when turbulence is present. In this study, prescribed pitch and surge motion were investigated.

Experiments on a FOWT in an ABL flow representative for offshore conditions by Pardo Garcia et al. (2022) show that surge motion has little effect on the wake breakdown. However, the surge frequency can be found in the downstream signal, meaning that a following turbine would be immersed in flow in a similar scale, so there could be a dynamic response.

Angelou et al. (2023) show that for measurements of real FOWT wakes, the recovery of the wake deficit and wake expansion is driven by ambient turbulence levels. A FOWT therefore shows a similar behavior as a bottom fixed turbine.
This implies that it is relevant to look at FOWT wakes including the inflow turbulence.
Zhou et al. (2022) conducted Reynolds-averaged-Navier-Stokes (RANS) simulations on a blade resolved simulation with added shear and turbulence. These show that the wake velocity distribution differences between floating and fixed turbines are small. Turbulence in the inflow makes the main difference, while shear has a minor contribution. The TI in the wake reduces faster under the influence of ambient turbulence, while a higher TI is found directly behind the blades.
Xu et al. (2023) presented a fully coupled numerical analysis of a floating wind turbine in an ABL, using an integration of FAST into their LES framework to solve the hydrodynamics and an Actuator line method (ALM) model for the aerodynamic representation of the FOWT. They found that the wake center varies because of pitching motion. Generally, the wake is shifted to the left (looking downstream). The static pitch of the floater leads to an upward force on the wake, driving the wake upwards. The turbulence intensity found in the wake was similar between both, floating and bottom fixed turbines. They conclude that only minor difference in the wake deficit between floating and bottom fixed have been found, but the wake center tends to rise upwards for the FOWT.

Z. Li et al. (2022) show that meandering can be induced by the side-side (sway) motion of the rotor at low turbulence levels. They also show that when inflow TI is high, the meandering is suppressed and the improvement in the wake recovery is lower than in laminar inflow conditions.

Schliffke, Conan, et al. (2024) conducted experiments on a a model FOWT in ABL flow combined with surge, pitch and heave motion. They found these idealized 1 DOF motions do not leave a signature in energy spectra. Such a signature occurs, however, when motion frequencies or amplitudes are very high and outside the operational envelope of a FOWT. The effects of surge motion were noticeable until 8D downwards of the rotor for certain amplitude and frequency combinations. Heave and pitch are less detectable in the wake and require high amplitudes and frequencies to be detected in the wake, but were generally not detectable at 8D downstream. The study additionally investigated the importance of different DOFs on the wake. They showed that surge and pitch had the most significant impact on the wake and errors by modeling a pitch motion as surge motion are small.

1.2 Literature Summary

Overall, the wakes of wind turbines are dependent on the specific ambient and operational conditions. Both, turbulent inflow conditions as well as different floating motions have been shown to change the wake behavior.
The methods used to investigate the influence of turbulence on floating wind turbine wakes vary as well as the parameter sets chosen, making a direct comparison between the different studies difficult.

Concluding the findings, floating motion can have an effect on the wake dynamics, which can vary depending on the movement direction, amplitude, and motion frequency. When additionally free stream turbulence comes into play, wake dynamics may drastically change. This means that an analysis of FOWT wakes requires considering the turbulent inflow conditions.

While within the research on the effects of turbulent inflow conditions on the wake, decomposition methods are commonly used in order to understand the flow characteristics, in the research of FOWTs the focus is often only directed towards the load analysis and statistical descriptions of the wake.

1.3 RESEARCH QUESTIONS

The review of the findings on FOWT wakes in turbulent inflow conditions revealed a gap in the literature body.
Following Messmer et al., 2024, sway and surge motion can impact the wake in terms of breakdown. While Z. Li et al., 2022 investigated sway motion and showed that turbulent inflow conditions drastically reduce the impact of the floating motion of the wake, no comparable study exists for the surge motion. Ramos-García et al., 2022 investigated surge motion under turbulent inflow conditions, but concentrated their work on loads and yields, rather than the wake flow field.

This work aims to describe the wake of a wind turbine undergoing surge motion in turbulent flows, in order to gain an understanding of the wake's sensitivity to the different conditions. Advancing knowledge in this direction could either build trust in existing wake models to be sufficient for FOWT applications or help gain an understanding of what physics engineering models need to capture when used for floating wind farm design.

Based on the previous findings on FOWT wakes as described in chapter 1, assumptions can be made on the wake behavior found for a FOWT in surge motion in turbulent inflow conditions:

1. *Surge motion only has a minor effect on the wake in turbulent inflow conditions*
    - How do the wake deficit and the turbulence intensity in the wake depend on the surge amplitudes?
    - How do the turbulence intensity and the wake deficit depend on the surge frequency?
2. *With increasing inflow turbulence intensities, the effects of surge motion vanish*
    - At which turbulence intensity level is a turbine motion as found for a realistic wind turbine negligible?
3. *When surging the turbine with sufficient amplitude, an effect on the wake can be found*
    - How large does a surge amplitude need to be, in order to change the wake behavior?

2 THEORY AND METHODOLOGY

In this section, the theoretical background of the research is explained. The theory behind the numerical methods to generate the flow fields as well as post-processing methods are being explained.

2.1 LARGE EDDY SIMULATIONS

In order to simulate the flow around the FOWT Computational fluid dynamics (CFD) is used. Within CFD, there are different fidelity levels, that differ by what spatial and temporal scales they resolve. It is possible, to compute all time and length scales of the turbulent flow by directly solving the Navier-Stokes equations (NSE). However, this approach, called Direct numerical simualtions (DNS), is unfeasible from the perspective of simulation cost due to the high spatial and temporal resolution required. It has been found that for sufficiently small scales, the turbulence characteristics are not dependent on the macro-scale flow topology, but there is a similarity between the small scales of all turbulent flows (Kolmogorov, 1941) (Kolmogorov, 1962). Applying this idea to CFD leads to the development of LES, developed by Smagorinsky (1963). The approach behind LES is to separate the scales, where large scales are resolved, while the small scales are modeled. In order to realize this approach, a filter operation is introduced to remove small scales.

This operation yields the filtered form of the NSE as follows:

$$\frac{\partial \overline{u}_i}{\partial t} + \frac{\partial \overline{\overline{u}_i \overline{u}_j}}{\partial x_j} = -\frac{\partial \overline{p_m}}{\partial x_i} + \nu \frac{\partial}{\partial x_j}(\frac{\partial \overline{u}_i}{\partial x_j} + \frac{\partial \overline{u}_j}{\partial x_i}) - \frac{\partial \tau_{ij}}{\partial x_j} + \overline{f}_i \tag{2.1}$$

$$\frac{\partial \overline{u}_i}{\partial x_i} = 0 \tag{2.2}$$

with the modified pressure $p_m = {}^{p}/_{\rho_d}$ (using the fluid density ρ_d, velocity vector u_i, kinematic viscosity ν, external volume force f_i and subgrid tensor τ containing all components that cannot be directly derived from the mean velocity $\bar{u}$ (Sagaut, 2006). While in the theoretical framework of LES, explicit filters are used, in practice the filtering is in most cases done implicitly by the mesh resolution being too coarse to resolve the smaller scales.

The subgrid tensor accounts for the effect of the small scales on the resolved larger scales. As the contents of the subgrid tensor are not resolved, various subgrid models have been proposed to account for the small-scale contributions. A quite successful model has been proposed by Smagorinsky (1963), which has following approach:

$$\tau_{ij} = \underbrace{\frac{1}{3}\tau_{kk}\delta_{ij}}_{Dilation} - \underbrace{2\nu_t\overline{S}_{ij}}_{Deviation} \tag{2.3}$$

The subgrid-scale tensor is split into dilation and deviation. The dilation term can be included in the pressure term and, hence, the sub-grid scale model only needs to represent the deviation. Closure of the problem is done by an eddy viscosity model. The underlying idea is that the effect of small-scale fluctuations is mathematically and physically comparable to an increased diffusion. Therefore an additional diffusion coefficient for momentum transfer, the eddy viscosity, is formulated.

Within the model developed by Smagorinsky, 1963, the eddy viscosity is computed as:

$$\nu_t = C_S\Delta^2|\overline{S}| \tag{2.4}$$

using the filter scale Δ, and a model constant C_S, referred to as Smagorinsky constant, and the filtered strain rate tensor $\overline{S}$:

$$\overline{S}_{ij} = \frac{1}{2}\left(\frac{\partial\overline{u}_i}{\partial x_j} + \frac{\partial\overline{u}_j}{\partial x_i}\right) \tag{2.5}$$

This model has the drawback of having a fixed constant, and hence does not perform well in certain flow conditions.

This drawback has been alleviated by the introduction of a dynamic approach by Germano et al. (1991), which introduces the adaptivity of the model by allowing the model constant to change in space and time. This model was then further refined by Lilly (1992). For wind turbine wake simulations, the dynamic approach has been shown to outperform the standard Smagorinsky model, especially in shear flows like those found in the ABL.

An implementation of the dynamic Smagorinsky model is present in the used CFD code YALES2 (Moureau et al., 2011) and will be used in this study.

2.2 ACTUATOR LINE METHOD

Even when using the LES approach, the numerical simulations of the flow around wind turbines are expensive. The reason is the boundary layer flow around the wind turbine blades: To properly resolve the boundary layer, cell sizes need to be sufficiently small at the wall. However, to compute the wake and resolve e.g. wake meandering, the domain needs to be sufficiently large. This necessity of small cell sizes and large domains simultaneously leads to very high cell numbers and computational costs. However, as in the analysis of the far wake the details of the flow near the blade are not relevant, the concept of the ALM is to model the effect of the blades rather than resolving them, which was proposed by Sørensen and Shen (2002). The method utilizes the force term in the Momentum equations of the NSE (Equation 2.1) in order to impose body forces that represent the effect of the blade. It has since been used and validated in many different wind turbine simulations and received several improvements, like dynamic stall correction, correction for losses at the blade tips, etc.

To model the effect of the blades on the flow, the model uses following approach:

1. Sample a representative wind velocity vector for the blade section from the flow.
2. Compute the force of the blade from tabulated force coefficient data depending on the inflow angle.
3. Apply the force as a volume force at the position of the blade. A smearing kernel is used to distribute the forces in order not to generate non-physical sharp peaks in single cells (that lead to numerical instability).

In the context of ALM simulations, the smearing kernel responsible for distributing the forces from the blade onto the mesh has been found to have a significant impact.
Following Sørensen and Shen, 2002, the blade forces are applied to the flow by applying the convolution to the blade forces f_b with a smearing kernel η_ϵ, yielding the spatially smeared forces f_ϵ:

$$f_\epsilon = f_b \otimes \eta_\epsilon \tag{2.6}$$

where the smearing kernel η_ϵ is defined as:

$$\eta_\epsilon(r) = \frac{1}{\epsilon^3 \pi^{3/2}} exp[-(r/\epsilon)^2] \tag{2.7}$$

where ϵ is a regularization length scale and r the distance of the actuator point to the cells at which the forces are applied.

This regularization length scale has been found to have a significant effect on the performance of the ALM. It stabilizes the computation by applying a Lamb-Oseen viscous vortex core, and therefore reducing the velocity gradients (Meyer Forsting and Troldborg, 2020). However, it also introduces an error in the angle of attack, and hence, affects the forces exerted by the blades. Different types of corrections have been investigated to mitigate these errors. Often, tip correction methods are being used, that have their origin in the Blade Element Momentum theory (BEM) method. However, these generally correct for a finite number of blades, which in an ALM framework is invalid (Meyer Forsting, Pirrung, et al., 2019). The development of correction methods to improve ALM performance is an active field of research with different correction methods being proposed, in order to adapt the smearing length scale ϵ to the blade parameters, e.g. Meyer Forsting, Pirrung, et al., 2019, Martínez-Tossas and Meneveau, 2019.

2.3 ATMOSPHERIC FLOWS

Realistic inflow conditions on land and at sea are complex, involving a multitude of physical scales and phenomena that shape the actual wind field. These factors range from seasonal effects over the course of a year, over large weather systems, to daily thermal variations, and terrain-dependent changes.

Locally, the flow is strongly influenced by the development of the ABL. Due to the presence of the Earth's surface, where the velocity approaches zero, a boundary layer forms with a distinct velocity profile, typically characterized in terms of shear.

Thermal effects lead to different stability conditions. The stability conditions affect, how fluctuations are amplified due to the thermal conditions. These fluctuations then have an impact on the mixing in the ABL, leading to different velocity and temperature profiles. A description of the ABL in dependence of the stability effects has been developed by Monin and Obukhov, 1954.

Additionally, other factors change the flow like blockage, interaction with other wind turbines and wind farms, and surface roughness change due to sea states. Atmospheric physics and how to represent different inflow conditions are a very active field of research.

2.4 Synthetic Turbulence Generation

Due to the high complexity of the atmospheric wind fields, within the context of CFD, a variety of simplifications have to be taken: On one hand, a simplified setup allows for the identification and isolation of different effects at play. On the other hand, limitations are imposed by the capabilities of the setup, considering the numerical cost of simulations.

For studies using LES, there are generally two popular approaches: precursor simulations and synthetic turbulence injection.

In precursor simulations, the inflow conditions are obtained by running a separate CFD simulation. A second simulation is set up, that resembles a box in the atmosphere. By connecting inflow and outflow periodically and applying a pressure gradient, an infinite channel can be computed. When this channel flow is converged, velocity fields can be sampled on planes from the precursor simulation, which are then used as the inflow conditions of the main simulation.

A precursor simulation is a full LES simulation and needs to include all the relevant (boundary-) conditions that influence the development of the velocity profile and turbulence generation. This means adding a transport equation to the system, in case thermal effects need to be modeled. Hence, precursor simulations are connected to high computational costs. Additionally, as the boundary layer is a result of a simulation, it is not well suited to quickly vary different inflow parameters.

A more pragmatic approach is synthetic turbulence injection. Here, a turbulence field is precomputed by other means than CFD, in order to generate a wind field with specified statistics. This field can then be mapped onto the boundaries of the CFD domain. The turbulent inflow from a turbulence box is based on Taylor's "frozen turbulence" hypothesis. Following Taylor, 1938, for a turbulent wind field space and time are interchangeable. Hence the turbulent flow field is advected, without changing itself. Therefore, a time-dependent inflow can be generated from the turbulence box by sampling along the stream-wise direction.

Synthetic turbulence generation methods often consist of a description of a turbulent spectrum and the use of inverse Fourier transforms to generate a wind field. These methods are generally computationally less expensive than precursors. As the turbulent wind field generated with such an approach is not necessarily a solution of the NSE, interactions with the CFD solver near the inlet are to be expected, like pressure oscillation and dissipation of turbulent structures. Hence, for the use in CFD computations, specific synthetic turbulence generation methods have been developed, that minimize these effects, e.g. the divergence free synthetic eddy method developed by Poletto et al., 2013.

In wind energy engineering, the so-called "Mann model" is often utilized for turbulence generation. It is based on a linearized form of the NSE and was initially, meant to estimate spectral information based on the model fit to wind measurements (Mann, 1994). It can be used to generate a turbulent wind field (Mann, 1998). The Mann model is part of the International Electrotechnical Commission (IEC) standard requirements to specify load cases to be investigated in the certification process of a wind turbine (IEC, 2005). Therefore, the Mann turbulence generation is an established reference, that is used in all sorts of simulations regarding wind energy applications. This includes CFD simulations, despite the previously mentioned drawbacks related to synthetic turbulence fields.

2.5 PROPER ORTHOGONAL DECOMPOSITION

The wind turbine wake flows will be analyzed by means of proper orthogonal decomposition (POD), based on the snapshot method introduced by Sirovich, 1987. The underlying idea is to decompose the time signal of the flow fields (a row of "snapshots") into their variation in space and time. This way, the most energetic modes of the flow can be identified. As the scale of turbulence eddies is associated to their energy content, POD is often used in an attempt to describe large scale fluctuations and coherent structures. POD is therefore a data-driven method and besides flow analysis and description it finds application in building reduced order models of flow fields.

The POD methodology applies singular value decomposition Singular value decomposition (SVD) to a matrix containing snapshots of a fluid flow. When applied to snapshots including all velocity components, POD provides an orthogonal basis based on the maximum variance, hence energy in modes, which allows for a more intuitive interpretation of the spacial modes. The ortho-normal basis can be used to decompose a flow time series (a sequence of snapshots) into their modal contributions, and in that way see the temporal behavior of the modes at play.

A snapshot is defined as the column vector which comprises the all three velocity components at all flow positions in the dataset to be analysed:

$$S(t) = \begin{pmatrix} u_{x,i}(t) \\ u_{y,i}(t) \\ u_{z,i}(t) \end{pmatrix} \tag{2.8}$$

The ordering of the elements within the column vector is arbitrary but needs to be consistent along all snapshots. The snapshots are assembled into a data matrix M:

$$M = (S_1, S_2 \dots) \tag{2.9}$$

which generally yields a tall and skinny data matrix, where every column represents a snapshot and every row an ensemble of different values for a given flow velocity component at a specific location in the domain.

There are two routes to obtain the proper orthogonal decomposition. First, singular value decomposition can be applied on the data matrix M, yielding:

$$M = U\Sigma V^T \tag{2.10}$$

where U and V are matrices containing the left and right singular vectors. Both U and V are ortho-normal. In the context of POD, U contains spacial information, while V contains time information. The Matrix Σ is a diagonal matrix, with decreasing eigenvalues on the main diagonal. The squared eigenvalues in Σ represent the resolved kinetic energy in the flow fluctuations.

Alternatively, an equivalent eigenvalue problem can be formulated, as shown e.g. in Kerschen et al., 2005, which is the direct result of inserting the SVD formulation Equation 2.10 into the auto-covariance matrix:

$$M^T M = V\Sigma^2 V^T \tag{2.11}$$

For the matrix M with dimensions $(m \times n)$ this means solving a $n \times n$ problem. For usual POD applications, data matrices are tall and skinny, i.e. m»n. This way, computations can be more memory efficient.
The modes that contain spacial information (left singular vectors U) can be reconstructed as:

$$U = MV\Sigma \tag{2.12}$$

The combination of time and amplitude variations, named modal time series can be obtained:

$$A = U^T M = \Sigma V^T \tag{2.13}$$

Instead of the data matrix M a matrix with a different time series of snapshots can be used, which projects the new M=matrix into the ortho-normal basis of the spatial modes. Then the obtained modal time series will represent the modal energy content over time for the new data set in terms of the POD basis.

The eigenvalues, and hence the energy content in the modes, can be retrieved by:

$$a_i(t) * a_i(t) = \sigma_i v_i * \sigma_i v_i = \sigma_i^2 \tag{2.14}$$

using the ortho-normal property $v_i v_j = \delta_{ij}$ of the right eigenvector matrix, where $a_i(t)$ is the component of the modal time series matrix A that is assigned to mode i. In the same way, for a modal time series the energy content can be retrieved. The variance of a modal time series is a measure of the energy contained in a mode:

$$E_i = \overline{a_i(t) a_i(t)} \tag{2.15}$$

3 SETUP

The section comprises two main parts: Firstly, the setup of the computation in the numerical framework is explained, spanning the computational domain, mesh creation, scaled wind turbine model, as well as the inflow conditions. Secondly, pre-studies are included that cover the interaction of turbulent inflow and the used grid, as well as the influence of the partitioning approach

3.1 CFD CODE

The CFD code YALES2 (Moureau et al., 2011) is used. It can simulate the fluid flow on large grids using parallel processing and has been used for several studies in wind energy applications. Several studies show the capabilities of the code using actuator line models implemented in the framework, like (Benard et al., 2018), (Houtin—Mongrolle et al., 2021), and (Combette, 2023). In the context of wind turbine wake simulations, low Mach numbers are expected and, hence, compressible effects are considered negligible. The incompressible solver *ICS* is used within this project, which is based on a predictor-corrector approach.

3.2 COMPUTATIONAL DOMAIN AND BOUNDARIES

The computational domain comprises a box of dimensions 15Dx6Dx6D (Figure 3.2) in which the turbine with a diameter of $1D = 178.3m$ is placed 3D downstream of the inlet. The coordinate system is chosen such that the origin is in the rotor center (Figure 3.1), with the streamwise direction x, the horizontal direction y, and the vertical direction z.

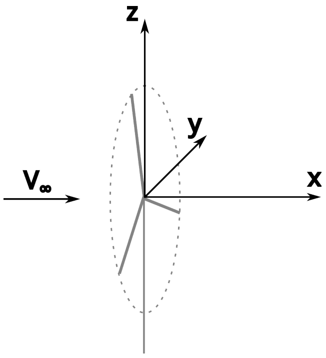

Figure 3.1: Coordinate system of the domain. The rotor center is placed in the origin of the domain.

Direction	Description
x	Streamwise
y	Horizontal
z	Vertical

Table 3.1: Description of the basis vectors of the coordinate system.

For the choice of the cross-section of the box, blockage effects are relevant. The rotor-based blockage is $\pi(D/2)^2/(6D)^2 \approx 2.2\%$. The influence of the blockage has been studied by Combette, 2023 in a similar application and it showed that the velocity profile in the wake is not significantly altered when using a cross section of $6D \times 6D$ when compared to $8D \times 8D$.
The placement of the rotor is chosen in order to leave sufficient space between the rotor-induced velocity field and the inlet, and to keep the turbine outside of the zone where interaction between grid/discretization and inlet turbulence is strong, which will be further discussed in section 6.2. Similar computations by Z. Li et al., 2022 used $3.5D$ distance between rotor and inlet, while Combette, 2023 found no difference when comparing distances of $5D$ to $3D$. In the current setup, the rotor is placed $3D$ downstream of the inlet.

The domain length is chosen to gather sufficient data on the far wake. The aim is to resolve the wake up to $10D$ downstream in order to compare the results with reference studies. In YALES2 sponge layers are being utilized in order to dampen instability effects caused by the boundary condition at the outlet. In pre-studies, this was found to affect the flow further upstream. In order to minimize the effects of the boundary condition at the outlet and the sponge layers on the data, the domain was extended in the downstream direction. The final domain length was then chosen as $15D$, leaving a wake region with the length $12D$, where $10D$ is considered to be not influenced by the outlet boundary. A visualization of the domain can be found in Figure 3.2.

The boundary conditions have been chosen as shown in Figure 3.2. A further introduction of the inflow boundary condition follows in section 3.6.

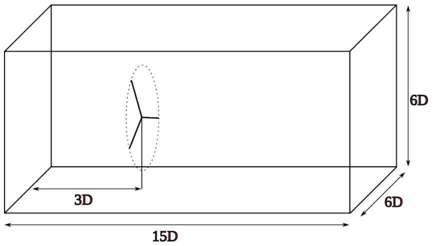

Figure 3.2: Simulation domain including the wind turbine model

Patch	Boundary Condition
Bottom	Slip
Top	Slip
Sides	Slip
Inlet	Uniform + synthetic turbulence
Outflow	zero Gradient

Table 3.2: Boundary conditions of the domain boundaries

3.3 DISCRETIZATION

This section deals with the discretization of the numerical problem, including the mesh as well as the discretization schemes for space and time.

3.3.1 COMPUTATIONAL MESH

The computational mesh needs to fulfill a a variety of requirements. Generally the mesh selection is a trade-off between computational cost and accuracy.

Considering the mesh resolution, Troldborg et al., 2007 showed that for resolving the tip vortices, a resolution of at least $dx = R/32$ is required, with a rotor radius R and the grid element length dx. This is supported by Hodgson, M. H. A. Madsen, et al., 2023, who additionally showed, that although lower resolution cannot depict the tip vortices, the overall behavior of the wake and the breakdown location are predicted well at a resolution of $dx = R/16$. As the interest in this study is on the overall wake behavior rather than the distinct flow features by the blade, this coarse resolution of $dx = R/16$ is chosen as a baseline and a grid dependence study (section 3.8) will further shed light on the implications of this choice.

The mesh topology, i.e. the grid elements and overall spatial structure of refinement levels is chosen based on the capabilities of the used code to deal with different mesh elements, regions of interest in the flow as well as intended post-processing. A cartesian grid with hexahedral mesh elements is chosen, in order to obtain a uniform grid in the region sampled for the POD analysis. The mesh has a uniform region centered around the rotor with a cross-section of $3D \times 3D$. Smooth grading is applied outside that region in order to reduce the number of cells in the less relevant flow regions. A cross section of the used mesh is shown in Figure 3.3. No grading was applied in the stream-wise direction. All meshes are created using the open-source meshing-software GMSH (Geuzaine and Remacle, 2009) v.4.11.1. The grid size for the baseline mesh is 8.3×10^6 elements.

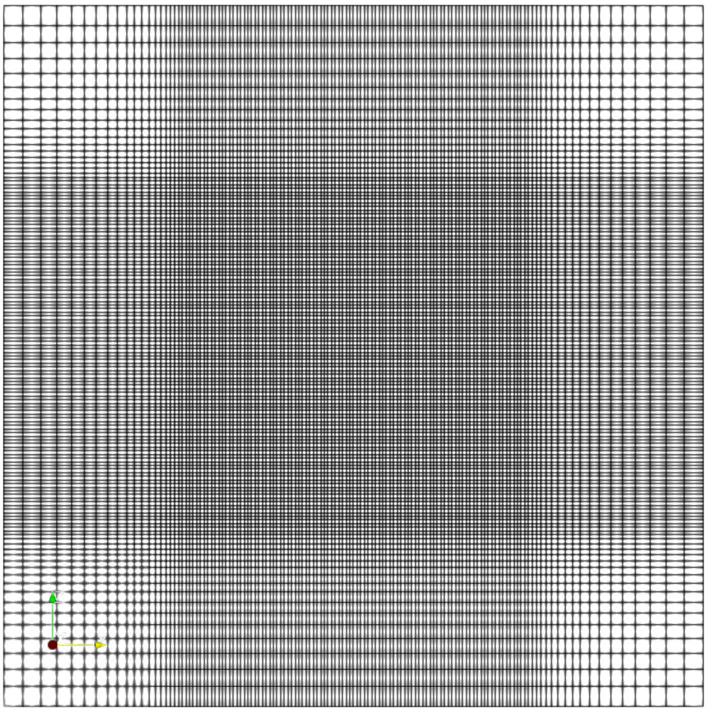

Figure 3.3: Cross-section (y-z plane) of the computational mesh

A grid convergence study is carried out in order to evaluate the influence of the computational grid on the results and to estimate errors. This is done in section 3.8.

3.3.2 SCHEMES

The discretization schemes were chosen according to the findings of Benard et al., 2018, showing that within the YALES2 framework, fourth-order discretization schemes in time and space yield improved accuracy while not adding excessive computational cost. In all computations, a 4th order central scheme was used for the spatial discretization, while time integration was performed using a 4th order "TFV4A" scheme, which is blending between a 4th order Runge-Kutta and a 4th order Taylor-Galerkin scheme Kraushaar, 2011. The time step size was fixed in order to fulfill the Courant-Friedrichs-Lewy (CFL) condition Equation 3.1 as well as limit the number of cells a blade element would travel within a time step Equation 3.2. It was found that generally the condition on the blade element travel distance per time step set heavier constraints on the time step size.

$$\frac{U dt}{dx} \leq 1 \tag{3.1}$$

$$\frac{\omega D dt}{2dx} \leq 1 \tag{3.2}$$

For the cartesian grids, time steps were chosen in accordance with Equation 3.2 as shown in Table 3.3. The CFL-number of $^{U dt}/_{dx} < 0.2$ was found in all simulations.

R/dx	dt in s
16	0.06
24	0.04
32	0.03

Table 3.3: Time steps used in the different grids in the grid independence study

3.4 ACTUATOR LINE MODEL

The actuator line model (ALM) is set up to resemble the DTU 10MW Reference wind turbine (RWT) developed Bak et al., 2013. The main turbine parameters are depicted in Table 3.4. The baseline of the current setup is the HAWC2 model implementation of the RWT provided by DTU-Wind, 2020.

For a YALES2 ALM model, chord, twist as well as force coefficients need to be given at the same spanwise points, such that these parameters can then be interpolated onto the exact location of the actuator points. This requires prior interpolation of the blade data provided by the HAWC2 model onto a single set of discrete points along the blade.

Parameter	Abbreviation	Value
Rotor Diameter	D	178.3m
Rated wind speed	V_{rated}	11.4 m/s
Rotational Speed	ω_{rated}	9.6 RPM
Hub diameter	D_{Hub}	5.6m

Table 3.4: Parameters of the DTU 10MW RWT

The twist has been interpolated linearly with regards to the spanwise position onto the points where the chord and thickness/chord ratio are given. The force coefficients have been interpolated from the airfoil polars, depicted in Figure 3.5, linearly with regard to the spanwise thickness/chord distribution. Chord, twist, and thickness/chord distributions are depicted in Figure 3.4.

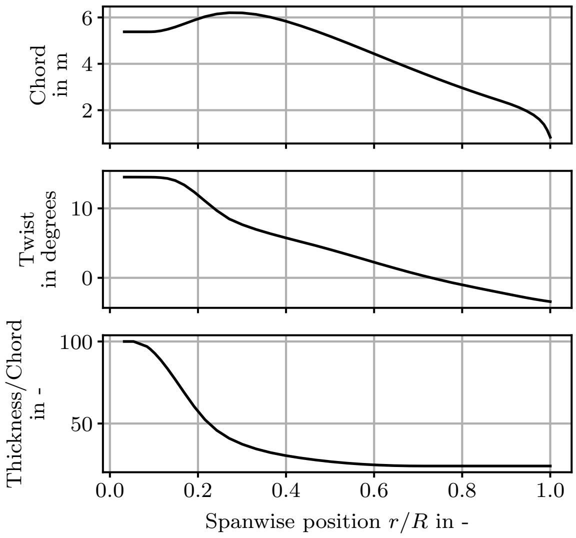

Figure 3.4: Twist, chord, and thickness/chord ratio distribution of the DTU10MW RWT

The polars provided from the RWT were computed using 2D CFD by Bak et al., 2013. For angles of attack outside the normal operation range (-180 to -45 and 45 to 180), the lift and chord values were computed assuming a flat plate and using simple analytical functions, as described in Bak et al., 2013. All airfoil polars for the six different thickness/chord ratios are shown in Figure 3.5.
The thick airfoil polars (thickness/chord ratio of 60% and 48%) have special shapes with the lift increasing discontinuously with two bumps for increasing angle of attack. The 60% airfoil additionally shows the lift to increase for negative angles of attack. All airfoil polars are given only for single, selected Reynolds numbers and the ALM does not account for Reynolds number changes.

The floating motion is then modeled as a sinusoidal motion of the ALM along a single translational DOF. Within YALES2, the motion is prescribed based on a user-defined function for the

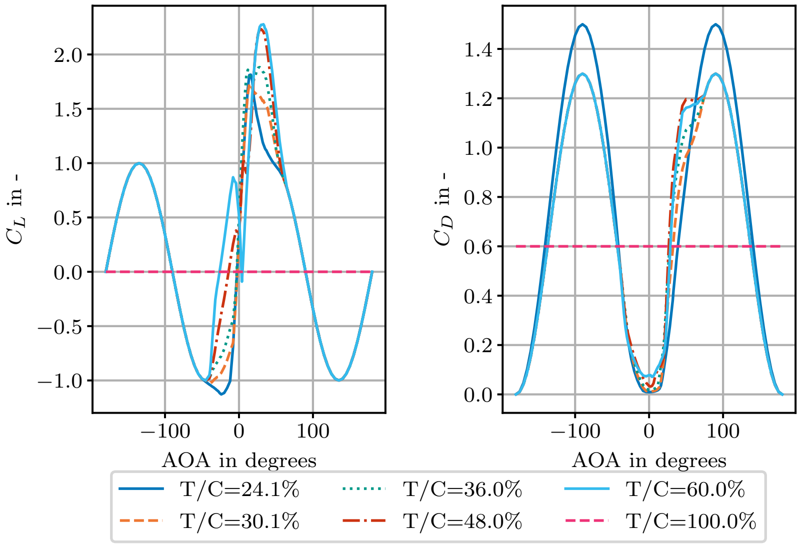

Figure 3.5: Airfoil polars including lift and drag coefficient for the airfoils with different thickness/chord ratios (T/C).

motion velocity. Within this thesis, the motion frequency is described in a dimensionless manner using the Strouhal number:

$$St = \frac{f_m D}{U_\infty} \tag{3.3}$$

with the motion frequency f_m, rotor diameter D and free stream velocity U_∞. While the Strouhal number is a non-dimensional measure for flow oscillations, it is commonly expanded to non-dimensionalize other frequencies, like motion frequencies or frequencies in the inflow. No controller is considered in the setup and the turbine is operated at a fixed rotational speed, as given in Table 3.4

3.4.1 Limitations of the Turbine Setup

The modeling choices lead to limitations of the current setup when compared to a real wind turbine.

The model does not include elastic behavior, which has been shown to affect the aerodynamics of large turbines like the DTU 10MW RWT.
Additionally, imposing the motion of the turbine instead of computing the motion based on forces acting on the structure is strongly idealized, as the system behavior is very complex. When imposing the motion, wave excitation in that sense and pitch as a result of thrust are not considered.
Lastly, tower and nacelle are not included in the model, although they will have a significant impact on the wake breakdown.

3.5 Computing and Data Management

Simulations were run on TUDelft Cluster HPC12, which allowed for parallel computing using multiple nodes with Intel Xeon E5-2640v3 and v4 CPUs. It was found that for the current simulations, there were no noticeable improvements in computing time when using more than 2 nodes (i.e. >40 cores) per computation. This is likely connected to the required data transfer between the nodes becoming a bottleneck. For the POD, long data samples are required leading to large runtimes. However, this is undermined by the wall clock time limit of 72 hours per computation on the cluster. Therefore, simulations needed to be stopped and restarted in order to combine data from multiple runs.

It appears that in YALES2 the restart of simulations with an actuator line moving in space is inexact, and hence, a transient was found on every restart in the power signal of the simulation. As a direct result, also the flow in the wake is likely changed by this, such that a transient needs to be removed at every restart and no coherent time series longer than than possible in a single run can be obtained.

3.6 Inflow Conditions

As discussed in section 2.3, realistic inflow conditions for an (offshore) wind turbine are complex.

In order to model the inflow in the CFD framework using synthetic turbulence, it is necessary to make simplifications and assumptions due to the computational limits. Further, it is easier to isolate the relations between inflow turbulence and wake, if the model complexity is reduced.
The choice was made to neglect veer and sheer, and only concentrate on the turbulence intensity in this study. This is done as in Z. Li et al., 2022 and Ramos-García et al., 2022, the effects of varying the TI levels was significant even without shear effects. Hence, it is assumed that alone in the TI levels, a quite significant impact can be found for the flow.

Using synthetic Mann-boxes is a standard procedure in wind turbine load calculations and medium fidelity modeling like unsteady BEM codes. However, in the context of CFD, synthetic turbulence inputs come with a set of problems.
The Mann-boxes are derived from a linearized form of the NSE (Equation 2.1, Equation 2.2), and therefore are not a solution of the NSE itself. Hence, when put into a finite volume solver which is constrained to solving NSE, effects can occur that change the input turbulence. Overall, turbulence is convected over the domain, and generally, Taylor's frozen turbulence assumption (Taylor, 1938) is used. However, in the CFD domain, there will be interaction of the turbulence box with the domain size (large lengths scales "don't fit" into the domain) as well as interaction with the grid resolution (too small turbulent structures cannot be resolved). All these have implications on the turbulent flow field, and that leads to a difference between the turbulent field at the inlet and the turbulent field that arrives at the rotor plane.

Due to this complex interaction of the injected turbulent field and the domain itself, a high effort was put into understanding the interaction of inflow field, domain, mesh, and CFD solver.

3.6.1 Synthetic Turbulence Generation in YALES2

YALES2 offers the option to directly define a turbulent length scale and turbulence intensity in order to generate a turbulent inflow field according to the Mann model within the CFD solver. Additionally, it is possible to pre-compute a turbulence field and superimpose it to uniform inflow conditions at the inlet.

Testing of the in-built turbulence generation boundary condition revealed high periodicity in the velocity field, shown in Figure 3.6. This is likely due to the generated turbulent field being too small. No mitigation measure for this condition was found on a user level, rendering pre-computed turbulence fields the viable option for the current project.

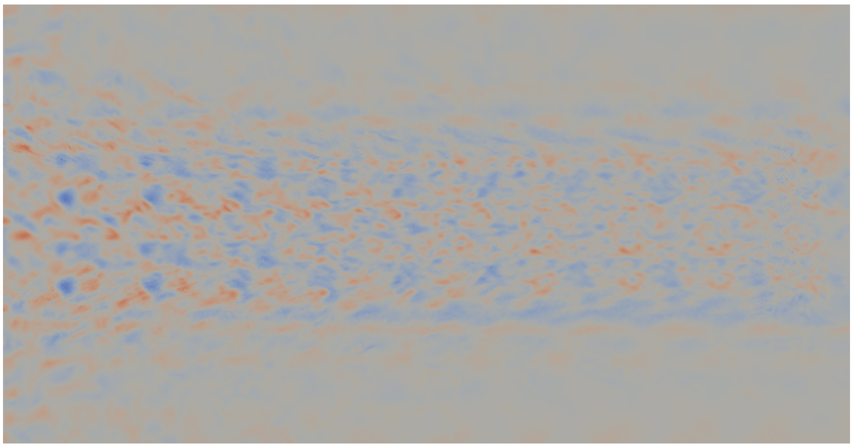

Figure 3.6: Velocity field of an empty box (no wind turbine) using the Mann turbulence generation boundary condition in YALES2. The high periodicity of the flow is shown.

3.6.2 Pre-computed Turbulence Fields

The second option within YALES2 is to pre-compute a turbulence field with external software and feed the turbulent field into the CFD solver. To generate a turbulence box with appropriate conditions, several studies have been compared.

Most studies using Mann boxes, only a reference TI is given. However, as described previously, the Mann model takes three input parameters: a length scale l, a parameter to scale the turbulence intensity $ae^{2/3}$, and a shear parameter Γ. As a result, reproducing the turbulent inflow results is not straightforward.
To set a range for the TI, different studies have been compared. Angelou et al. (2023) show that there is already a large difference in the wake characteristics when comparing TI of $I = 2\%$ and $I = 4\%$. In the same way, results in Z. Li et al., 2022 show that beyond a TI of $I = 4.7\%$, the

impact of side-side motion on the velocity deficit and the turbulence in the wake is negligible.

The choice of length scale and shear parameter is more intricate, as they are barely reported. Davenport, 1965 find the shear exponent offshore to be $\alpha = 0.10$. Later Hsu et al., 1994 showed that the shear exponent offshore at neutral ABL is around 0.11. To compute a length scale, Kelly, 2018 showed that the length scale can be derived using TI and shear exponent. Additionally, Peña et al., 2010 has further information on the choice of length scales, although the considered site is not far offshore.
As the choice of shear parameter and length scale is still ambiguous, the choice of these parameters is finally done in accordance with the IEC standard (IEC, 2005).

In this project simulations at TI levels of $I = 0\%$, $I = 2.5\%$, and $I = 5\%$ are planned. A single instance of a synthetic Mann box is generated using the parameters depicted in Table 3.5. This instance is then scaled to obtain different turbulence intensities.

Parameter	Value
$ae^{2/3}$	1
Γ	3.9
l	33.6 m
$N_x \times N_y \times N_z$	$1025 \times 257 \times 257$
$L_x \times L_y \times L_z$	$7139m \times 1790m \times 1790m$

Table 3.5: Parameters used for generating the the inflow turbulence box

Preliminary investigations on an empty domain without a wind turbine have been done in order to investigate how the inflow turbulence changes along the downstream direction. This is done due to the previously described interaction of the turbulence box with the grid, where dissipation of turbulence near the inlet is expected. Adding to this, the resolution of the CFD domain is relatively coarse compared to the resolution of the Mann box: Generally, it is advised to use a grid resolution 2-4 times higher than the resolution of the Mann box. Here the grid is only approximately 1.25 higher, which is likely to have an effect.

A more thorough look at the interaction of grid and inflow turbulence is presented in section 6.2. Using a turbulence box computed with the parameters shown in Table 3.5 and scaling to a TI of $I = 2.5\%$ then yields a progression of the time-averaged center-line TI as depicted in Figure 3.7.

The progression of the TI with an increase in the first half of the domain seems non-intuitive. However, the TI is not uniform in a turbulence box and, hence, variations may occur. Additionally, no strong dissipation was found at the inlet, which has been shown to occur for some turbulence boxes as described in section 6.2. In the following, to stress the difference between the TI of the synthetic turbulence box and the TI that is present in the simulated flow field, the inflow turbulence level of the Mann box is denoted as I_{in}

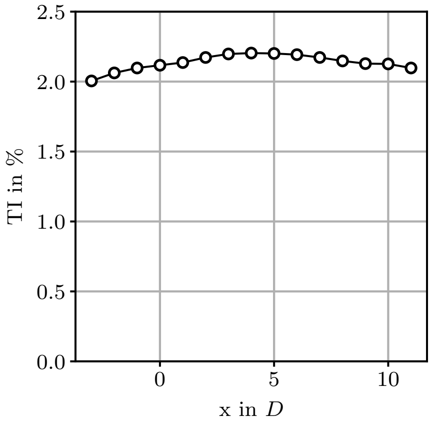

Figure 3.7: Time averaged center-line turbulence intensity for an empty box at an inflow TI of $I_{in} = 2.5\%$

3.7 INFLUENCE OF GRID PARTITIONING

For the simulation of CFD cases with high cell numbers parallel computing can be leveraged. The computation is split between different cores and nodes, and the results of subsets of the linear systems then have to be re-combined. Hence there are interfaces between cores and nodes, where data is transferred.

This process is dependent on the implementation of the parallelization. It has been shown previously that some CFD codes suffer from non-repeatability, when the partitioning is changed, which would occur when changing the number of cores used.

Hence, in order to make sure that results are consistent for different numbers of cores, which allows for using mixed resources on the cluster, a study has been done to investigate, whether the current setup in YALES2 produces consistent results for different partitioning.

Figure 3.8 shows a time instant of two simulations on the same flow case, only differing by the number of cores in use. No visual differences can be found and to the eye, the flow cases are identical.

To further investigate whether there are any differences, the velocity field has been sampled $2D$ behind the rotor in the same simulations, which is depicted in Figure 3.9.

As shown in Figure 3.9 a), the stream-wise velocity signals are identical. This implies, that errors as a result of grid partitioning are so small, that no differences in the flow structures occur. Hence, the statistics will be the same for both cases. Figure 3.9 b) shows the deviation between the two signals. The difference, or error, is zero up to the write precision of 10^{-16} (double precision).

To conclude, no difference can be found when varying the number of cores to compute the flow, which results in different grid partitioning. This allows for comparing simulations run on different numbers of cores and, hence, better use of the available computational resources.

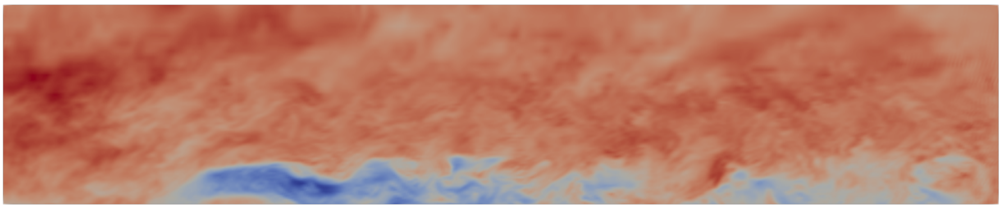

(a) $n_{cores} = 20$

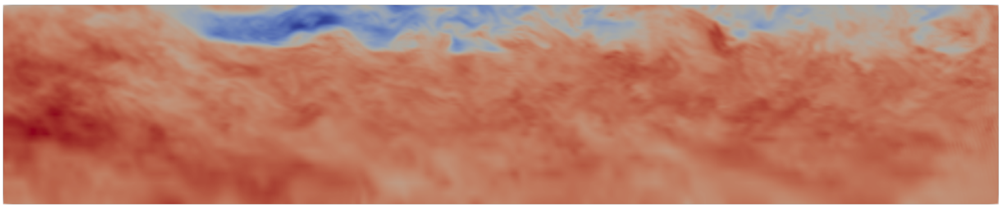

(b) $n_{cores} = 40$

Figure 3.8: Comparison of the streamwise velocity (u_x) field between simulations conducted with different numbers of cores. The cases are identical in initial and boundary conditions, and only differ by the number of cores. The given instantaneous fields are at the same time instance. The upper figure (a) is mirrored in the horizontal plane, such that a comparison is easier to make.

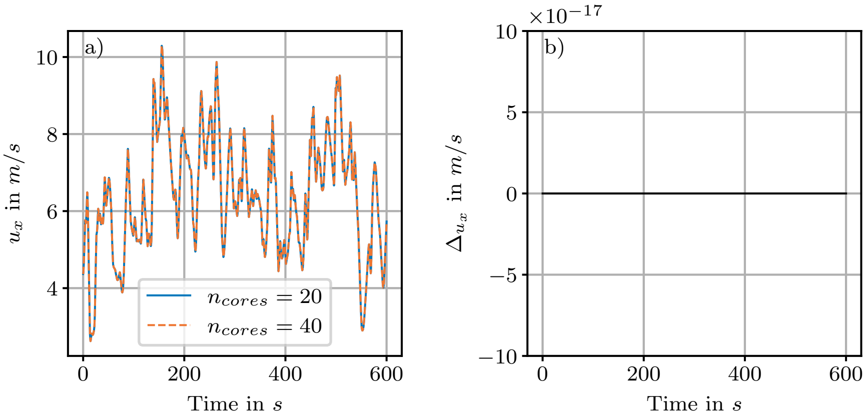

Figure 3.9: (a) Comparison of the velocity component u_x at a probe at location $2D$ downstream of the rotor and (b) difference of the stream-wise velocity time series for different partitioning

3.8 GRID INDEPENDENCE STUDY

Following the thoughts of George Box, every model contains a level of error. In CFD studies, there are various error sources. In the current setup, spacial and time discretization, discretization of the actuator line, smearing of the forces as well as errors of the used airfoil polars are considered leading error terms.

In the context of CFD, in order to gauge the errors due to the discretization, a mesh independence study is crucial. Even when a previous study on a similar mesh can be used as an initial guideline, the error is dependent on the general setup / code including the discretization, and hence has to be repeated for the current combination of mesh and CFD-code.

3.8.1 CONVERGENCE OF THRUST AND POWER

Within this study, it is anticipated, that structured (hexahedral) grids with high resolutions might exceed the available computational resources, and an unstructured (tetrahedral) mesh with stronger grading, and hence, lower computational cost, would be a backup option. The grid independence study will therefore serve a dual purpose: Firstly, it conveys an idea of the order of the error for the grids that are used. Secondly, it will also show how structured and unstructured meshes compare in YALES2 and whether the added numerical cost of structured grids is justified.

A preliminary mesh convergence study over five mesh levels has been conducted on an unstructured grid, with its' topology taken from Combette, 2023 and refinement to reach the number of actuator points as given in the table. Results with this mesh topology are shown in Table 3.6. Additionally, three cartesian grids with a resolution at the rotor of $dx = R/16$ (baseline), $dx = R/24$, and $dx = R/32$ were tested in the same fashion. As a reference, results for the steady-state BEM solver *HAWC2S* were added.

dx/R	ALM points	Thrust (MN)	Power (MW)	C_T	C_P	Grid	Method
	11	1.796	13.10	0.9037	0.5783	tet	CFD
	22	1.745	12.16	0.8780	0.53	tet	CFD
	26	1.728	11.96	0.8696	0.5235	tet	CFD
	31	1.719	11.64	0.8648	0.5137	tet	CFD
	43	1.705	11.43	0.8579	0.5044	tet	CFD
16	14	1.761	12.42	0.8858	0.5482	hex	CFD
24	22	1.715	11.62	0.8629	0.5127	hex	CFD
32	30	1.686	11.10	0.8480	0.4899	hex	CFD
-	-	1.661	10.90	0.8399	0.4832	-	BEM

Table 3.6: Power and thrust for a fixed turbine in laminar inflow on various meshes, including unstructured ("tet"), and structured ("hex") meshes. For comparison, results from the BEM-code HAWC2S are given.

Firstly, Table 3.6 shows a general difference between unstructured and structured meshes. In YALES2, to compute the number of actuator points to discretize the actuator line, the cell edge length is sampled from the mesh. Therefore the number of actuator points is directly dependent on grid resolution. As a result, the number of actuator points is a direct indicator of the grid size. Additionally, considering the lower volume of a regular tetrahedron with the same edge length as a hexahedron, the number of cells is increased for the unstructured mesh. Note that no direct comparison of the mesh sizes is possible, as the unstructured and structured meshes differ greatly in their topology. Results show that at a comparable resolution of the grid, the structured mesh yields results closer to those of higher resolution computations on an unstructured mesh and those of BEM. Overall, it is clear that both, power and thrust (and their coefficients) reduce with increasing mesh resolution, for both mesh topologies.

In general, the overproduction of thrust and power is very significant. More precisely, they reach levels beyond analytical boundaries: Analytically derived from momentum theory, the Betz limit provides an estimate of the theoretical upper limit for thrust and power coefficients. Assuming steady, inviscid, incompressible, and constant internal energy, the limit has been derived to reach values as shown in Equation 3.4. While in most applications not all these assumptions are met, until now it holds as a theoretical limit for the power production in all practical applications, with e.g. Porté-Agel et al., 2019 reporting that real HAWTs reach a power coefficient up to 0.5.

$$a_{Betz} = 1/3 = 0.33 \qquad C_{T,Betz} = {}^{8}\!/_{9} \approx 0.89 \qquad C_{P,Betz} = {}^{16}\!/_{27} = 0.59 \tag{3.4}$$

Exceeding the Betz limit is critical, as it shows that the actuator does not fully represent the physical behavior of the wind turbine anymore. High thrust coefficients can change the wake state of a stream tube. A high power coefficient is related to a significantly amplified wake rotation. Both these will have an impact on the wake. The thrust coefficient is over-predicted by approximately 5%, while the power coefficient is over-predicted by circa 13% when compared to the *BEM* computation for the cartesian mesh with $dx = R/16$ resolution.

The change in thrust and power coefficients with changing grid resolution is quite high in comparison to other studies, as e.g. Hodgson, Andersen, et al., 2021 who reported a maximum of 1% difference of the thrust coefficient between highest resolution ($dx = R/64$) and the resolution comparable to the current study ($dx = R/16$), while in the current computations, this difference is 12 % (between meshes $dx = R/16$ and $dx = R/32$). It is likely that this is related to the correction methods for the inflow angle, as described in section 2.2

It can be argued, that while it is crucial to obtain a representative thrust coefficient, the power coefficient is of lower importance, as relevant wake effects can still be found in experiments using an actuator disc without any power. However, the influence of a high wake rotation due to the large overproduction of power is unknown.
Additionally, the high thrust coefficient is expected to influence the results of the study.

3.8.2 Grid Convergence Index

In order to further quantify the convergence of the, the Grid convergence index (GCI) has been computed. It is a measure based on Richardson extrapolation Richardson and Glazebrook, 1910, which is a technique to provide an estimate for a grid-independent value from two or more grid-dependent computations at different mesh levels, while taking into account the refinement ratio and the order of convergence.

A routine to compute the GCI was implemented, following the suggestions in Celik et al., 2008.

$$GCI_{fine} = \frac{1.25|\epsilon|}{(r^p - 1)} \tag{3.5}$$

Additionally, as in NASA, 2024, the GCI computation for the coarse grid was done as follows:

$$GCI_{coarse} = \frac{1.25r^p|\epsilon|}{(r^p - 1)} \tag{3.6}$$

where r represents the refinement ratio, p the order of convergence, and ϵ the error between the grid levels.

The computations of the GCI for simulations on the three structured meshes are shown in Table 3.7.

Mesh	$GCI(C_T)$	$GCI(C_P)$
16	32.1%	76.3 %
24	29.8%	70.2 %
32	28.1%	67.7 %

Table 3.7: GCI error estimates for thrust and power coefficient for 3 different structured meshes

From Table 3.7 it is apparent, that there is a high grid dependency and the error based on the mesh is quite high, with a GCI of 32.1% and 76.3% for the thrust and power coefficients respectively for the baseline mesh with $dx = R/16$. Striking is, that even for the highest grid resolution, the GCI is still very high.

It is clear that there is no quantitative indicator of the mesh being sufficiently fine for the attempted study. The GCI is high, showing strong grid dependence of the results, and an overproduction of power and thrust is found.

Based on Hodgson, M. H. A. Madsen, et al., 2023 and Troldborg, 2009, one can argue that generally, a mesh of $dx = R/16$ is sufficient to capture the shear layer, while not resolving the tip vortices. Arguing in this line, resolution should be sufficient to capture the general tendencies of the flow. However, this is dependent on the CFD code in use.

Previous studies, e.g. by Benard et al., 2018, Houtin—Mongrolle et al., 2021 show that YALES2 is capable of capturing the flow physics well, comparable to other codes and ALM implementations. However, all these have been done on grids with far higher resolution. IThe current project stretches the application range of the numerical setup due to the low resolution of the ALM model.

The GCI also shows, that even for the higher resolution ($dx = R/32$) which, according to the previously mentioned studies, would be able to resolve the tip vortices, the error for the thrust and power coefficients is still high. A possible explanation is, that the ALM model itself is highly grid dependent. The error therefore comprises both the error coming from discretization of the finite volume domain, but also the error introduced by the coarsely resolved actuator, where the kernel distributing forces around the blade is dependent on the grid size as well.

In order to further isolate these different error sources, a fixed number of actuator points could be used while only varying the grid resolution. This approach, however, would still not be able to isolate the effect of the kernel, as it is dependent on the cell size. Further studies would be required, to predict the dependence on the smearing kernel.

The strong dependence of the power and thrust coefficients on the mesh is a common problem in ALM simulations. As pointed out in Meyer Forsting, Pirrung, et al., 2019, due to the smearing of the forces in order to mitigate numerical instability, self-induction is changed when compared to a singular force. As a result, an error in the angle of attack computation is introduced, which then leads to a change in the force coefficients. This process is grid-dependent, and hence, overprediction of the loads is tied to the grid size.

In order to mitigate this issue, correction methods have been developed: Meyer Forsting, Pirrung, et al., 2019 showed an improvement of the actuator line model by applying a smearing correction based on Lifting line (LL) theory. Separately, Martínez-Tossas and Meneveau, 2019 developed a LL based correction for the force smearing. YALES2 provides an implementation of the correction method by Martínez-Tossas and Meneveau, 2019.

At the current time, no scientific publications exist that evaluate the performance of the correction features in YALES2, and, hence, the features are considered as in development. In order to investigate, whether performance can be improved in the current case using the LL-correction, a low-resolution computation was done to compare to higher resolution results, which is shown in Figure 3.10.

Using the implementation of the filtered LL-correction (Martínez-Tossas and Meneveau, 2019), reduction of the forces near root and tip could be found. However, for the tangential force, the force increases for the last point of the actuator line. This behavior is unanticipated and further research would be required in order to find out, whether this is an issue with setting up the correction from the user-level inputs. Hence, overall improvement using this model was doubted. This leads to the project proceeding with the uncorrected model.

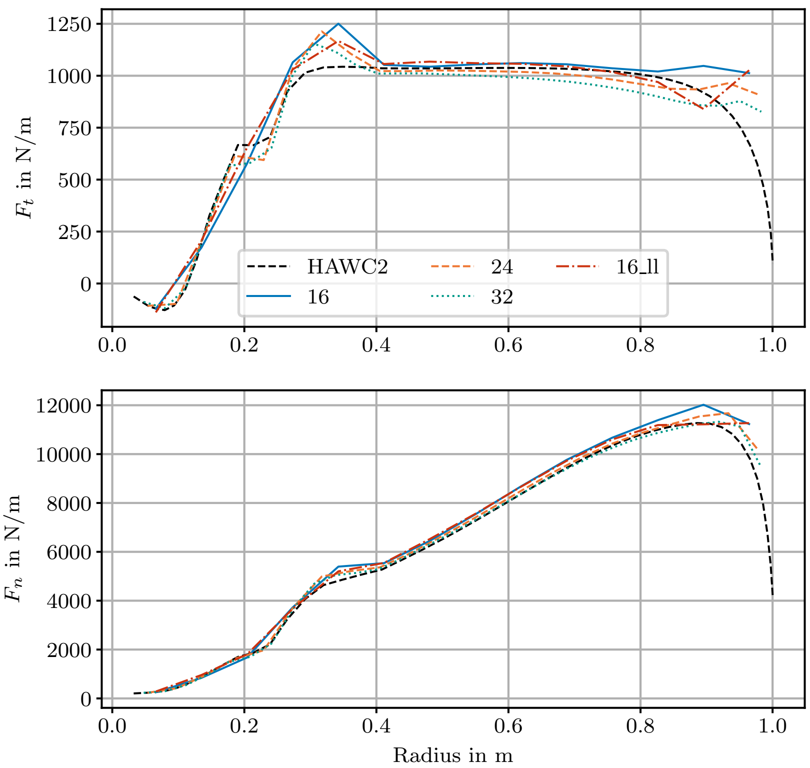

Figure 3.10: Comparison of the loads along the blade span, including different structured meshes $dx = R/16$ ("16"), $dx = R/24$ ("24"), $dx = R/32$ ("32"), filtered-LL correction method ("16_ll") and results from HAWC2 as a reference

Concluding the grid independence study, a strong dependence of the results on the grid has been found. It is argued that this is largely associated with the actuator line model not performing well in the current setup due to the low resolution. Thrust and power are very high compared to BEM results.

3.9 SIMULATION TIMES

In the previous section, it has been shown that the results are grid-dependent, and higher mesh resolutions would be desirable. When the mesh size is increased, the degrees of freedom in the linear system increase, and, hence, larger effort is required in order to solve the linearized system, which leads to longer simulation times. Adding further complexity to the simulations, like input, output, and write operations then increases the computational cost additionally.

Within numerical studies, simulation cost is a driving factor deciding the feasibility of a planned study. In the context of this study, it is expected, that for a fixed turbine with laminar inflow, simulation times will be significantly lower than for a moving turbine with turbulent inflow, which is the target setup. This is due to several reasons:

- For the final simulations, larger amounts of data are of interest, and, hence, write operations of large amounts of data are required and slow down the simulations.
- For the turbulent simulations, additional mathematical operations are required to map the turbulent field to the inlet boundary, and the same is true for adding the motion.

As a result, there needs to be overhead planned, in order to finalize the more complex simulations in time.
Simulated times need to be long: Not only does the simulation need to "converge", in this case meaning converged power and thrust values over time. As the intention is to analyze the wake, the changed thrust and power need to fully propagate through the whole wake, such that at least one full flow through the domain is required to resolve this transient. Only after that, a sufficient time series can be sampled in order to depict the full dynamics of the flow.

To elaborate on the dependence of the simulation times on the conditions, Table 3.8 shows the simulation times for multiple cases.

Motion	TI in %	Nodes × Cores	Simulation time in h
Fixed	0	1x20	41
Fixed	5	1x20	49
Fixed	5	2x20	39
A/D= 0.04, St=0.4	0	1x20	38
A/D= 0.04, St=0.4	5	2x20	42
A/D= 0.32, St=0.4	0	1x20	41
A/D= 0.32, St=0.4	5	2x20	38

Table 3.8: Simulation times for selected simulations. Simulation times are given as the time required to simulate a 10-minute time series of the flow.

It is apparent, that the floating motion has negligible influence on the simulation cost, but the introduction of the turbulent inflow condition does have a significant impact. YALES2 is able to provide detailed information on the contributions to the duration of the iterations. Comparing the two cases (first two rows of Table 3.8) reveals that the increase in simulation time has its' origin in more required time for the pressure correction.

If the grid resolution is increased, computational effort increases rapidly, e.g. when going from a resolution of $dx = R/16$ to $dx = R/32$ increases the number of cells by a factor of 8, and the number of iterations by a factor of 2, leading to an increase of computational cost with a factor of 16. This increased computational cost can be compensated by using more cores in the parallel computations. However, in the current project, this surpasses the available resources, considering the number of simulations that are required.

3.10 Mesh Selection

To conclude, for the study the mesh with $dx = R/16$ was chosen. This choice is mainly driven by the limitations of the computational resources. There are points to argue for the sufficiency of the mesh, like previous studies showing that overall breakdown behavior and shear layer can be depicted at these resolutions. However, there are also factors limiting trust in the model: Firstly the high power and thrust coefficients are very near the theoretical limit. Secondly, the convergence of these is poor with increasing grid resolution, which was attributed to the discretization of the ALM. However, to cover a large enough parameter space and have a sufficiently large simulated time series, the project goes forward with this low-resolution grid approach, being critically aware of the flaws of the current setup In the following, a validation against reference data is done in section 4.1, to show whether the model setup is still useful in order to represent overall trends.

The velocity magnitude field and mean velocity Root mean square (RMS) are depicted in Figure 3.11 and Figure 3.12 for the final setup with the grid resolution of $dx = R/16$ and a inflow turbulence of 0%.

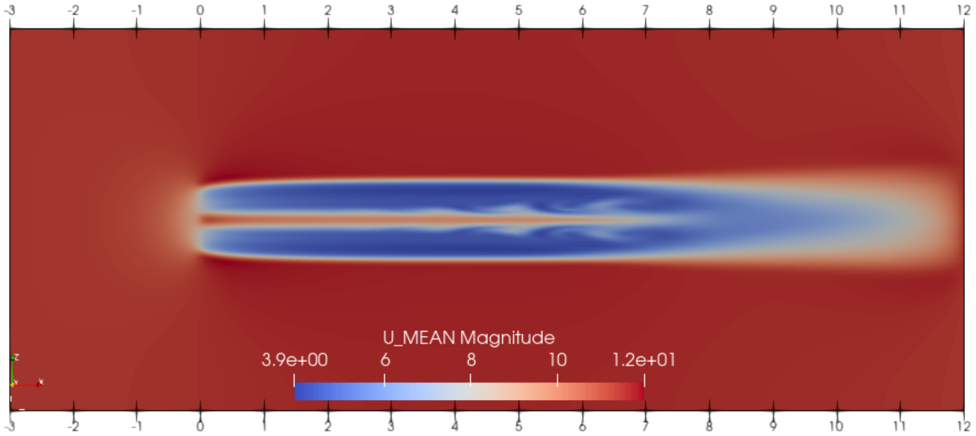

Figure 3.11: Velocity magnitude field a fixed turbine with inflow turbulence $I = 0\%$

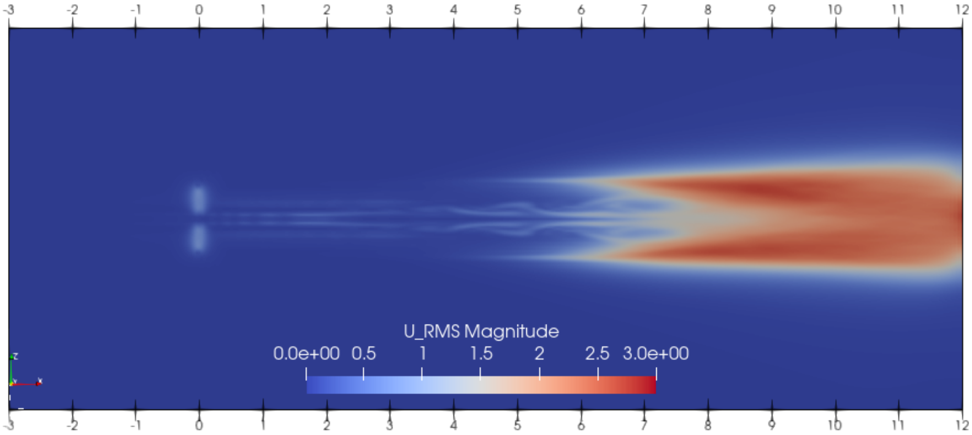

Figure 3.12: Velocity RMS magnitude field a fixed turbine with inflow turbulence $I = 0\%$

3.11 GLOBAL POD

When multiple different data locations or flow cases should be compared using proper orthogonal decomposition (POD), it is possible to utilize a *global POD*, following Andersen and Murcia Leon, 2022. The idea is to generate a data matrix that contains snapshots from different locations and/or cases. This way, a unified basis is generated, that describes modes in terms of most variance across the whole data set. This way, different locations, and cases can be compared directly with a single POD basis.

For a given flow case, cross-flow planes centered around the rotor and spaced 1D apart are sampled, as visualized in Figure 3.13.

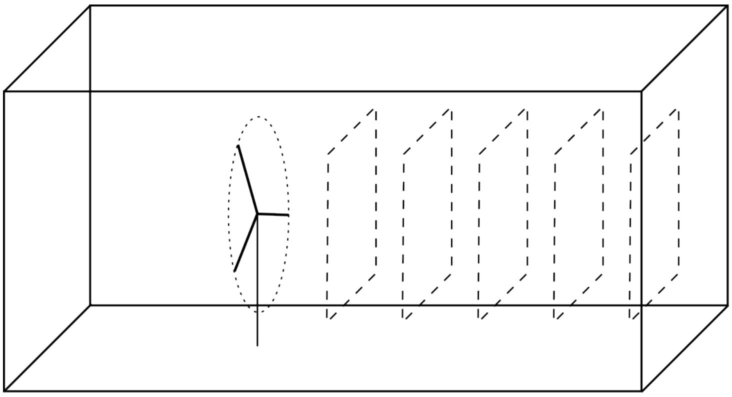

Figure 3.13: Cross-flow planes in the wake sampled for the POD analysis

A data matrix M is constructed by stacking data from multiple cases, plane positions and time steps in the second dimension of the data matrix as follows:

$$\left[(S_0 \dots S_{n_t})_{P_1} \dots (S_0 \dots S_{n_t})_{P_{n_p}}\right]_{C_1} \dots \left[(S_0 \dots S_{n_t})_{P_1} \dots (S_0 \dots S_{n_t})_{P_{n_p}}\right]_{C_{n_c}} \tag{3.7}$$

for the planes P and cases C with n_t time steps, n_p planes, and n_c cases. This way the matrix stacks snapshots column vectors in time at different planes and across different flow cases along the horizontal of the data matrix. This yields a data matrix of shape $3n_y n_z \times n_t n_c n_p$ that can then be used in the usual POD procedure.

3.11.1 CORRELATIONS OF MODAL TIME SERIES

In the context of POD, correlations can be used to show the relations between modal time series of different modes, planes, and flow cases. When a POD basis is created, the modes are, per definition, uncorrelated due to their orthogonality. However, if a modal time series is created by projecting a velocity field sampled with high frequency onto the POD basis, then correlations do appear between different modes.

The correlation coefficient is computed as:

$$\rho_{XY}(\tau_{lag}) = \frac{\sum(X_t - \mu_X)(Y_{t+\tau_{lag}} - \mu_Y)}{\sigma_X \sigma_Y} \tag{3.8}$$

for the signals X and Y, with their mean μ and standard deviation σ and a time lag τ_{lag}. Using the correlation different phenomena could potentially be shown:

1. Choosing signals X and Y as modal time series for two different modes from a single case on a single plane reveals if two modes might be both relevant for resolving certain structures.

2. Choosing signals X and Y as modal time series of the same mode and flow case, but different planar positions. This may yield information about the coherence of flow structures as they advect through the domain. If a flow structure persists over a long downstream distance, then the correlation is high for larger downstream distances.

3. Choosing X and Y as the modal time series of the same mode on a single plane and varying the flow cases. This conveys information on how far cases are similar. When there is little disturbance, and boundary conditions are the same, generally the same flow structures should develop. If that is not the case, it is a sign of high disturbance of the flow and, hence, a large influence of different motion or turbulent conditions.

3.12 EIGENVALUE CONVERGENCE OF POD MODES

Generally, POD should be used on a data matrix consisting of independent snapshots. To ensure the independence of the samples, often a definition based on the integral time scale is chosen. The definition of the integral time scale is not trivial, as due to the wind turbine motion there is a periodic content in the signal. Hence, the surge period T_s is used as a reference time for the large scale, which can be computed as shown in Equation 3.9.

$$T_s = \frac{D}{U_\infty St} = 39.1s \tag{3.9}$$

The Strouhal number of 0.4 leads to a frequency of turbine oscillation of approximately 0.026 Hz or a period of 39.1s respectively. As noted by Troldborg, 2009, it is necessary to use independent snapshots, in order to capture the second-order statistics. However, as the available data is limited, large spacing of the data leads to less data in the POD. A pre-study is conducted in order to investigate the influence of different sample frequencies and data sizes on the generation of the POD basis. The influence of the spacing between the sampled snapshots is presented in Figure 3.14.

Figure 3.14 shows how the energy in the eigenvalues of the global POD modes change with a change in the sampling frequency of the snapshots used to create the data matrix.

For large time steps between the samples, a slight shift of the cumulative energy in the first modes upwards can be seen. As shown in the appendix Figure 6.6, the modal basis appears grainy and

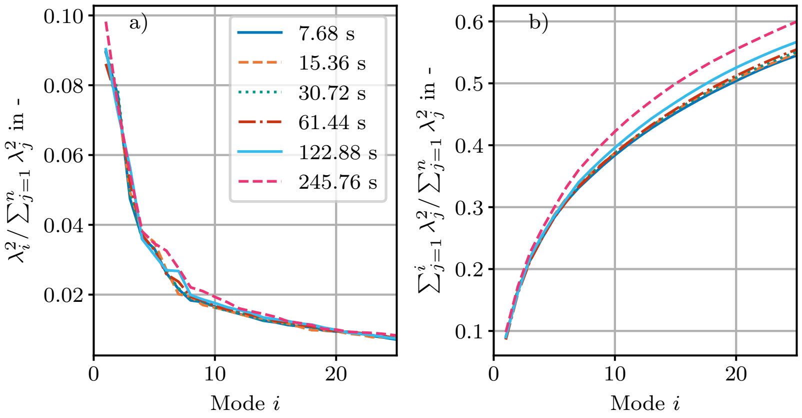

Figure 3.14: Relative energy content of the POD modes, where a) presents the relative contributions of a mode i to the energy in the global POD database from Table 4.5 and b) shows the cumulative energy contribution of the modes up to mode i

less smooth. This hints towards that the number of included samples is too low.

When the sampling time step increases, differences reduce and the energy in the modes of interest (the first 25) converge. This shows, that the influence of high sampling and, hence, statistically non-independent samples does not affect the basis noticeably.

Going forward, the sample period of 30.72 (equal to sampling every 512th time step) is chosen, as the eigenvalues are in the "converged bulk", the POD basis appears smooth and the amount of data to construct the basis is smaller than for any higher time resolution basis.

4 RESULTS

This section depicts results made in the course of the study. First, the setup is validated against a reference study in section 4.1, in order to show the model's capabilities. For the validation, a sway (side-side) motion case is used, as direct comparisons to the reference are possible. However, the remainder of the computations then concentrate on surge (fore-aft) motion: section 4.2 presents the influence of the surge amplitude on the wake, while section 4.3 covers the influence of surge frequencies.

4.1 VALIDATION

As previously the models' several flaws have been elaborated, this section is concerned with showing, how well the model can still capture the overall behavior of the flow. In order to do that, current sway simulation results are compared to the results by Z. Li et al., 2022.

The reference paper is concerned with the sway (side-side) motion of a floating wind turbine. The reference motion conditions are depicted in Table 4.1. As in the reference, the inflow turbulence level is then varied.

Parameter	Value
St	0.25
A/D	0.4

Table 4.1: Parameters used for the validation study. Values in comparison to Z. Li et al., 2022

The time- and rotor-averaged velocity deficit ${}^{\Delta U}/_{U_\infty}$ has been computed for simulations with inflow TI levels of 0%, 2.5%, and 5% using Equation 4.1.
Additionally, reference values were taken from Z. Li et al., 2022 at inflow turbulence intensity levels of 0%, 1.5%, and 4.7%.

$$\Delta U = \overline{U_{Rotor}} - U_\infty \tag{4.1}$$

with the free stream velocity U_∞. All these are depicted in Figure 4.1.

For the same flow cases, the time- and rotor-averaged turbulence intensity in the wake has been computed as follows:

$$I = \frac{\sqrt{{}^{2}/_{3} k_r}}{U_\infty} \tag{4.2}$$

with the resolved turbulent kinetic energy:

$$k_r = \sigma_{u_x}^2 + \sigma_{u_y}^2 + \sigma_{u_z}^2 \tag{4.3}$$

using the standard deviations σ of the velocity components u_x, u_y, and u_z. The current results as well as the reference values are depicted in Figure 4.2

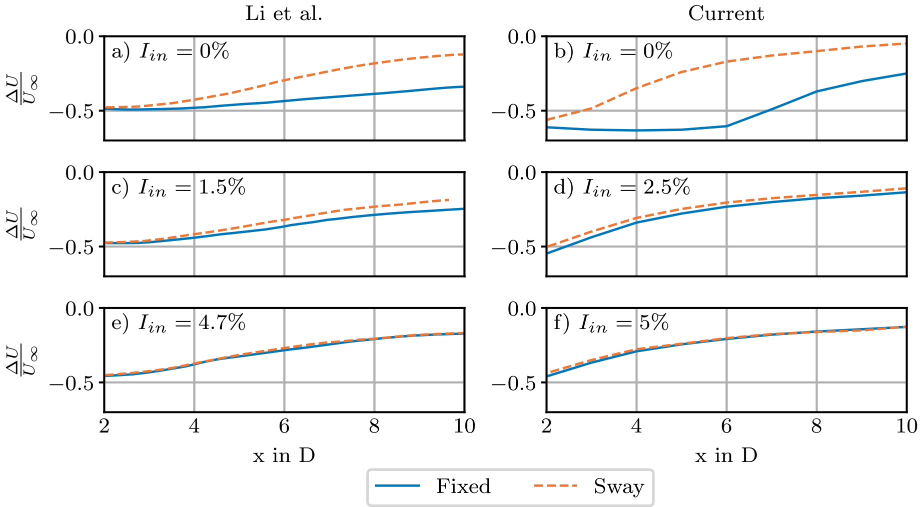

Figure 4.1: Rotor- and time-averaged velocity deficit $\frac{\Delta U}{U_\infty}$ as a function of the downstream distance from the rotor. Data in figures a), c), and e) are taken from Z. Li et al., 2022, while b), d), and f) are computed in the current study. With a) and b) $I_{in} = 0\%$, c) $I_{in} = 1.5\%$, d) $I_{in} = 2.5\%$, e) $I_{in} = 4.7\%$, f) $I_{in} = 5\%$

Comparisons are to the reference are made to find out, whether the current setup shows similar wake statistics and captures the overall trend for the increase in inflow TIs.

Comparing current results Figure 4.1 b) to the literature reference Figure 4.1 a) at an inflow TI of 0%, large differences can be seen: For reference a), the deficit is identical between fixed and moving turbine at the rotor, while differences grow in the downstream direction. The deficit recovers faster for the moving turbine. In the current computation b), the wake deficit differs significantly between the fixed and moving case at all stream-wise positions. At the rotor plane, the results of the current study show a larger velocity deficit for both fixed and swaying turbine case, although they reach a similar level as the reference further downstream.

When turbulence is introduced, the differences between fixed and swaying turbine rapidly reduce: In the lower TI case (c) $I = 1.5\%$) in the reference, differences between moving and fixed turbine have become very small. Overall the deficit is smaller at 10D downstream than for the moving case in laminar inflow, but higher for a fixed case in laminar inflow.
The same occurs in the current case depicted in d). Differences between moving and fixed turbine wake deficits become smaller both in the reference and in the current study.

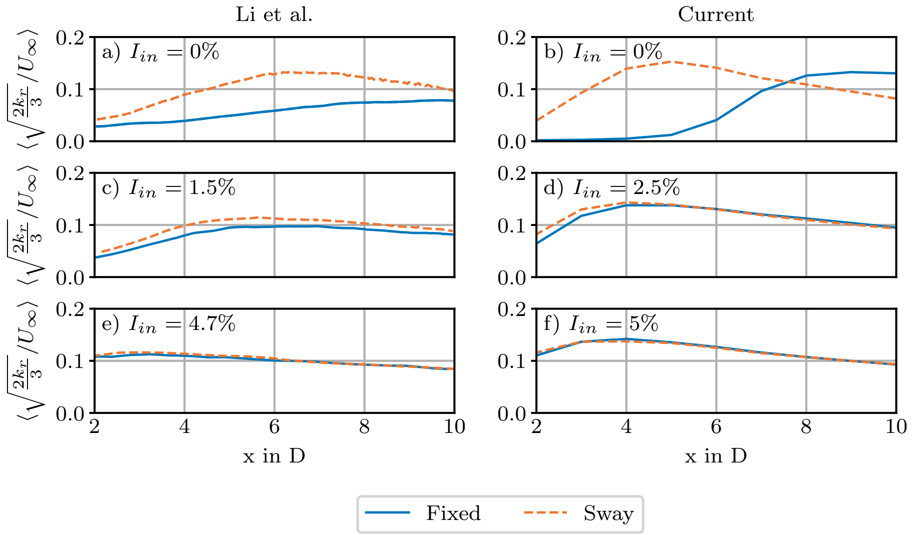

Figure 4.2: Rotor- and time-averaged turbulence intensity as a function of the downstream distance from the rotor. Data in figures a), c), and e) are taken from Z. Li et al., 2022, while b), d), and f) are computed in the current study. With a) and b) $I_{in} = 0\%$, c) $I_{in} = 1.5\%$, d) $I_{in} = 2.5\%$, e) $I_{in} = 4.7\%$, f) $I_{in} = 5\%$

Generally, due to the high thrust coefficient in the current study, the deficit should be directly affected, and should generally be stronger. It seems that when inflow turbulence is present, also the differences between the current simulations and the literature reference are reduced. This seems to happen, despite the different thrust coefficients.

When looking at the development of TI in the wake in Figure 4.2, the same overall trends are shown. At an inflow turbulence level $I_{in} = 0\%$, there is quite a difference between fixed and moving turbine in both the reference case (a), and current results (b). For an increasing inflow TI, both the reference and the current results show reducing differences between moving and fixed turbine. In general, the point of maximum TI in the wake shifts upstream for higher inflow TI levels. Again, this is true both for the reference as well as the current results.

The lower TI close to the rotor in the current study at TI=0% b) might be a result of the low resolution as well. As the resolution is low, the forces are spread over multiple cells, that is, a larger volume, suppressing high local forces in the individual cells. Hence, the ALM becomes closer to an actuator disc, and the variation of the flow induced by the blades is smaller, as the blades are not smeared further. This is only a possible explanation, and further studies would be required to prove this hypothesis.

Additionally, the higher TI in the wake for the fixed case at the downstream positions might stem from the large-scale meandering that is shown in Figure 4.3.

To conclude the comparison with the literature case, differences exist, especially under laminar inflow conditions. With higher inflow turbulence levels, overall differences are reduced. The overall trends found in the reference - increasing wake recovery for the fixed turbine when the inflow TI is increased, reducing recovery for the sway when the inflow TI is increased, and convergence of the fixed and floating case at higher inflow TI. These are likewise depicted in the current simulations. This, to some extent, shows that the current setup is capable of capturing the overall tendencies of the flow for a swaying turbine in turbulent inflows.

For the current validation, sway motion has been utilized as a direct comparison to previous results by Z. Li et al., 2022 is possible. In the remainder of the report, the focus lies on surge motion.

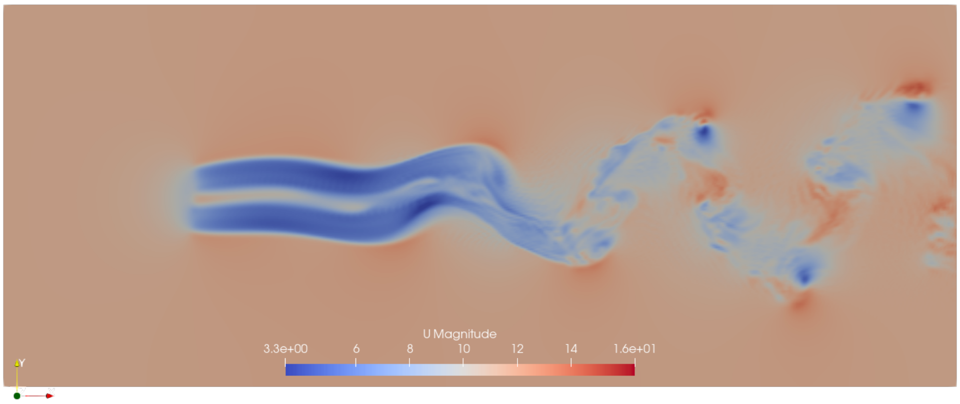

Figure 4.3: Velocity magnitude for the sway case $A/D = 0.04$, $St = 0.25$, $I_{in} = 0\%$

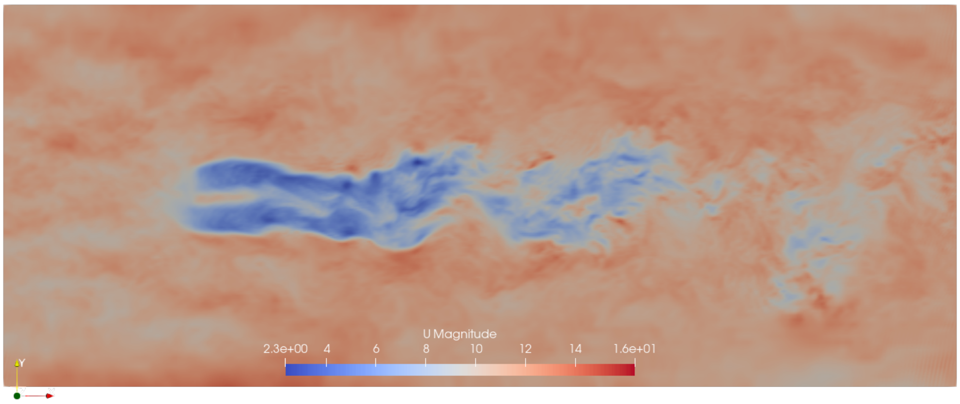

Figure 4.4: Velocity magnitude for the sway case $A/D = 0.04$, $St = 0.25$, $I_{in} = 5\%$

4.2 VARIATION OF THE SURGE AMPLITUDE

This section deals with the change of the wake due to variations of the surge amplitude. As in the previous section, wake deficit and turbulence are being investigated. Additionally, POD is used to analyze the wake flow in terms of energy content in the POD modes, as well as correlations of modal time series in order to highlight similarities and differences of the different flow cases.

The parameters of the surge motion were chosen based on findings of Messmer et al., 2024. For $St = 0.4$ and varying the motion amplitude from $A/D \in [0.01, 0.32]$.

4.2.1 DEFICIT AND TURBULENCE INTENSITY IN THE WAKE

As in the previous section, the velocity deficit and the TI are computed in the wind turbine wake. Figure 4.5 Compares the time-and rotor-averaged velocity deficit at 7 different surge amplitudes for three different turbulence levels. Figure 4.6 depicts a comparison of the time-and rotor-averaged turbulence intensities for the same cases.

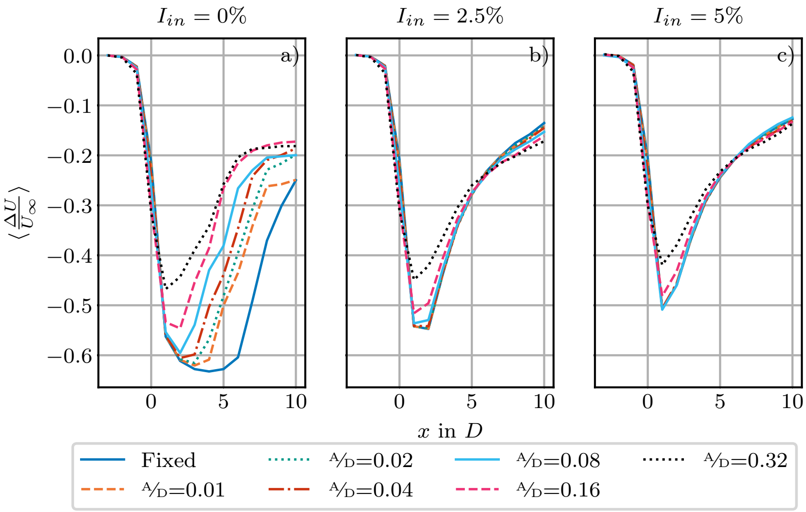

Figure 4.5: Rotor- and time-averaged velocity deficit $\frac{\Delta U}{U_\infty}$ as a function of the downstream distance from the rotor for different motion amplitudes and inflow turbulence intensities. With a) $I_{in} = 0\%$, b) $I_{in} = 2.5\%$, c) $I_{in} = 5\%$

At laminar inflow conditions, the surge motion had an impact on both, wake deficit (Figure 4.5 a)) and wake TI (Figure 4.6 a)). The relations between surge amplitude and deficit are very clear. The fixed turbine case has the largest deficit and needs the longest downstream distance to recover. For increasing amplitude, the deficit then reduces. The point of the highest deficit (lowest value) shifts upstream with increasing amplitude.

When the inflow turbulence is increased to 2.5% (Figure 4.5 b)) the curves largely collapse. Almost no differences can be found up to an amplitude of $A/D = 0.08$. Only for the two cases

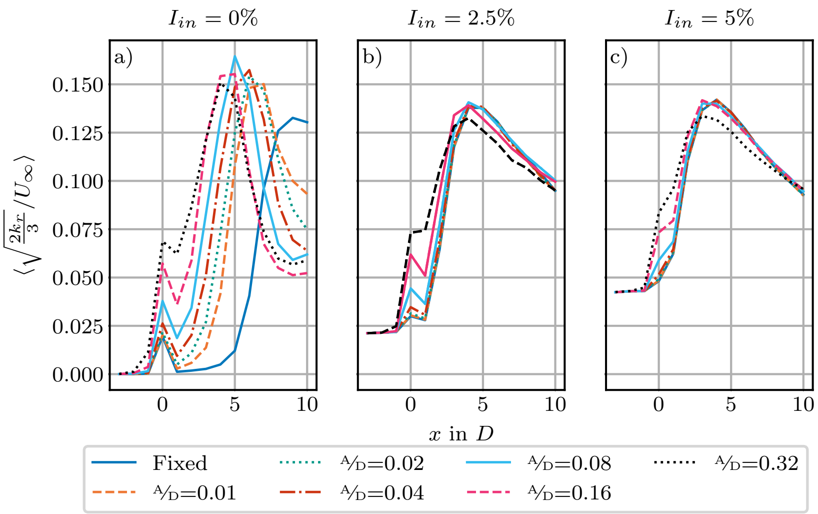

Figure 4.6: Rotor- and time-averaged turbulence intensity $\langle\sqrt{\frac{2k}{3}}\rangle/U_\infty$ as a function of the downstream distance from the rotor for different motion amplitudes and inflow turbulence intensities. With a) $I_{in} = 0\%$, b) $I_{in} = 2.5\%$, c) $I_{in} = 5\%$

with the highest amplitude (0.16 and 0.32) the maximum deficit is reduced, while the deficit still overall follows the same progression.

When TI is further increased to 5% (Figure 4.5 c)), differences due to different amplitudes further reduce.

Looking at the variation of the turbulence intensity in the wake Figure 4.6, a similar progression is found: Differences are large at $TI = 0\%$ (a)) between the different surge amplitude conditions, and results are ordered by amplitude: the higher the amplitude, the further upstream the TI increase happens. When the inflow TI is increased the results generally collapse, and differences are visible only for the high amplitude cases. For the highest TI level (5% in c)), all, but the two largest amplitudes collapse into a single curve.

When turbulence is introduced at the inflow, the simulations collapse. This shows, that the given motion (Amplitude and frequency combination) has little effect on the development of the wake statistics. The turbulence levels are quite low with 2.5% and 5%, but still sufficient to have a large effect on the wake. These results are in agreement with the findings by Z. Li et al., 2022, Ramos-García et al., 2022, and Messmer et al., 2024, that all show that with turbulent inflows, the motion dependency of the wake reduces.

4.2.2 LOADS

As previously found, the motion amplitudes necessary to impact the wake development noticeably in the current numerical framework are very high. The operation of a wind turbine in these

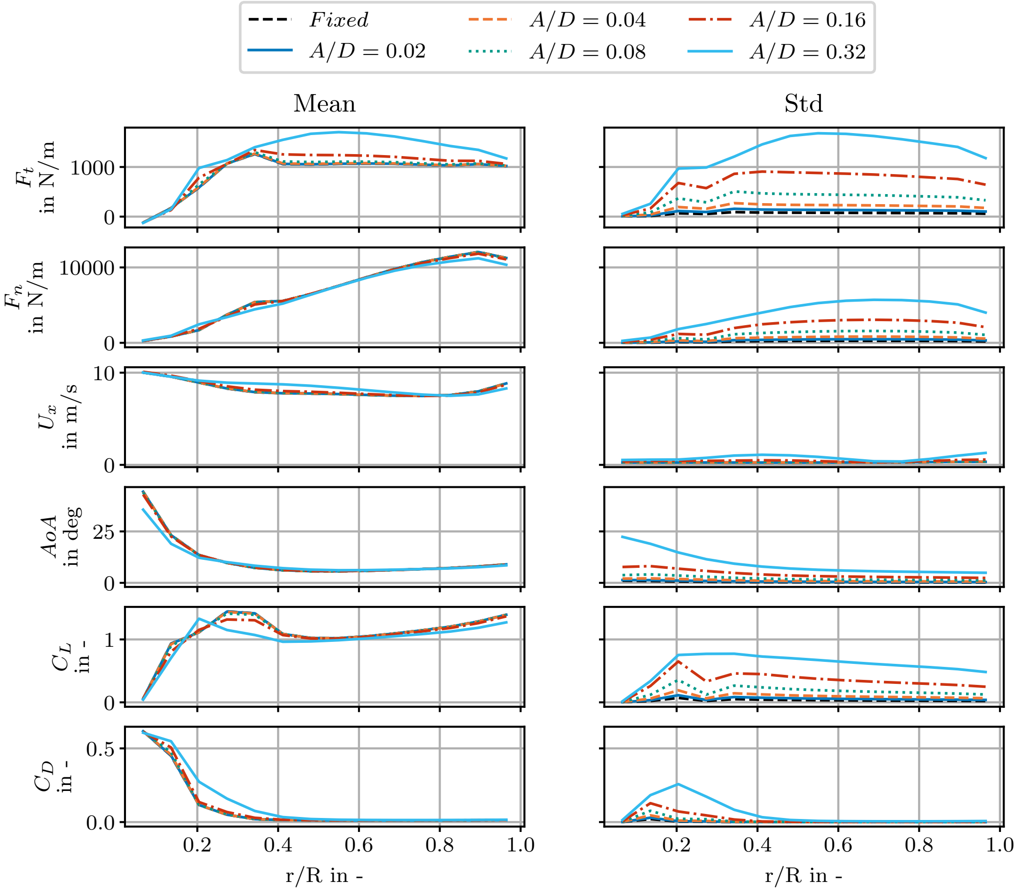

Figure 4.7: Comparison of tangential and normal loads F_t and F_n, sampled velocity for the ALM U_x, angle of attack, and force coefficients C_L and C_D over the non-dimensional radial position r/R for different surge amplitudes

conditions would likely have a substantial impact on the loads. For that reason, the blade loads have been computed

Figure 4.7 shows the spanwise loads and other load-relevant parameters for different spanwise positions, both mean (left) and standard deviation (right).

For the lower amplitudes $A/D = 0.04$ and $A/D = 0.08$, the difference to the fixed turbine is very small in the mean values. Differences occur for the higher amplitudes, where the highest amplitude ($A/D = 0.32$) even shows a different load profile for the in-plane force F_t. The standard deviations in the right column shed light on the influence of the motion on the time-varying loads. An increased surge amplitude is directly correlated to higher load variations, both in the tangential and azimuthal directions. Even for the small amplitude, the standard deviation is significantly increased.

For the large amplitudes $A/D = 0.16$ and $A/D = 0.32$, standard deviations are in the order of magnitude of the mean values. These are considered very high.

This report does not intend to thoroughly investigate loads and yields but rather uses them to outline whether the results can still be considered physical and to gauge, whether the operational conditions are relevant for a real FOWT. More thorough investigations on the loads and power output of a FOWT in a similar setup can be found in Combette, 2023.

For the large load variations, it is clear that firstly, there would be a response of the controller, which is not considered in the current setup. Secondly, aero-elasticity would likely come into play. Lastly, the load conditions found here will have significantly increased the fatigue loads, and hence, a turbine would not operate in these conditions.

As a result, it is clear that the high amplitude computations can be considered academic edge cases and their only purpose is to approximate, how much rotor motion is required to make a difference in the wake characteristics.

To further shed light on the operational conditions, thrust and power coefficients (time average and standard deviation) have been computed and are depicted in Table 4.2

A/D	TI	$\langle C_T \rangle$	$\sqrt{\langle C_T'^2 \rangle}$	$\langle C_P \rangle$	$\sqrt{\langle C_P'^2 \rangle}$
0	2.5%	0.89	0.018	0.55	0.026
0.04	2.5%	0.89	0.073	0.56	0.109
0.08	2.5%	0.89	0.141	0.57	0.211
0.16	2.5%	0.88	0.274	0.62	0.412
0.32	2.5%	0.86	0.50	0.77	0.750
0	5%	0.89	0.034	0.56	0.052
0.04	5%	0.89	0.080	0.56	0.119
0.08	5%	0.89	0.138	0.57	0.207
0.16	5%	0.88	0.276	0.62	0.416
0.32	5%	0.86	0.501	0.77	0.751

Table 4.2: Variation of the mean and standard deviation of the power and thrust coefficients for different surging cases at $St = 0.4$, varying surge amplitude and inflow TI

Generally the deficit in the wind turbine wake is directly dependent on the load of the rotor on the flow. In order to compare wakes, the thrust and power coefficients need to be in a similar range. Table 4.2 shows the thrust and power coefficients dependent on the surge motion amplitude and inflow TI levels. It is apparent that overall a thrust reduction of up to 3.5% with increasing motion amplitude is present for the two inflow TI levels. It can also be seen that the power coefficient is increased significantly at the highest amplitudes. The standard deviations of both thrust and power coefficient increase almost linearly with the motion amplitude, which is in line with the findings of the standard deviations in Figure 4.7.

Generally a reduction of thrust and increase of power would be desired outcomes. However, looking at the standard deviations reveals, that for the high amplitudes, they are in the order of magnitude of the mean value. This, again, shows that the load variations are very high, and turbine controls would come into play long before reaching these conditions.
The development of wakes is sensitive to operational conditions like power and thrust coefficient. If the thrust coefficients differ, the comparability of the wakes is affected. This might affect the results of the wake deficit and TI previously and might be part of the explanation as to why the highest amplitude cases differ from the lower amplitude ones. Messmer et al., 2024 could circumnavigate this issue by keeping the thrust coefficient constant. A comparable isolation cannot be made in this case, as the thrust is dependent on the numerically computed forces from the actuator line model.
Further Table 4.2 shows that the thrust coefficient reaches Betz-limit. For high amplitude cases, the power coefficient even exceeds the Betz-limit. There are multiple possible reasons for this. Firstly, it was shown previously in the grid study, that both coefficients are grid-dependent in the whole range of grid resolutions tested in this project. The chosen resolution of $R/dx = 16$ is quite coarse and leads to high thrust and power coefficients. This may be attributed to the smearing kernel used and the smearing length scale. As previously discussed, in more advanced actuator line models corrections would be used to reduce the grid dependency.

Another possible explanation for these effects might be the power added to the flow by the motion of the rotor, which is discussed in the following section.

4.2.3 ADDED POWER

It is found that the increasing power coefficient is directly connected to increasing the surge motion. The power coefficient is only increased drastically for the two highest amplitude cases $A/D = 0.16$ and $A/D = 0.32$.

The large amplitudes and surge velocities dynamically change the inflow conditions at the rotor. The surge velocities can be directly obtained from the sinusoidal motion and are presented for different combinations of amplitude and surge frequency in Table 4.3.

A/D	St	v_{max}	v_{max}/U_∞
0.01	0.4	0.2865	0.0251
0.02	0.4	0.573	0.0503
0.04	0.2	0.573	0.0503
	0.4	1.1461	0.1005
	0.6	1.7191	0.1508
	0.8	2.2921	0.2011
0.08	0.4	2.2921	0.2011
0.16	0.4	4.5842	0.4021
0.32	0.4	9.1684	0.8042

Table 4.3: Maximum rotor surge velocities for different combinations of amplitude and frequency

Table 4.3 shows clearly, how strong the inflow velocity fluctuation is for the high amplitude cases, with the rotor surge speed reaching more than 80% of the ambient mean wind speed.

By moving the rotor, work is done on the flow. Hence, an energy input is required to do this provide this work. From a simplified perspective, this power comes from the motion of the floating turbine, e.g. by wave motion. Further, this power is also equivalent to the aerodynamic damping of the FOWT floating motion by the rotor.

Table 4.4 depicts the power put into the flow by the prescribed motion of the rotor.

A/D	P_{Surge} (MW)	P_{Surge}/P (%)
0.02	0.03	0.23
0.04	0.11	0.90
0.08	0.45	3.48
0.16	1.77	12.62
0.32	6.4	36.77

Table 4.4: Power required for the surge motion, and comparison to the aerodynamic power for different motion amplitudes at a surge frequency of $St = 0.04$ and inflow turbulence level of $I_{in} = 2.5\%$.

Table 4.4 shows that for the high amplitudes, significant power is put into the system into the flow, reaching more than 12% of the aerodynamic power of the rotor at $A/D = 0.16$, and surpassing 35% at $A/D = 0.32$. These are both very high. A FOWT in motion will reach an equilibrium state, where energy put into the motion by the external forces and the dissipation are in balance. An energy input into the FOWT of multiple MW by wave motion can be considered high and it is very questionable, again, that this would occur in practice.

4.2.4 POD

In order to investigate the wake in more detail and highlight similarities and differences between the different flow cases, proper orthogonal decomposition is used. The energy content in different POD modes is used to indicate changes in the flow structures in the wake. Cross correlations are then used to show temporal similarities between the different flow cases.

DESCRIPTION OF THE POD DATABASE

A global POD is created, in order to represent all flow cases in a unified basis. Data from multiple cases is being used, comprising different motion amplitude and turbulent inflow combinations. An overview of all the flow cases used is shown in Table 4.5.

Data was obtained from planes normal to the mean flow direction at $x \in [2D, 10D]$ with a spacing of $1D$. The planes have a size of $2D * 2D$ centered around the rotor, with a sample resolution according to the grid resolution, resulting in 65×65 data points per plane. Data was sampled spaced 2^9 timesteps (30.72s), in accordance with the studies on the spacing of the samples in section 3.12. The transient has been removed from the datasets.

Case	Inflow TI (%)	St (-)	A/D (-)	Comment
1	2.5	0	0	
2	5.0	0	0	
3	2.5	0.4	0.02	
4	5.0	0.4	0.02	
5	2.5	0.4	0.04	
6	5.0	0.4	0.04	
7	2.5	0.4	0.08	
8	5.0	0.4	0.08	
9	2.5	0.4	0.16	
10	5.0	0.4	0.16	
11	2.5	0.4	0.32	
12	5.0	0.4	0.32	
13	2.5	0.2	0.04	
14	2.5	0.6	0.04	
15	2.5	0.8	0.04	
16	2.5	-	-	no turbine

Table 4.5: Flow cases used for the generation of the global POD basis

Using the described dataset, the POD has been computed. The stream-wise component of the first 25 spatial modes (left eigenvectors of the SVD) is depicted in Figure 4.9. The horizontal and vertical components of the spacial modes can be found in the appendix (Figure 6.4, Figure 6.5).

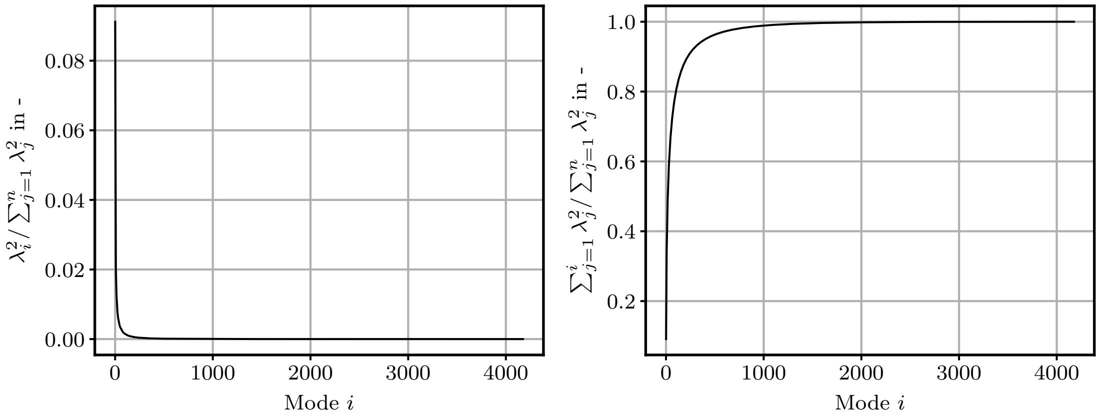

Figure 4.8: Relative squared eigenvalues of the POD basis (left), and its' cumulative representation (right)

Overall, the POD modes depicted in Figure 4.9 show a reduction in the size of the structures with increasing mode number. Some of the POD modes also show distinct structures that are commonly found in wind turbine wake POD analysis: Dipoles can be found in mode 1 and 2. They are rotated to each other and form a pair. Similarly modes 4 and 6 show quadrupoles with

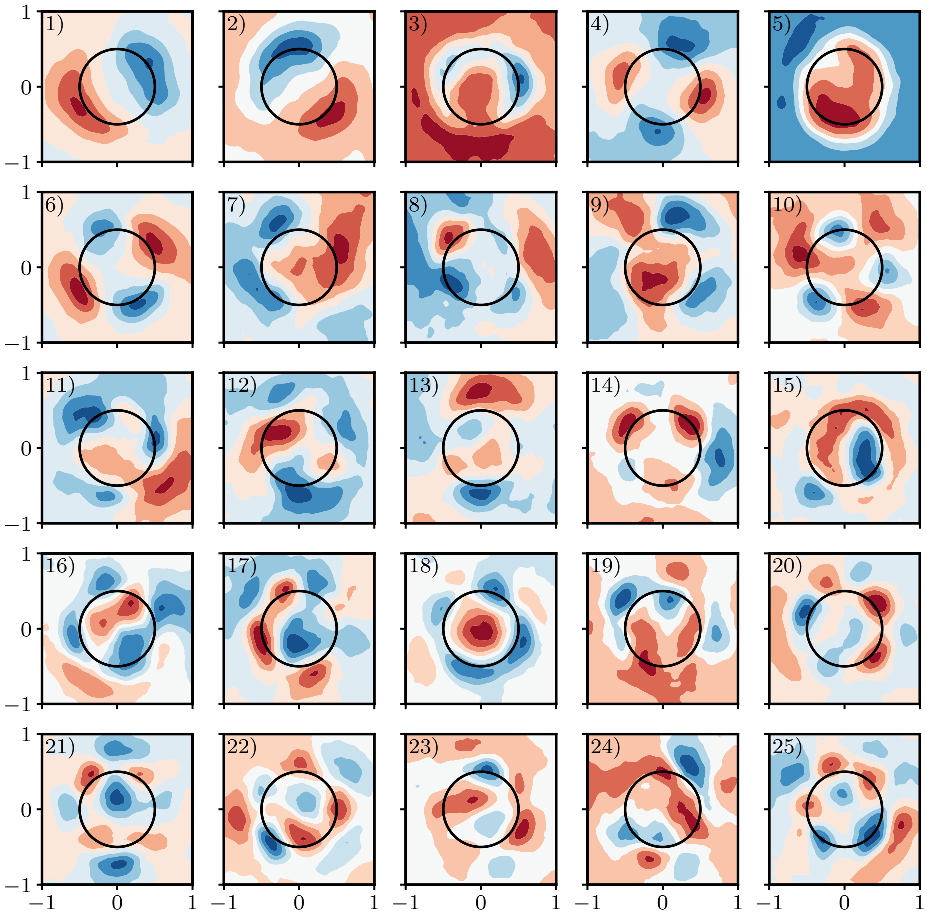

Figure 4.9: Stream-wise component u_x of the global POD basis. Only the first 25 modes are depicted.

a distinct rotation. Mode 5 represents a monopole. These findings are in line with e.g. Andersen, Sørensen, et al., 2013, Sorensen et al., 2015. Other modes appear rather unstructured. In general, the spatial modes in the current work are less smooth than the ones found in the references. This is likely connected to the limited amount of data used to generate the modes.

The square of the Eigenvalue represents the energy content in a mode for the whole dataset and the sum of the squared Eigenvalues can be used as a representation of the energy content in the POD modes. These are both depicted in Figure 4.8. It is shown that the energy content in the modes decreases rapidly, and most of the energy is already contained in the first 1000 modes.

ANALYSIS ON THE VALIDITY OF MODES

When computing the POD, the first modes will be connected to large-scale structures and decrease successively. Due to write precision and overall uncertainty in the data, the last modes cannot be assigned to physical structures in the flow and can be considered noise. In that case, modes are not relevant to represent the overall dynamic behavior of the wake.

The number of modes that are associated with the dynamics is dependent on the data input. If the amount of snapshots included in the POD is low, the number of modes that can be separated from noise reduces.

In order to investigate which modes are relevant for the dynamic representation and indicate invalid modes, several criteria have been formulated. Generally, they often define a threshold τ_M, such that only modes with eigenvalues surpassing the threshold can be separated from noise and should be considered.

Two criteria have been applied in order to estimate, how many of the modes are valid or interpretable. Criteria from Gavish and Donoho, 2014 and Epps and Techet, 2010 have been utilized. They both consider the shape of the data matrix and data noise/errors to generate a threshold τ_M. In Figure 4.10 the eigenvalues of the SVD are plotted and the two thresholds are added. It is shown that the eigenvalues are beyond the threshold for approximately up to mode 1300 (Gavish & Donoho) and 2000 (Epps & Techet).

This shows that for the given POD analysis, the number of included time steps is sufficient to generate a large enough amount of modes unrelated to noise. Hence, by concentrating only on the first (25) modes, no issues related to the data noise should be expected. However, it also shows that modes are neglected that contribute significantly to the dynamics of the flow.

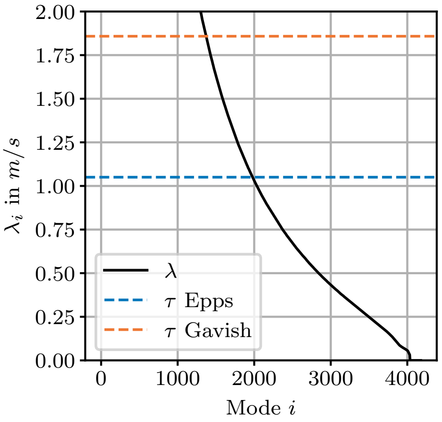

Figure 4.10: Estimates of the validity of POD modes based on two different threshold criteria for the Eigenvalues of the SVD. Modes with eigenvalues below the threshold are considered invalid.

MODAL TIME SERIES

As the POD basis has been established, it will now be used to do a deeper analysis of the flow characteristics. This is done by computing the modal time series, which contains temporal information on the energy contribution of the individual modes. By computing the variance of the modal time series, the energy content of the modes can be estimated and provides insights into how certain modes are related to the flow conditions.

The modal time series has been computed for all planes in all cases, by projecting the flow onto the POD basis as previously described in section 2.5. From these, the variance has been computed and is normalized by the sum of the squared sum of their corresponding eigenvalues. This is done in order to represent a ratio of the energy content of the modes. The results of these computations are visualized and split into two figures in Figure 4.11 and Figure 4.12. The subfigures in the left column represent cases at inflow turbulence of $I_{in} = 2.5\%$, and the right column $I_{in} = 5\%$. Along the rows of the figures, the motion amplitude increases.

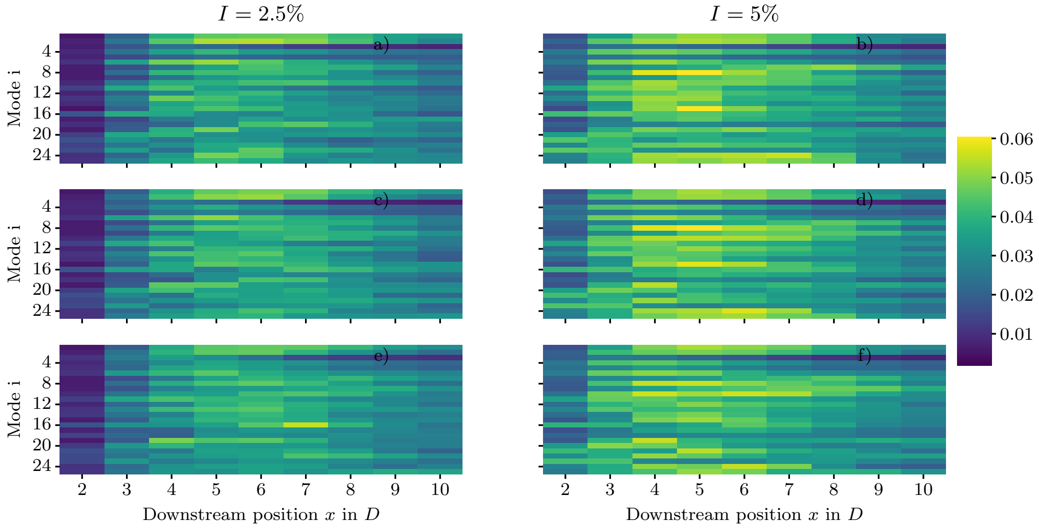

Figure 4.11: Normalized variances of the modal time series for varying plane positions and modes for the following cases: a) fixed, $I_{in} = 2.5\%$; b) fixed, $I_{in} = 5\%$; c) $A/D = 0.02$ $St = 0.4$, $I_{in} = 2.5\%$; d) $A/D = 0.02$ $St = 0.4$, $I_{in} = 5\%$; e) $A/D = 0.04$ $St = 0.4$, $I_{in} = 2.5\%$; f) $A/D = 0.04$ $St = 0.4$, $I_{in} = 5\%$.

At high amplitudes ($A/D \in [0.08, 0.32]$, in g, i, and k), distinct modes accumulate large amounts of energy. Starting from an amplitude of $A/D = 0.08$ (g) modes 3 and 5 have a high energy content at a downstream distance from the rotor of $3D$ to $6D$. When the amplitude is further increased, these modes have high energy for a wider range of downstream positions (2D to 8D for $A/D = 0.16$ in i); 2D to 10D for $A/D = 0.32$ in k)). At the low amplitudes from fixed over $A/D = 0.02$ to $A/D = 0.04$, no clear changes in the energy content of the modal time series can be found. For the higher turbulence cases, the same modes (3, 5) are active when the amplitudes are large ($A/D = 0.16$ in j); $A/D = 0.32$ in l)). However, it is clear that in higher inflow turbulence levels, higher amplitudes are necessary to find these modes being pronounced, and they don't sustain for similar long downstream distances.

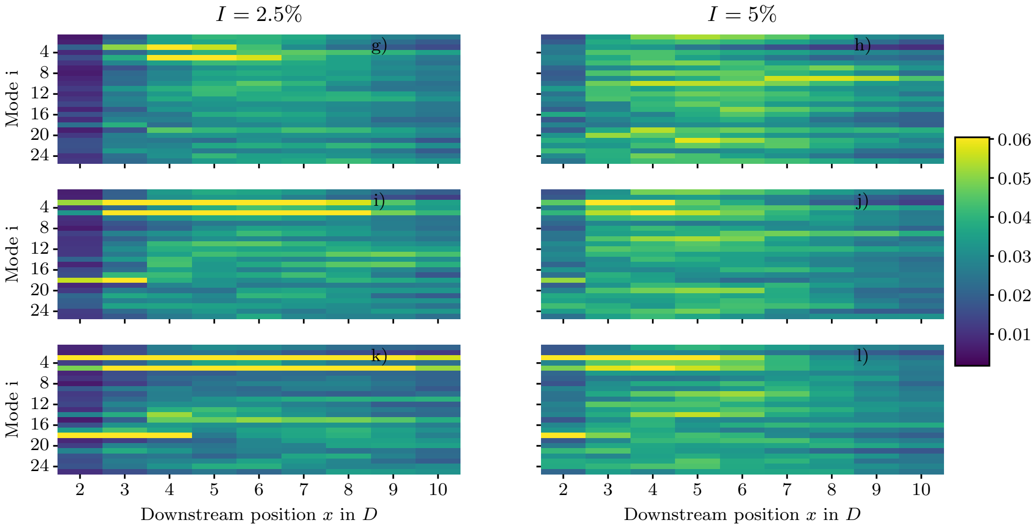

Figure 4.12: Normalized variances of the modal time series for varying plane positions and modes for the following cases: g) $A/D = 0.08$ $St = 0.4$, $I_{in} = 2.5\%$; h) $A/D = 0.08$ $St = 0.4$, $I_{in} = 5\%$; i) $A/D = 0.16$ $St = 0.4$, $I_{in} = 2.5\%$; j) $A/D = 0.16$ $St = 0.4$, $I_{in} = 5\%$; k) $A/D = 0.32$ $St = 0.4$, $I_{in} = 2.5\%$; l) $A/D = 0.32$ $St = 0.4$, $I_{in} = 5\%$.

The findings can be interpreted as that certain modes can be identified that are associated with the wakes of high amplitude motions. These are related to the flow structures developing in the wake. It hints towards, that distinct flow features are developing when high amplitude motion is present. However, when the inflow TI is increased, they are less pronounced. This might show that energy is not sufficient to build up these coherent flow features. Additionally, they break up earlier due to the effects of the ambient turbulence.

However, this analysis is not a proof of these coherent structures and need to be interpreted with care.

4.2.5 Correlations Between Different Flow Cases

When the turbine undergoes surging motion, flow structures/features building around the blades and in the wake are being modulated. If this modulation is small, then the features will be very similar, and, hence, the correlation of the flows will be high. Hence, the correlation along different flow cases with different motion parameters gauges, how large the effect of the motion on the flow features is.

Previously, the variance of the modal time series has been used as an indicator for the development of flow features in the wake. To further investigate these features and their relation to surge motion and inflow TI, correlations between the modal time series are analyzed in this section.

From a second perspective, if different TI levels are being used and correlations are high, then there can be two possible causes in the current setup. Firstly the correlation of the inflow can be high. This is due to the different turbulence levels being the same Mann box instance scaled to different TI levels. On the other hand, if these inflows are different, then the features leading to correlation are mainly caused by the rotor and are less dependent on the inflow TI levels.

With this motivation, correlations of the modal time series for different planes and different cases are being compared. First, the correlations of the modal time series of the same planes in different flow cases are investigated.

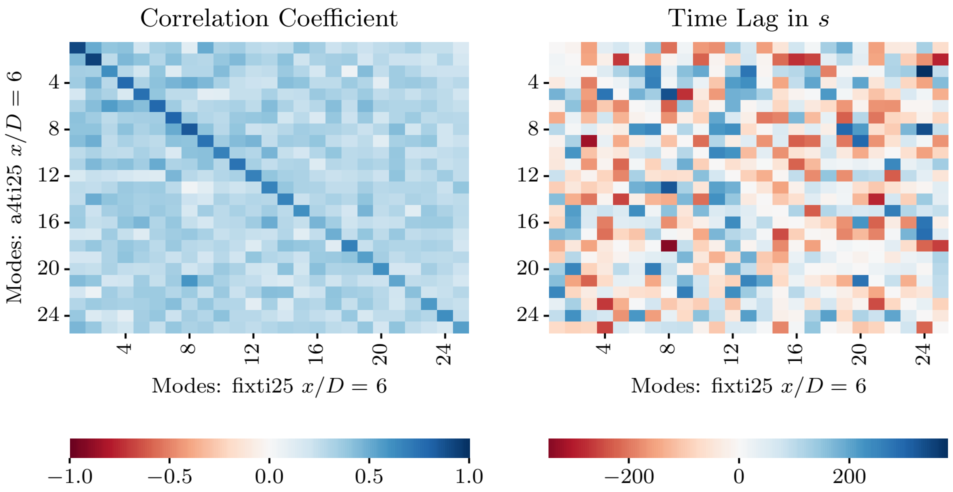

Figure 4.13: Cross-correlation of the modal time series and time lag for the flow cases fixed ($A/D = 0$), $I_{in} = 2.5\%$ and $A/D = 0.04$, $I_{in} = 2.5\%$. Both are at the plane at 6D downstream of the rotor.

Figure 4.13 shows the maximum cross-correlation and the according time lag of the signals for the two flow cases fixed ($A/D = 0$), $I_{in} = 2.5\%$ and $AD = 0.04$, $I_{in} = 2.5\%$. The main diagonal depicts the correlation of the modal time series of each mode of one flow case with the same mode in the second flow case.

It is shown that for the lower order mode, correlation is high, but for higher order modes, correlation tends to lower values. The off-diagonal elements show the correlation of a mode of the first flow case and a different mode of the second flow case. The correlations of the modal time series between non-equal modes (found on the off-diagonal) are generally low and no overall trends can be found. Hence, the relevant information is in the main diagonal. To compress the results and allow for a larger-scale comparison of correlations of the modal time series along different planes and cases, the main diagonals have been extracted for multiple flow cases and planes.

Firstly, the different flow cases will be compared with each other. By computing the cross-correlation between the identical modes (main diagonals) and planes of two different flow cases, a heat map can be generated, as shown in Figure 4.14.

In addition to the cross-correlation, Figure 4.13 shows the time lag. That is the time shift between the signals required to obtain the maximum correlation coefficient. It can be used as an indicator to estimate the advection speed when correlations between different planes in the same case are computed. Additionally, it provides an idea about the validity of the correlation: when the time lags are not in a reasonable range, it indicates that a possible high correlation is not due to actual overlap of structures, but rather a result of computing correlations from too short time signals.

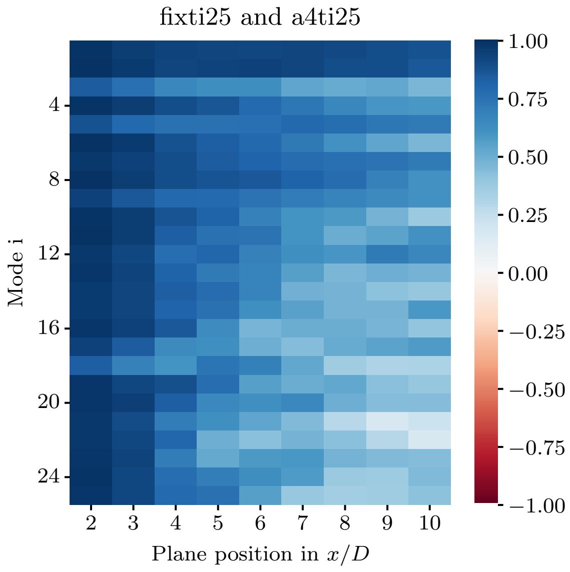

Figure 4.14: Correlation of planes and modes corresponding for fixed ($A/D = 0$), $I_{in} = 2.5\%$ and $A/D = 0.04$ at $I_{in} = 2.5\%$. The plot is generated by creating multiple plots comparable to Figure 4.13 for identical plane positions and extracting the main diagonal.

Figure 4.14 reveals, that generally, with increasing downstream distance the correlation reduces between the two different flow cases. Additionally, lower order modes tend to correlate for larger downstream distances.
A figure like that is generated for multiple combinations of flow cases, which can be found in Figure 4.14. These computations have been done to compare:

1. The fixed case with the cases with varying amplitude at TI of $I_{in} = 2.5\%$
2. The fixed case with the cases with varying amplitude at TI of $I_{in} = 5\%$

The entirety of these results can be found in the appendix in subsection 6.5.2.

THRESHOLD

In order to extract the essence of these heat maps, a measure is introduced to gauge the similarity of the flow cases in the following way: A threshold $\tau_c = 0.5$ is set. For every figure, the count of fields surpassing this threshold $\rho > \tau_c$ are counted in each column. In essence, the measure shows the ratio of modes (only considering the first 25), that surpass the threshold.

The ratio of modes surpassing the correlation threshold τ_c to the number of modes is computed as follows:

$$n_{\rho > \tau_c} / n_{modes} \tag{4.4}$$

This measure has a qualitative character, although it has a numeric value assigned to it. From a conceptual perspective, it is a combined measure for a reduced order flow field, hence, a filtered flow field. However, the filtering is not related to scales, but to modes, i.e. energy content.

The threshold τ_c allows to compare the overall behavior of the progression of correlation while filtering out the correlations that are likely related to noise. Due to the short sample lengths of the time series, correlations due to random processes in the signal can become high and would be lower for longer sample lengths.
Figure 4.15 shows the integrated correlation measure to compare the flow cases with varying amplitude to the fixed turbine flow case at an inflow turbulence intensity of $I_{in} = 2.5\%$. In general, the further downstream the sampled plane is from the rotor, the stronger the correlation decreases. With increasing surge amplitude, the reduction of the cross-correlation occurs further upstream and is in general stronger.

Upstream disturbances grow over the course of being advected. They get amplified, such that the flow structures develop in a different way. The higher the disturbance, the more the correlation will reduce when going downstream.

Figure 4.16 shows the same correlation measure comparing the flow cases with varying amplitude to the fixed turbine flow case at an inflow TI of $I_{in} = 5\%$. The trends found at inflow turbulence level of $I_{in} = 2.5\%$ are the same for the higher turbulence intensity of $I_{in} = 5\%$: The correlation near the rotor is high and then reduces in the downstream direction. With an increase in the surge amplitudes, the correlation to the reference case with a fixed turbine is reduced. Overall,

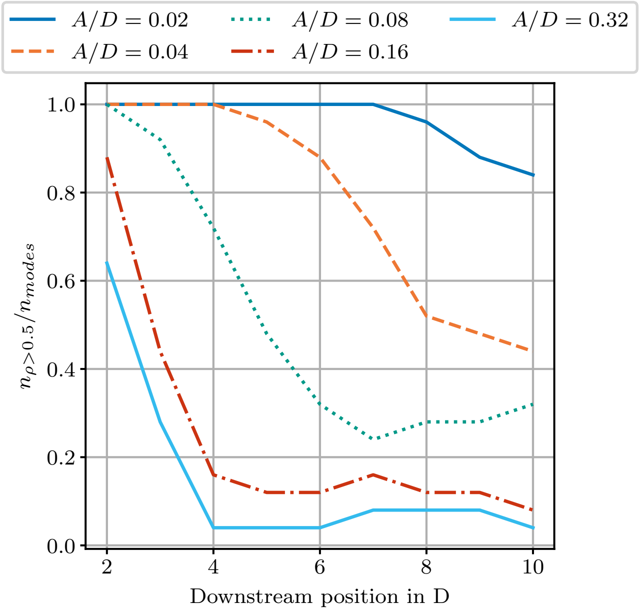

Figure 4.15: Comparison of the progression of correlation between the moving turbine flow cases ($St = 0.4$, varying amplitude) and the fixed turbine flow case, both at an inflow turbulence level of $I_{in} = 2.5\%$. The threshold criterion is used to find the ratio of the number of modes with high correlation $\rho > \tau_c$

comparing the same amplitudes of Figure 4.15 and Figure 4.16, it is apparent that for the higher inflow TI, the correlation between the fixed turbine flow-case and the moving flow-cases is higher. For the lowest amplitude, Figure 4.16 even suggests, that the cases are fully correlated for the higher inflow TI. However Figure 6.25a reveals, that the correlation still reduces downstream, only at a smaller rate and, hence, stays above the threshold all the way.

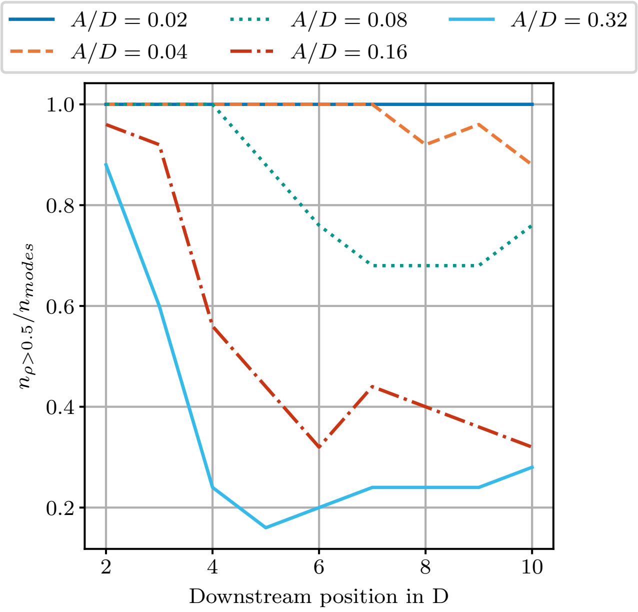

.

Figure 4.16: Comparison of the progression of correlation between the moving flow cases and the fixed turbine ($A/D = 0$) flow case, both at an inflow turbulence level of $I_{in} = 2.5\%$. The threshold criterion is used to find the ratio of the number of planes with high correlation $\rho > \tau_c$

4.2.6 CORRELATIONS OF DIFFERENT PLANES

In the previous section, the correlations of the same modes at the same positions for different flow cases have been compared, in order to show the differences in the development of the modal time series over different flow cases. However, further information on the development of the wake within a single flow case can be obtained using correlations. When computing the cross-correlations between the modal time series of different planes within one flow case, the progression of the correlation of single modes in the downstream direction can be extracted. Additionally, due to the stream-wise offset of the planes, a time lag of the modal time series is introduced. This time-lag yields additional information about the validity of the correlations. If the time lag is discontinuous, this hints towards uncorrelated flows. In that case, high correlations would be, as discussed, a result of the relatively short time sequences used in this study. The time lag is normalized by the modal advection time scale, computed as the time lag normalized by the plane distances. The time lag is computed as an average of fields of the heat map (modes and planes) yielding a correlation of $\rho > 0.75$.

The computation of cross correlation and time lag is done for the case $A/D = 0.04$ at $I_{in} = 2.5\%$, where correlations of the modal time series at the last plane (10D downstream) and the modal time series of the upstream planes are being calculated. Results are shown in Figure 4.17.

The computation is repeated for every flow case, and the full results can be found in the appendix subsection 6.5.1.

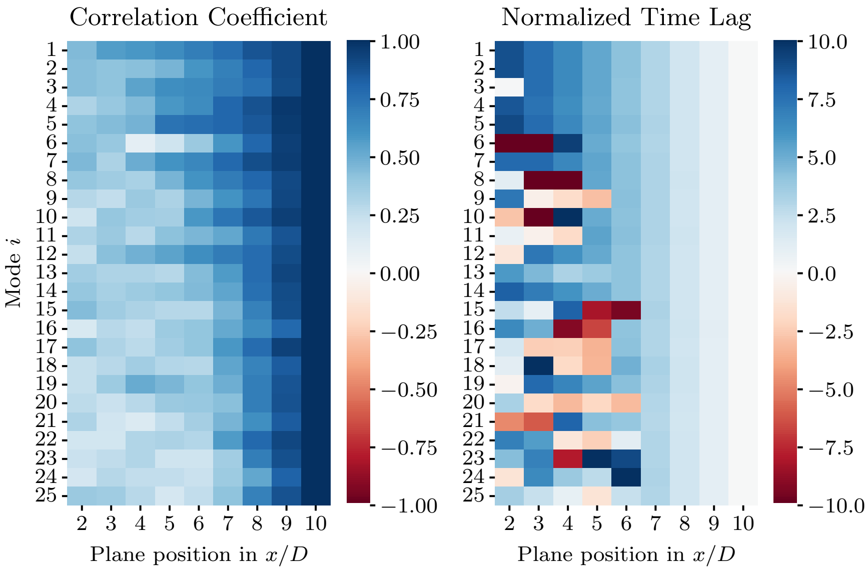

Figure 4.17: Correlation of the modal time series between the equal modes at the plane at $x = 10D$ and the upstream planes for the flow case $A/D = 0.04$ at $I_{in} = 2.5\%$. The plot is generated by creating multiple plots comparable to Figure 4.13 for different combinations of cross-correlations between modal time series of planes in the same flow case and extracting the main diagonal.

Figure 4.17 shows the overall trend that the larger the distance between the upstream and the downstream plane ($x = 10D$) is, the lower the correlation gets. In the close range to the plane, (9D), all modes still show high correlation. Mode 1 and 2 have continuous time lags over all distances, indicating that these modes stay correlated over the full observed range. For higher modes, correlation is generally lost more quickly. This is further shown by the time lag being discontinuous, showing that the correlation is lost. When then after the discontinuity of the time lag a high correlation is found, this is considered as a result of noise.

As in the previous section, results have been further compressed using the same approach of defining the threshold $\tau_c = 0.5$ and computing the ratio of modes surpassing this threshold for the correlations between the plane at $x = 10D$ and the upstream planes ($x \in [2D, 9D]$). This is depicted in Figure 4.18 for the amplitude variation at $I_{in} = 2.5\%$ and Figure 4.19 for the amplitude variation at $I_{in} = 5\%$.

These two figures have to be read from right to left, as the cross-correlation between the modal time series of the last plane (x=10D) and all other upstream planes is computed. As a direct result, the correlation at 10D with itself is always 1. Then, going further upstream, correlation reduces.

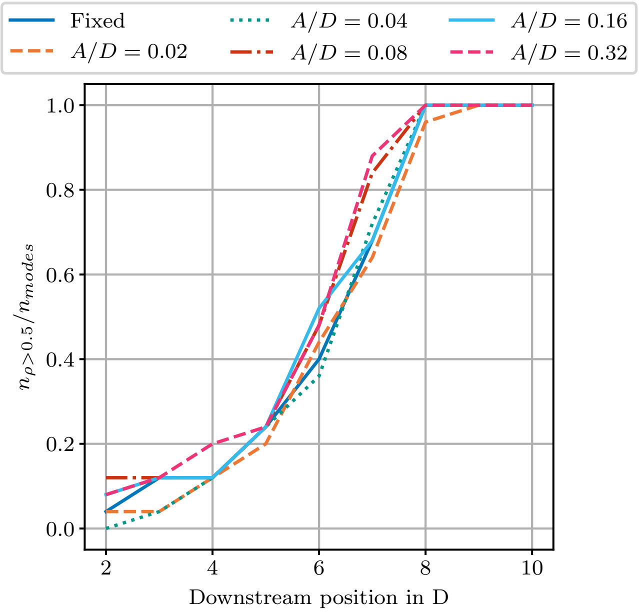

Figure 4.18: Comparison of the progression of correlation between the plane at $x = 10D$ and the upstream planes, for different motion amplitudes at a turbulence level of $I_{in} = 2.5\%$ and a motion frequency of $St = 0.4$. The threshold criterion is used to find the ratio of the number of planes with high correlation $\rho > \tau_c$.

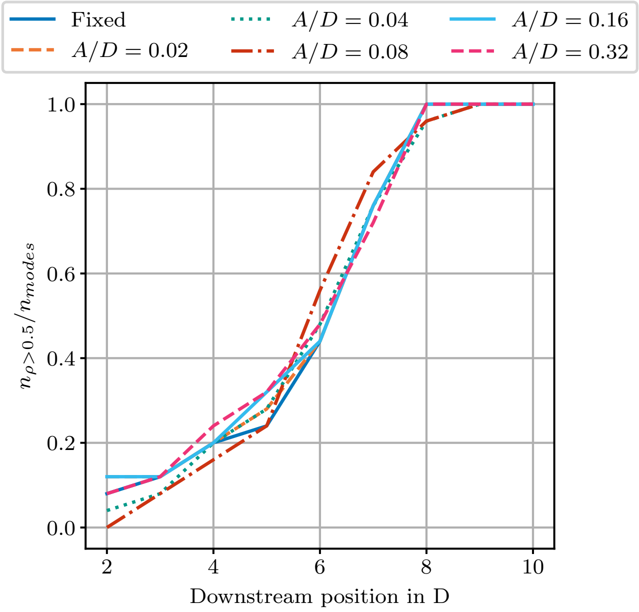

Figure 4.19: Comparison of the progression of correlation between the plane at $x = 10D$ and the upstream planes, for different motion amplitudes and a motion frequency of $St = 0.4$ at a turbulence level of $I_{in} = 5\%$. The threshold criterion is used to find the ratio of the number of planes with high correlation $\rho > \tau_c$.

Most striking is, that for all amplitudes and both turbulence levels, the correlation curves collapse. They are not fully identical, but likely in the range of the uncertainty introduced by the utilized analysis methods. This suggests, that from the perspective of the far wake, the turbulent structures break up in a similar way for all cases.

4.2.7 SECTION SUMMARY

In this section, the influence of different surge amplitudes on the wake has been investigated. Computing the rotor-averaged velocity in the wake for different downstream positions in subsection 4.2.1, it has been shown that differences between the wakes with different motion amplitudes are significant in laminar inflow conditions, but are way less noticeable when even low turbulence of 2.5% is introduced at the inflow. In that case, only the very high motion amplitudes of $A/D = 0.16$ and $A/D = 0.32$ were able to significantly alter the wake statistics.

The loads on the blades, thrust, power progressions, and power input into the flow by the surge motion have been computed. They have shown that the large amplitude cases are very extreme, leading to load conditions that would not be found in the operational envelope of a real FOWT. Even for the small motions, the increase in the standard deviations of the loads was found to be significant.

Lastly, POD has been used in order to investigate the development of the flow structures in the wake. Computing the energy in the modes by evaluating the variance in the modal time series, certain modes could be found that were associated with high motion amplitudes. However, the energy content in these modes was found to reduce significantly when the inflow TI was increased from $I_{in} = 2.5\%$ to $I_{in} = 5\%$.
Computing the correlation of the modal time series, it was shown that the higher the surge amplitude, the faster the correlations to the modal time series of a fixed turbine reduce, pointing towards different flow structures evolving in the wake. At the larger inflow TI level of 5%, the correlations between cases with different surge amplitude were higher compared to the lower inflow TI. This shows that the motion amplitude loses importance, while the dependence of the wake flow on the inflow conditions increases. Further, correlations of different planes within individual flow cases showed, that for all flow cases, the correlation of the modal time series over the downstream direction are similar when seen from the far wake, pointing towards a more universal character of the wake in this region.

4.3 VARIATION OF THE SURGE FREQUENCY

In this section, the differences of the wake characteristics for varying surge motion frequencies are being investigated. The analysis follows the thread of the previous section.

The current frequency range was chosen as $St \in [0.2, 0.8]$ based on the findings of Messmer et al., 2024. They showed that in the range $St \in [0.5, 0.9]$ a quasi periodic wake is found. Here the surge motion induces a meandering. For lower $St \in [0.2, 0.5]$, pulsing of the wake with synchronization to the excitation frequency is present. Hence, varying the Strouhal number in that range might reveal different wake patterns, that could have different effects on the wake even in turbulent inflow conditions.
As before, the rotor- and time-averaged velocity deficit and wake turbulence intensity have been computed and are depicted in Figure 4.20.

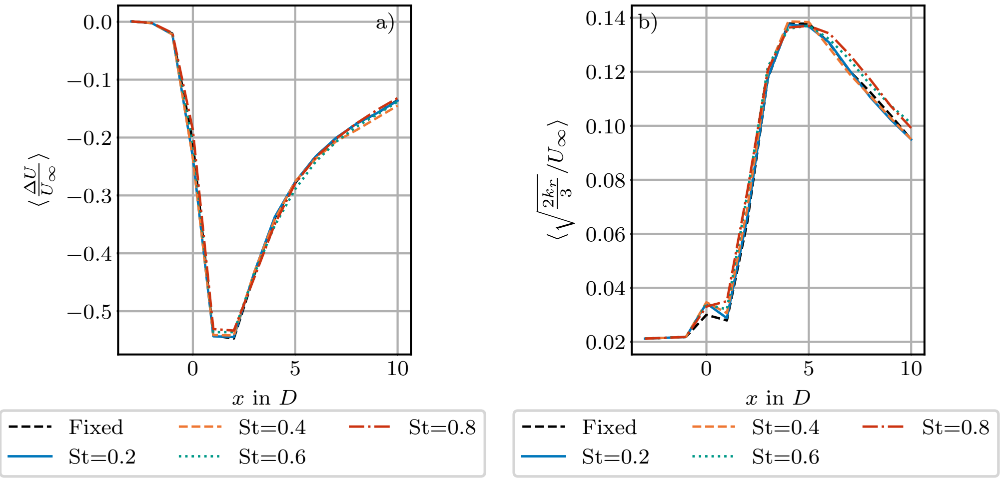

(a) Rotor- and time-averaged velocity deficit $\frac{\Delta U}{U_\infty}$ as a function of the downstream distance for different motion frequencies and inflow turbulence intensities.

(b) Rotor- and time-averaged wake turbulence intensity $\langle \sqrt{\frac{2k}{3}} \rangle / U_\infty$ as a function of the downstream distance for different motion frequencies and inflow turbulence intensities.

Figure 4.20: Wake statistics for varying surge motion frequencies

Figure 4.20a depicts the wake deficit for 5 different motion conditions. It is shown that for the low inflow TI level of $I_{in} = 2.5\%$, all frequencies collapse and no differences can be found. Figure 4.20b supports these findings by showing, again, that for all motion frequencies the results for the TI in the wake collapse to the results found for the fixed wind turbine.

4.3.1 POD

As in the previous section, POD was utilized in order to obtain a more detailed view of the wake characteristics. The flow cases with varying surge frequency have been included in the data set used to create the POD basis in the previous section. The same POD basis is therefore used again, allowing for direct comparisons to the previous results.

The variances of the modal time series have been computed for all motion cases and planar positions (2D to 10D downstream). The results are depicted in Figure 4.21 a), b), and c).

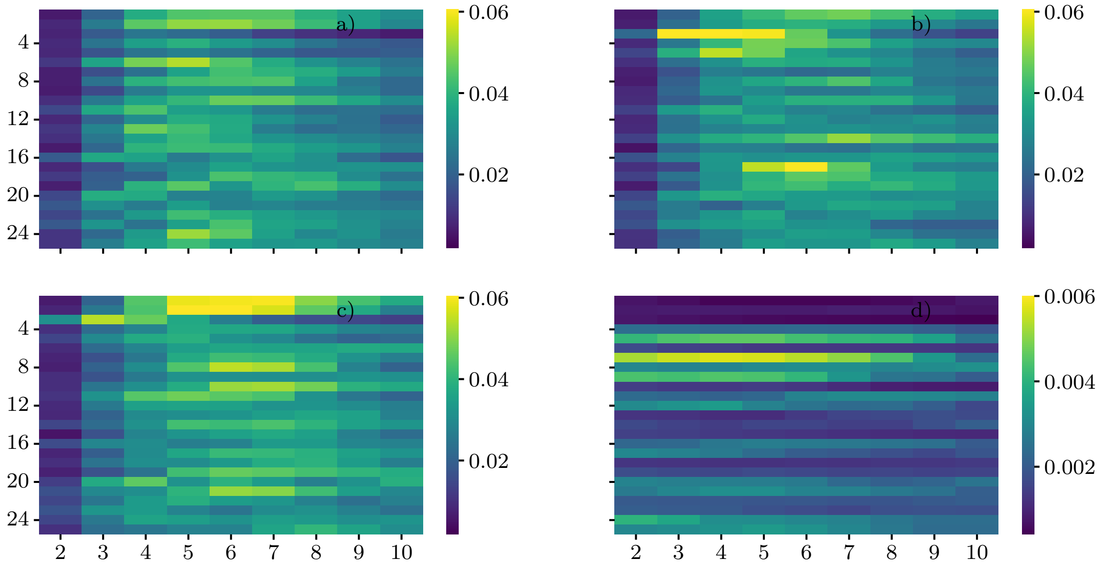

Figure 4.21: Normalized standard deviations of the modal time series for varying plane positions and modes for the following cases: a) $A/D = 0.04$ $St = 0.2$, $I_{in} = 2.5\%$ b) $A/D = 0.04$ $St = 0.6$, $I_{in} = 2.5\%$ c) $A/D = 0.04$ $St = 0.8$, $I_{in} = 2.5\%$ d) empty channel, $I_{in} = 2.5\%$.

The variance of the modal time series at $St = 0.2$ in Figure 4.21 a) shows no clear difference to the baseline case at $St = 0.4$ (Figure 4.11 e)). When the motion frequency is increased, similarly to the amplitude variation, certain modes contain larger energy. At a motion frequency of $St = 0.06$ in b), modes 3 and 5, which have previously been associated with wakes at high amplitude surge motion, show an increase in variance at a downstream distance of around 4D from the rotor. At $St = 0.8$ in c), there is an increase in the variance of modes 1 and 2 at 5D to 7D distance from the rotor.

All together, no clear tendency for the change in the frequency on the modal variances can be found. Based on the current findings, it is not possible to associate certain spatial modes with the increase in motion frequencies.

4.3.2 THRESHOLD

In the same manner as in the previous section, the threshold τ_c condition is used to compress the results of the correlation computations.
Figure 4.22 depicts the comparison of the fixed flow case to 4 different flow cases with an amplitude of $A/D = 0.04$ and varying motion Strouhal numbers. This is done by computing the cross-correlation between the modal time series of the same planes and modes of both cases and counting the number of highly correlated modal time series ($\rho > 0.5$) as before.

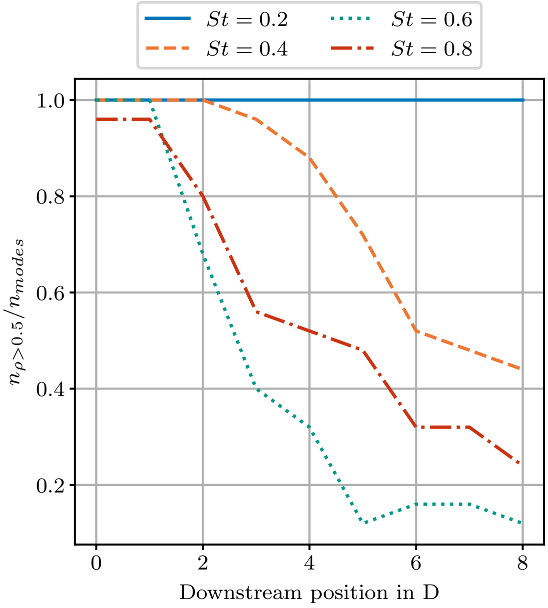

Figure 4.22: Comparison of the progression of correlation between the moving turbine flow cases and a fixed turbine flow case, both at an inflow turbulence level of $I_{in} = 2.5\%$. The threshold criterion is used to find the ratio of the number of planes with high correlation $\rho > \tau_c$.

The correlation is high for the lowest frequency case and reduces up to the Strouhal number of $St = 0.6$. However, when further increasing the Strouhal number to $St = 0.8$, the correlation increases again. The correlation of the lowest frequency case and the fixed case is very high, which can be visually inspected in Figure 6.27b. A possible explanation might be in Table 4.3. Due to the low frequency, the surge velocity is also smaller than for higher motion frequencies. Hence, less energy is pumped into the flow, which indicates less disturbance.

The largest loss of correlation for a frequency of $St = 0.6$ shows, that this frequency is able to disturb the flow structures more than a higher frequency would, even though the surge velocity (and therefore energy) is lower. For this case, it has previously been found that the same modes were activated as in high-amplitude motion wakes. It is generally intricate to assign certain modes with the specific physical behavior of the flow, as a POD basis does not isolate flow structures. However, the activation of the same modes is an interesting occurrence and might hint towards

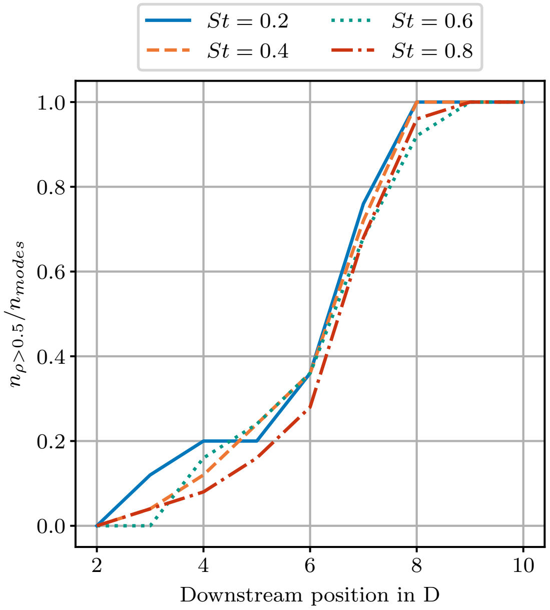

Figure 4.23: Comparison of the progression of correlation modal time series between the plane at $x = 10D$ and the upstream planes at an inflow turbulence level of $I_{in} = 2.5\%$ for a variation of the motion frequency. The threshold criterion is used to find the ratio of the number of planes with high correlation $\rho > \tau_c$.

certain similarities between higher amplitude cases and the high-frequency case. Further research would be necessary to gain proper insights into why these modes appear in both conditions (high amplitude and $St = 0.6$).

The threshold criterion is again applied to the correlations of the modal time series of the planes within a single case to show how the flow develops when advecting through the domain, which is depicted in Figure 4.23.

As seen before for the amplitude variation, all curves for the different motion frequencies collapse, hinting towards a universal wake development behavior in the far wake.

SECTION SUMMARY

First, the wake statistics were evaluated, considering the time- and rotor-averaged velocity deficit and turbulence intensity. All motion frequencies collapsed onto the results obtained for a fixed turbine, and, hence, no differences due to the motion frequency could be found.

The variances of the modal time series were computed in order to represent energy content in different modes. While at the frequency of $St = 0.6$ the same modes were found to be more active that were found to be important in the wakes of high amplitude motion cases, no general trend could be found between motion frequencies and active modes.

Evaluating the correlations of the varying motion frequency cases with the fixed turbine wake, it was shown that the motion frequency of $St = 0.6$ lead to larger de-correlation of the wake flow.

4.4 INVESTIGATION ON THE BACKGROUND FLOW

The sampled cross-stream planes have a size of $2D \times 2D$. This was chosen as this was within the uniform grid region as well as allowing to capture the dynamics in the wake, where meandering and expansion lead to large spacial structures reaching outwards of the rotor area.

However, the POD captures energy in the whole dataset. Close to the rotor that means, that a lot of the "outside" region is in the data. This outside region might be relevant for the POD: The turbulent inflow used is a single realization of a turbulence box, scaled to the different levels of turbulence intensity. However, the spatial structures are the same for each simulation. This means that each simulation contributes with fluctuations from the turbulence, that are the same. It is unclear at this point, how this might affect the POD analysis.

Therefore, an empty channel flow only with the turbulent input is projected onto the POD basis, trying to reveal if there might be any dependencies. This approach is not technically rigorous: it neglects the interaction of turbulent structures and the wind turbine and therefore assumes sort of linear superposition, which is not actually physical.
Figure 4.24 shows the correlation of planes between the empty channel flow and a flow case with a fixed turbine, both at TI2.5. It is clear, that no correlative behavior can be found at any plane or mode.

The modes are optimal in the sense of capturing energy in the fluctuation. Most fluctuation stems from the energy extraction by the rotor, not by the ambient turbulence. Hence the main features of fluctuation are not present and the empty channel flow is uncorrelated to the cases with a turbine present.

Lastly, the correlations between the modal time series for the different planes within the empty channel flow case have been computed. These are depicted in Figure 4.25. Overall, correlations stay quite high when compared to the cases where the turbine is present. To some extent, this shows the validity of Taylor's frozen turbulence hypothesis: As the correlations are high, it is a first-order approximation that the turbulence is advected without larger changes. For mode 9 the time lag is inconsistent. This indicates that there still is a development of the flow structures and correlation reduces with the distance of the planes.

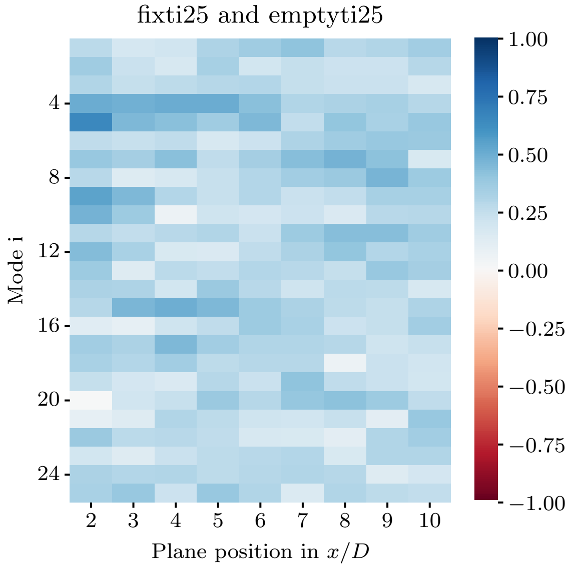

Figure 4.24: Correlation of the planar modal time series for an empty channel flow and a fixed turbine, both over the same turbulent inflow field realization

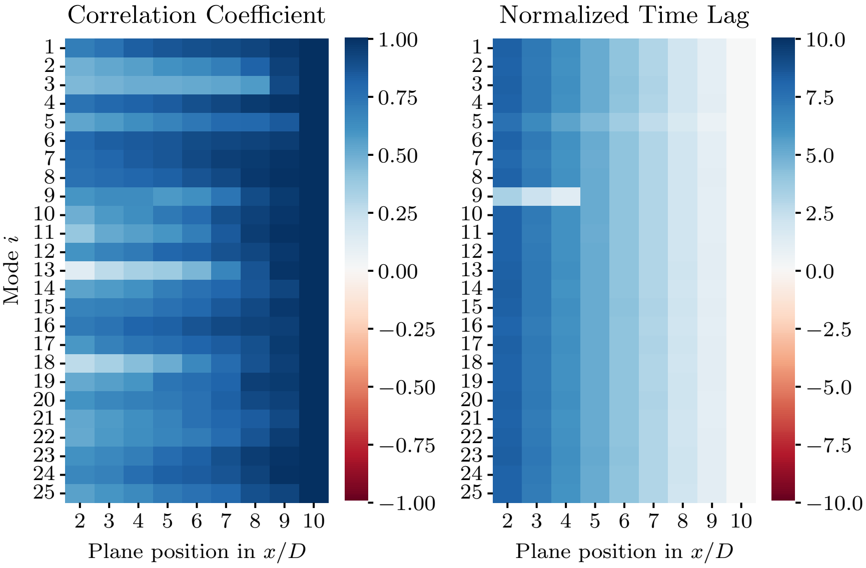

Figure 4.25: Correlation between the modal time series of the plane at $x/D = 10$ and the upstream planes for the empty flow case

5 CONCLUSION

This section concludes the findings in the current research, while specifically pointing out the limitations of the obtained results. The research questions are then answered and lastly, the overall findings are summarized.

5.1 DISCUSSION OF THE MAIN ISSUES WITHIN THE RESEARCH

The chosen combination of grid and ALM creates issues regarding grid-dependent results on one hand and overproduction of thrust and power on the other.
As shown and discussed in section 3.8, results are still dependent on the grid resolution. It is argued, that the grid dependence is largely caused by the ALM model being used without any correction and, hence, reaching the limits of its ability to represent the wind turbine physics well on a coarse grid.
In the context of this study, simulation time was prohibitive to run simulations on finer meshes, reducing the error added by the ALM. However, even on a finer grid, grid dependence was not significantly alleviated, as the GCI was found to be very high still.
The error was evaluated from the power and thrust produced by the turbine. This measure cannot isolate the errors by the ALM and the discretization errors in the context of the finite volume method. The latter is the target value of the grid independence study. Hence, the power and thrust values are not a good measure for convergence. However, due to the grid dependence of the ALM, also other flow variables will directly change as a result of changing thrust and power. This is why for improving the quality of the current study, a proper usage of correction methods would be of high value, in order to obtain appropriate results on a relatively coarse mesh.

The study was continued despite the known issues with the setup, referring to the findings in Hodgson, M. H. A. Madsen, et al., 2023, that a lower resolution may still be useful to resolve the shear layer and the general wake behavior. Additionally, it is argued that actuator discs are used in comparable studies like Messmer et al., 2024. In these studies, power is neglected and only thrust forces are present. Hence, the approach can produce relevant results although the power coefficient is not comparable to a realistic wind turbine. The focus is then to just capture the shear layer and the overall behavior of the wake well enough.
However, an evaluation of the discretization error would in any case still be necessary to build trust in the numerical results, which is considered a major issue in the current research.

The high power and thrust coefficients caused by the low grid resolution directly affect the wake flow, where extremely high inductions were found. In hindsight, the choice of an actuator disc model might have performed better in the affordable grid resolutions and should be considered, if the current research is iterated.

Due to the surge motion the inflow speed changes, leading to a variation in the angle of attack. This is especially significant for large surge amplitudes and high frequency motion. This means that data is sampled from the entire Angle of attack (AOA) range of the force coefficient polars. As argued before Bak et al., 2013 used 2D RANS to obtain the force coefficients for the operational ranges, but assumed a flat plate for high angles of attack. As a result, for the high surge amplitude and large AOA variations, flat-plate force coefficients are sampled. In the context of lower fidelity models and steady-state simulations, this is likely not an issue, as the interest is more in showing the overall performance of the blade for all conditions. However, for a highly transient flow case with large variations as in the current work, this may not properly represent the forces exerted by the wind turbine blade anymore. Hence, for high AOA variations, a more sophisticated baseline turbine with representative data for high AOA conditions would improve trust in the model.

Additionally, the airfoil data is only given for certain Reynolds numbers that are representative for the normal operation of the wind turbine. However, for the surging turbine the inflow velocity, and hence Reynolds number, changes. For the large surge motion case, inflow velocity can be almost doubled. In the outer region of the blade, considering the velocity triangle, the contribution of the inflow wind speed to the relative wind speed of the blade is small, and therefore the changes due to the motion are expected to be small. However, in the inside section the variation is more drastic, as the speed due to rotation is lower and, hence, the contribution of the inflow speed is larger in the velocity triangle. Further investigations would be required in order to investigate the influence of the Reynolds number at high motion amplitudes.

Considering the inflow modeling, only a single realization of a turbulent field has been used. Generally, it would be preferable to use multiple seeds to make sure that results are not dependent on the seed used to generate the wind field.

In a follow-up study, these issues would need to be addressed to improve on the current approach and increase the quality of the results.

5.2 ANSWERS TO THE RESEARCH QUESTIONS

Previously, the findings in the report have been portrayed and critically reviewed. The following shows, how far the results can be used to answer the research questions and test the research hypotheses:

1. *Surge motion has only minor effect on the wake when TI is present*

    - It has been shown by evaluating velocity deficit and wake TI, that at a low inflow turbulence level of $I_{in} = 2.5$, these wake statistics are similar for surge motion amplitudes of up to $A/D = 0.08$ at a motion Strouhal number of $St = 0.4$ and collapse to the results obtained for a fixed turbine. When varying the surge frequency between $St = 0.2$ and $St = 0.8$ at an amplitude of $A/D = 0.04$ and an inflow TI of $I_{in} = 2.5\%$, wake deficit and turbulence intensity do not significantly differ from those of a fixed turbine.

2. *With increasing TI, the effects of surge motion vanish*
   - From the wake deficit and wake turbulence intensity, no differences between $I_{in} = 2.5\%$ and $I_{in} = 5\%$ have been found. However, when using POD to compute correlations between the modal time series for the same modes at the same planes, stronger correlations between moving and fixed turbine wake have been found at the higher TI level. This suggests that the inflow turbulence becomes a more dominant factor in the wake development than the motion amplitude. This supports the hypothesis of the influence of the motion decreasing with increasing inflow TI.
3. *When surging the turbine with sufficient amplitude, an effect on the wake can be found*
   - For large wind turbine motions of amplitudes $A/D = 0.16$ and $A/D = 0.32$, wake deficit and wake turbulence intensity were changed in both turbulence levels. Using POD and computing correlations between modal time series, a change between the fixed and a moving case can be seen already at lower motion amplitudes than $A/D = 0.16$. For all motion amplitudes, the correlation of the wake to the wake of a fixed turbine is reduced, and with increasing amplitude, the correlation decreases. For both higher amplitudes, the models' capability to properly represent the flow physics is questionable, due to the high unsteadiness in the inflow and the high power coefficients. Additionally, it is argued these conditions are outside the operational envelope of a realistic FOWT.

5.3 SUMMARY

In this report, the wake behavior of a floating wind turbine undergoing surge motion in turbulent inflow conditions was investigated. Using the LES code YALES2 in combination with an actuator line model of a wind turbine, wake flows were generated.

In order to investigate the behavior of the numerical setup, investigations by Z. Li et al., 2022 for sway motion were reproduced. The model successfully captured the overall trends of the wake deficit and turbulence intensity.

Considering surge motion, comparing the wake deficit and wake turbulence intensity for different motion amplitudes in different turbulence conditions revealed, that already at a low turbulence level of $I_{in} = 2.5\%$ no significant difference was found for motion cases up to an amplitude of $A/D = 0.08$, which is considered high. Only when extreme motion amplitudes are present, the wake deficit and turbulence intensity differ significantly from the results obtained for a fixed turbine.

Using a global proper orthogonal decomposition, that is based on data at multiple cross-stream planes in different flow cases an ortho-normal basis is generated. For large amplitudes, certain modes can be identified that are associated with the wakes of wind turbines with large surge amplitudes across different large amplitude cases. These modes tend to be less relevant when the ambient turbulence level is increased, suggesting a reducing dependence of the flow on the motion amplitude with increasing turbulence levels.

When varying the motion frequency instead of the amplitude, it was shown that at $St = 0.6$, the loss of correlation between the fixed turbine flow case and the moving turbine case is the highest. This suggests this frequency is more effective at disturbing the flow. Additionally, it was found that in the wake at this motion frequency, some of the modes that previously have been associated with wakes of high amplitude motions contain high energy. However, the results are not sufficient to draw parallels.

Lastly, when considering the correlations between the different planes within the individual flow cases, the wakes in all motion conditions showed similar behavior in terms of the progression of the correlation coefficient. This suggests, that in the far wake, the influence of the specific motion conditions on the development of the wake is reduced.

The results need to be considered with caution, as simulations suffer from grid dependence and, hence, further studies are required to properly validate the results.

The study overall suggests that when turbulent inflow conditions are present, the effects of floating motion on the wake are strongly reduced.

6 Appendix

6.1 Unstructured Grid

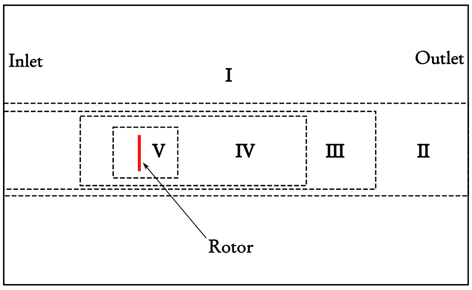

Figure 6.1: Layout of the tetrahedral mesh. The rotor center is positioned at (0,0,0), where x is the streamwise coordinate. The mesh is symmetric in the xy-plane and xz-plane.

Region	Cell size	Height	X_0	X_1
I	LC	6D	-3D	7D
II	LC/2	2D	-3D	7D
III	LC/5	1.7D	-3D	5D
IV	LC/7	1.5D	-1.5D	3.5D
V	LC/12	1.4D	-0.55D	0.55D

Table 6.1: Mesh parameters for tetrahedral mesh, with the rotor diameter D and the cell length LC. LC is approximately $^5/_{12}D$, as used in Combette, 2023.

The unstructured mesh used for the validation of the ALM model is based on the mesh used by Combette, 2023, but was adapted to the current setup. The mesh was scaled up to preserve the same ratio of cell sizes to rotor diameter, as a different wind turbine is used. The refinement boxes II and III have been extended towards the inlet, in order to resolve the turbulent structures from the inlet. The mesh consists of tetrahedral elements.

In the course of the grid independence study section 3.8, the resolutions of the different field regions were adapted in order to obtain different resolutions at the rotor, leading to varying numbers of actuator points as depicted in Table 3.6. The exact resolution of the cases is missing due to loss of data.

6.2 DISSIPATION OF SYNTHETIC TURBULENCE

As turbulence fields generated with the Mann method are not solutions of the Navier-Stokes equations, it is anticipated that an undesired numerical behavior appears close to the inlet. Specifically, it is investigated, how much turbulence dissipates due to the interaction with the mesh.

A preliminary study on the inflow was done in an empty domain to investigate the change in turbulence statistics over the domain without the influence of the wind turbine. This is intended to reveal the dependence on the grid and CFD solver. The domain and mesh used are described in section 3.2 and subsection 3.3.1. The inflow turbulence is generated using parameters from Table 6.2 and the tool *IEC Turbulence Simulator* 2024. The number of points in the turbulence box was changed to $1024 \times 256 \times 256$ to comply with the needs of the tool. The turbulence intensity is then scaled to $I = 5\%$.

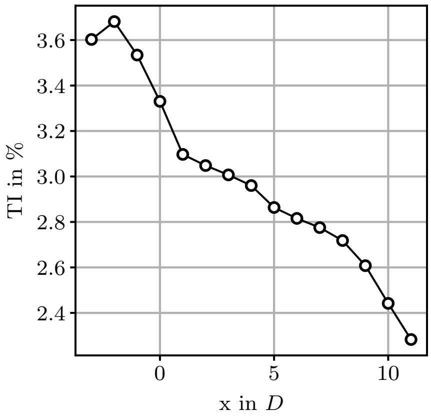

Figure 6.2: Turbulence intensity as a function of the downstream position. TI were computed along the center line of the domain.

As depicted in Figure 6.2, the turbulence dissipates significantly within the domain. It is expected that there is some loss of resolved turbulent kinetic energy in the flow. However, the reduction of more than approximately 50% compared to the turbulence of the synthetic turbulence box is considered large.
An attempt was therefore made to estimate dissipation analytically. In order to outline the influence of the mesh resolution and the domain size, the energy spectrum has been computed to see how much of the energy content in the turbulence is outside the resolved scales. The energy spectrum is approximated as a Karman spectrum, which is also used as a baseline spectrum for derivations of the Mann model (Mann, 1994).

Then it is investigated, what fraction of the energy lies in wave numbers corresponding to the length of the domain cross-section (lower wave-number limit) and the grid resolution (upper wave-number limit). The energy within these bounds has been compared to the overall energy in the spectrum and the relative loss in TI is shown in Table 6.2. This is only a qualitative analysis, as the cut-off of energy due to the mesh is likely not sharply at the indicated bounds of mesh and domain. Additionally, the Nyquist limit has not been accounted for. The spectrum is not scaled to a TI of $I = 5\%$ as only relative changes of the energy are investigated.

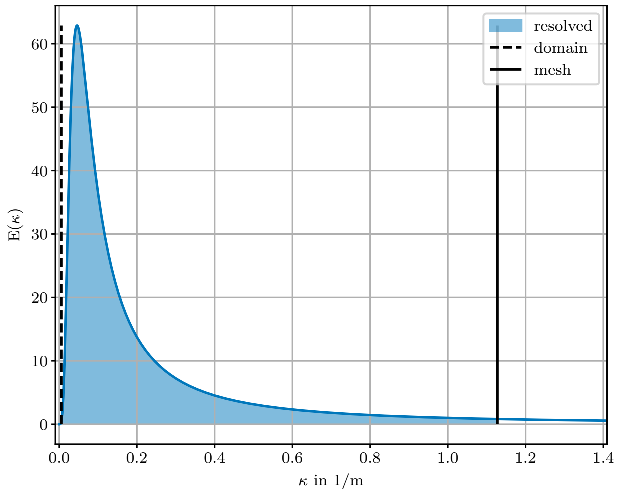

Figure 6.3: Energy spectrum of the turbulence box as a function of the wavenumber. The spectrum is approximated using the Karman-spectrum. The resolved energy between the cut-off due to mesh resolution and domain size are depicted. The energy losses are beyond these bounds.

It is shown that using these energy cut-off conditions, indeed a significant part of the energy is outside the bounds, with approximately 12.8% as shown in Table 6.2. However, this is not sufficient to explain the large energy dissipation found in the CFD simulations. Additionally, if this frequency cut-off would be the reason for the dissipation, it would be expected to find a larger contribution of decay at the inlet and then reach, to some extent, a more constant TI level after the initial energy dissipation.

It is finally found that for the use within the CFD framework YALES2, turbulence boxes need to be specifically adapted.

Parameter	Value
Domain size	6D
Mesh resolution	D/32
$ae^{2/3}$	1
l	33.6
Γ	3.9
Relative energy loss	12.8%

Table 6.2: Possible energy losses due to domain size and mesh resolution. The Mann model input parameters $ae^{2/3}$, l and Γ are taken from Table 3.5.

6.3 POD BASELINE - BASE COMPONENTS

Previously, only the stream-wise component of the POD (Figure 4.9) base has been analyzed in subsection 4.2.4 . However, the POD additionally yields two cross-stream components (horizontal and vertical), that are part of the POD basis. These are depicted in Figure 6.4 and Figure 6.5.

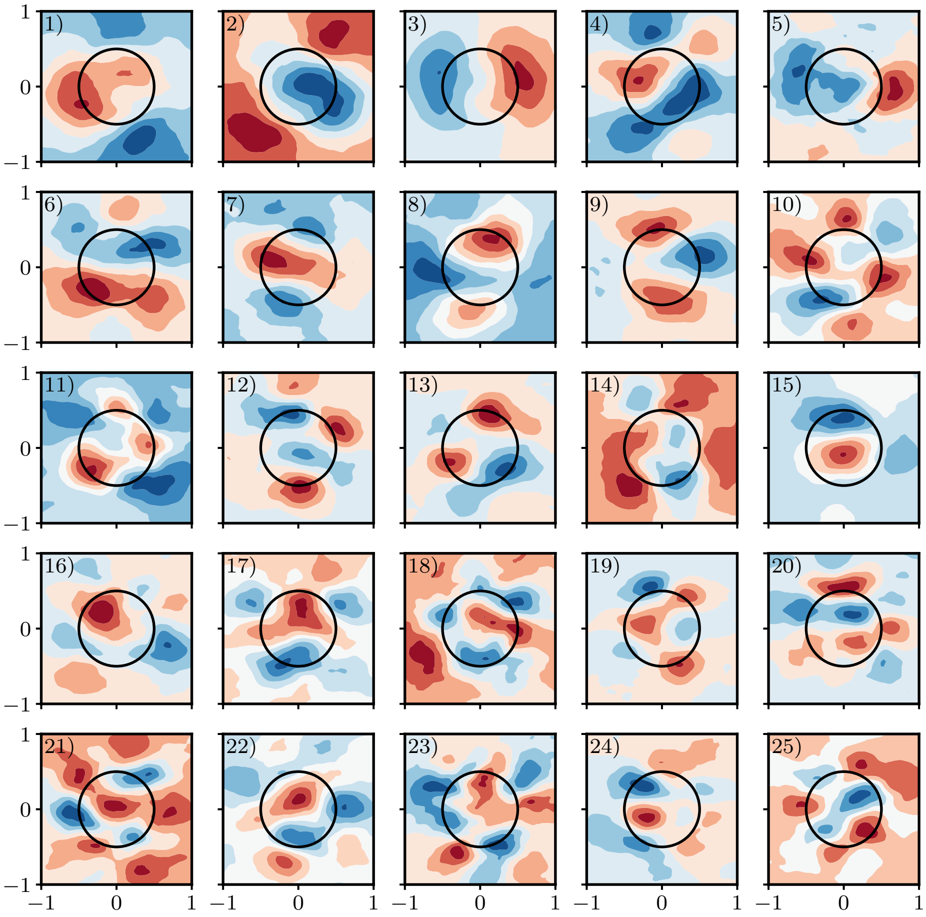

Figure 6.4: Horizontal cross-stream component u_y of the baseline POD. Only the first 25 modes of the global POD ortho-normal basis are depicted.

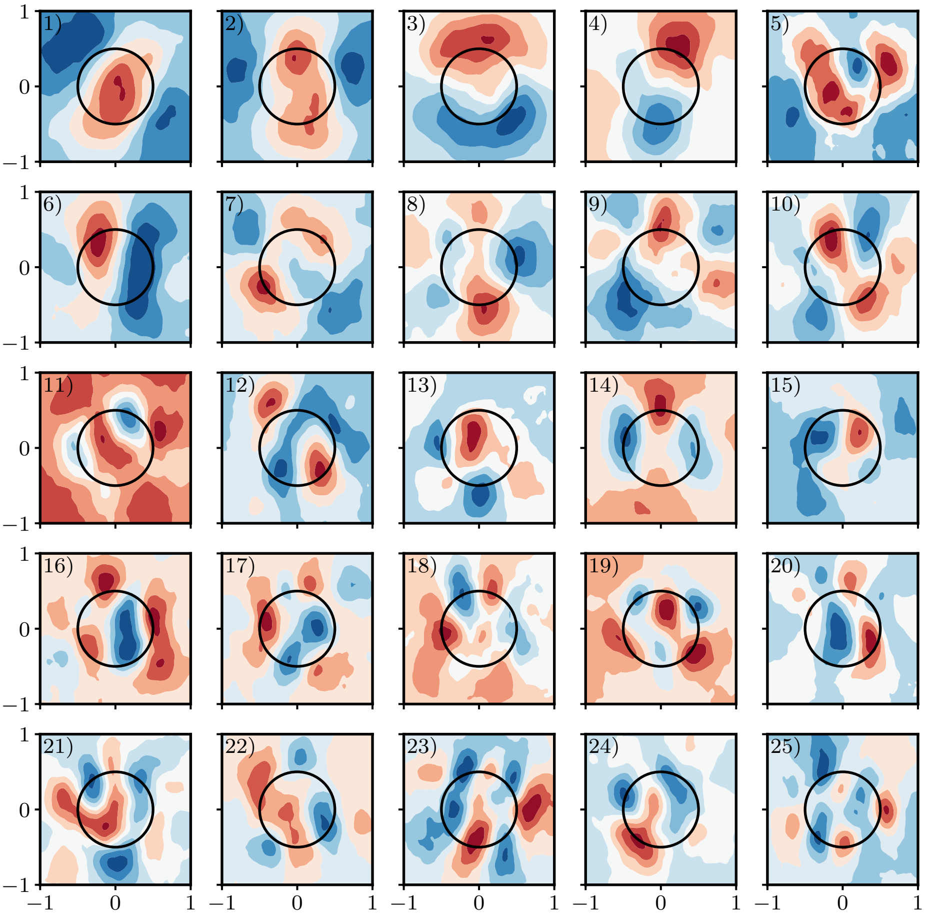

Figure 6.5: Vertical component u_z of the baseline POD. Only the first 25 modes of the global POD orthonormal basis

6.4 POD Basis for Low Numbers of Samples

Figure 6.6 depicts the stream-wise component u_x of the POD basis of the data set described in subsection 4.2.4 generated using long time spacing between samples leading to low sample numbers when compared to the baseline. A time spacing between samples of 246.76s is

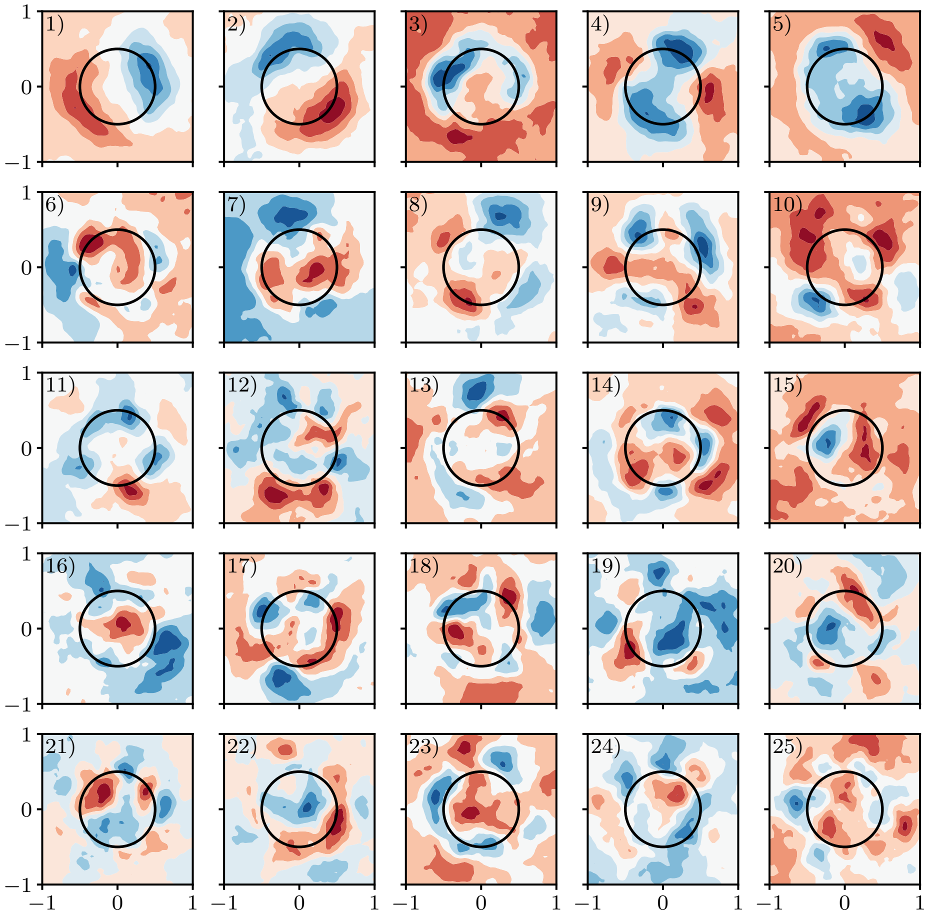

Figure 6.6: Stream-wise component u_x of the modal basis derived from long sample times of 245.76s (every 2^{12}th time step). Only the first 25 modes of the basis are depicted.

6.5 CORRELATIONS OF POD MODAL TIME SERIES

Within this report correlations between modal time series have been used heavily to characterize similarities and differences between the different flow cases. Generally, multiple modes and planes have been used to compute correlations. Threshold criteria are used to extract the overall tendencies. However, the full correlation data used to create the compressed correlation measure is depicted in the following.

6.5.1 COMPARISON OF DIFFERENT PLANES WITHIN ONE CASE

The correlations between identical modes and of different planes within individual flow cases have been performed, as discussed in subsection 4.2.6. Here, correlations of the modal time series of the last plane ($x = 10D$) and the upstream planes are depicted.

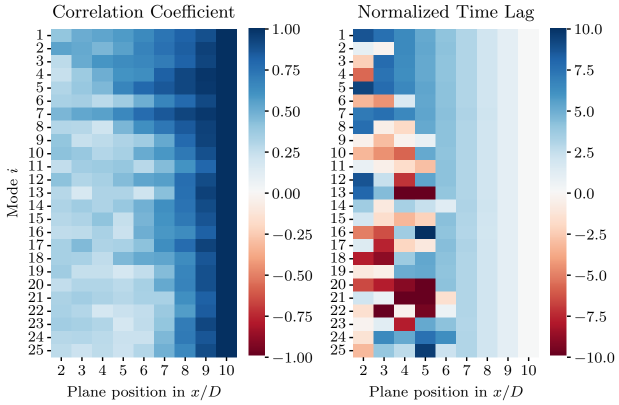

Figure 6.7: Correlations between the plane at $x = 10D$ and the upstream planes for the case $^{A}/_{D} = 0$, $St = 0$ (fixed), $I_{in} = 2.5\%$

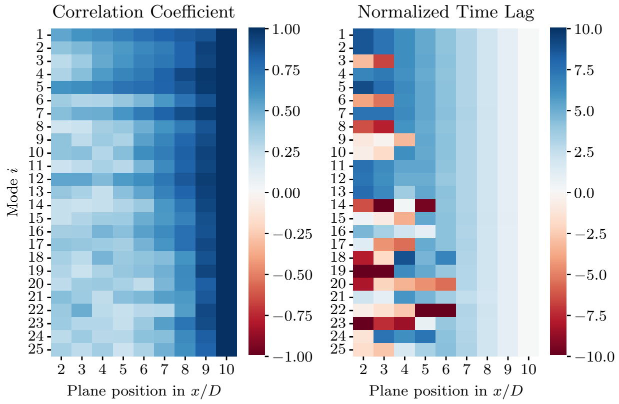

Figure 6.8: Correlations between the plane at $x = 10D$ and the upstream planes for the case $^{A}/_{D} = 0$ (fixed), $I_{in} = 5\%$

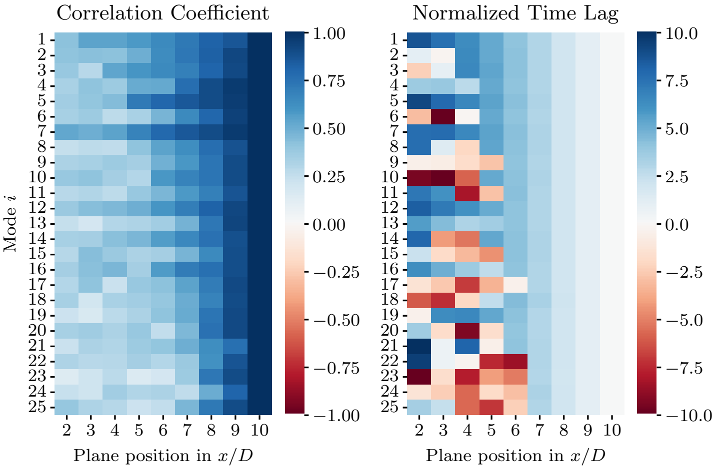

Figure 6.9: Correlations between the plane at $x = 10D$ and the upstream planes for the case $A/D = 0.02$, $St = 0.4$, $I_{in} = 2.5\%$

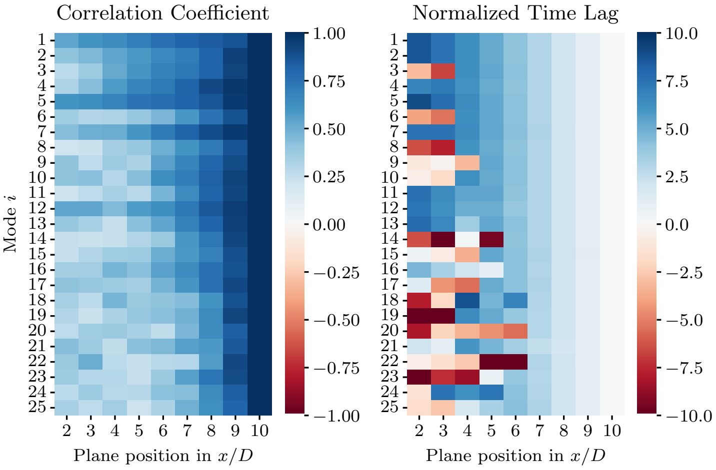

Figure 6.10: Correlations between the plane at $x = 10D$ and the upstream planes for the case $A/D = 0.02$, $St = 0.4$, $I_{in} = 5\%$

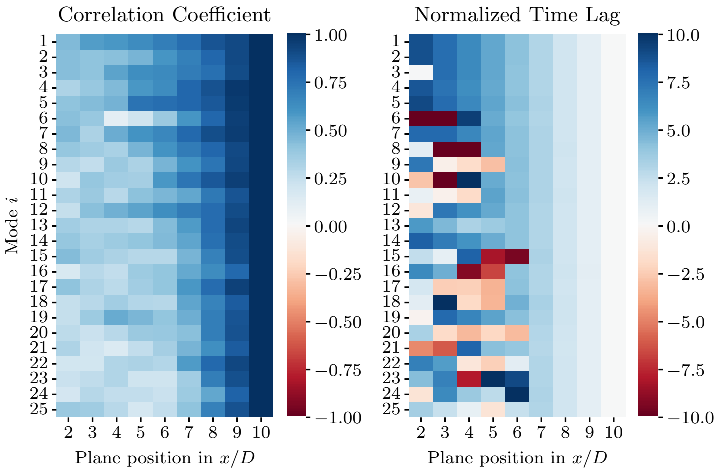

Figure 6.11: Correlations between the plane at $x = 10D$ and the upstream planes for the case $^A/_D = 0.04$, $St = 0.4$, $I_{in} = 2.5\%$

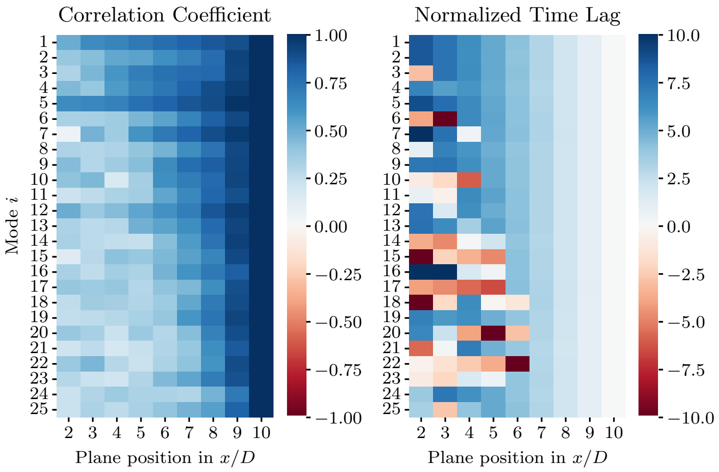

Figure 6.12: Correlations between the plane at $x = 10D$ and the upstream planes for the case $^A/_D = 0.04$, $St = 0.4$, $I_{in} = 5\%$

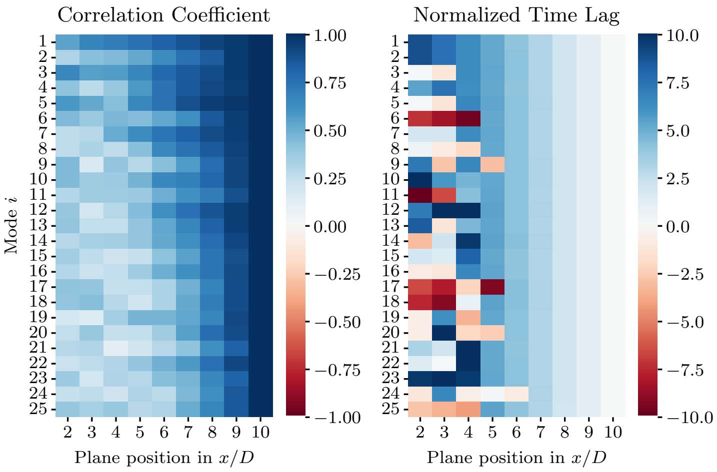

Figure 6.13: Correlations between the plane at $x = 10D$ and the upstream planes for the case $^{A}/_{D} = 0.08$, $St = 0.4$, $I_{in} = 2.5\%$

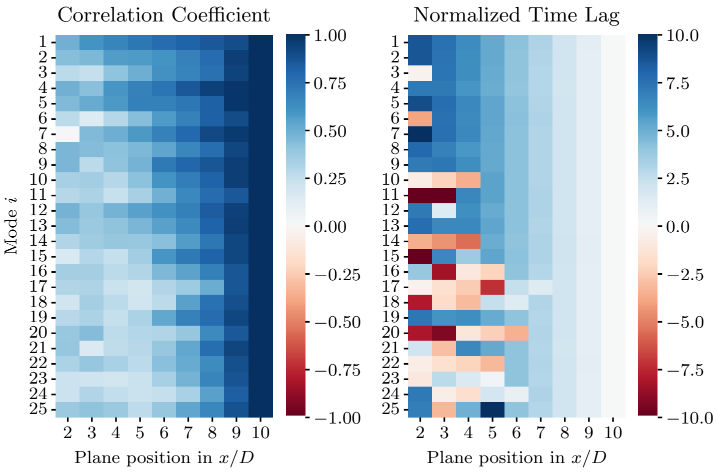

Figure 6.14: Correlations between the plane at $x = 10D$ and the upstream planes for the case $^{A}/_{D} = 0.08$, $St = 0.4$, $I_{in} = 5\%$

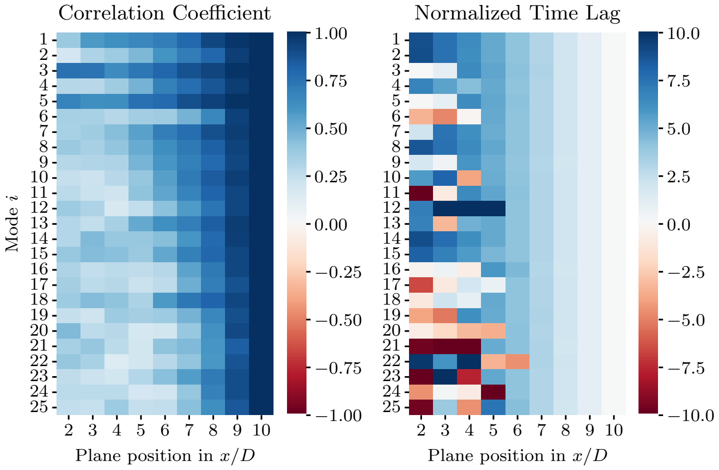

Figure 6.15: Correlations between the plane at $x = 10D$ and the upstream planes for the case $^{A}/_{D} = 0.16$, $St = 0.4$, $I_{in} = 2.5\%$

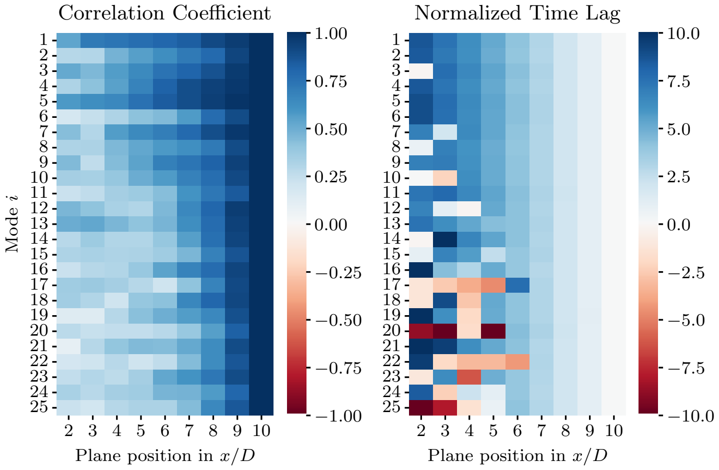

Figure 6.16: Correlations between the plane at $x = 10D$ and the upstream planes for the case $^{A}/_{D} = 0.16$, $St = 0.4$, $I_{in} = 5\%$

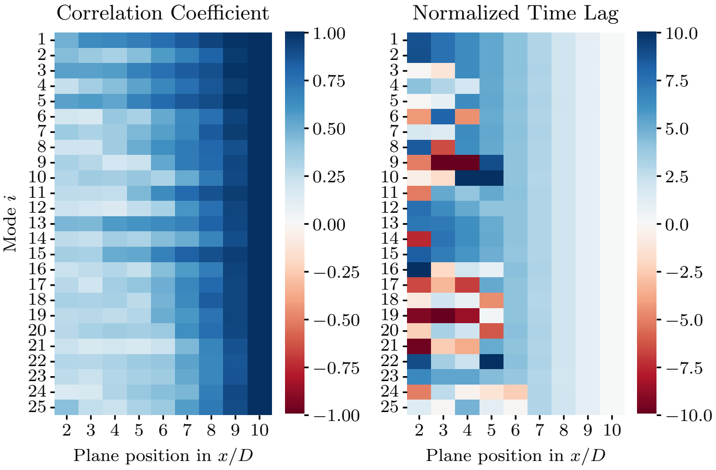

Figure 6.17: Correlations between the plane at $x = 10D$ and the upstream planes for the case $A/D = 0.32$, $St = 0.4$, $I_{in} = 2.5\%$

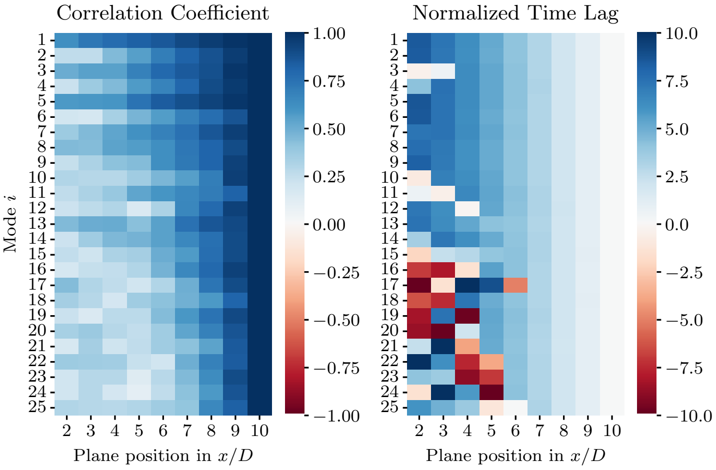

Figure 6.18: Correlations between the plane at $x = 10D$ and the upstream planes for the case $A/D = 0.32$, $St = 0.4$, $I_{in} = 5\%$

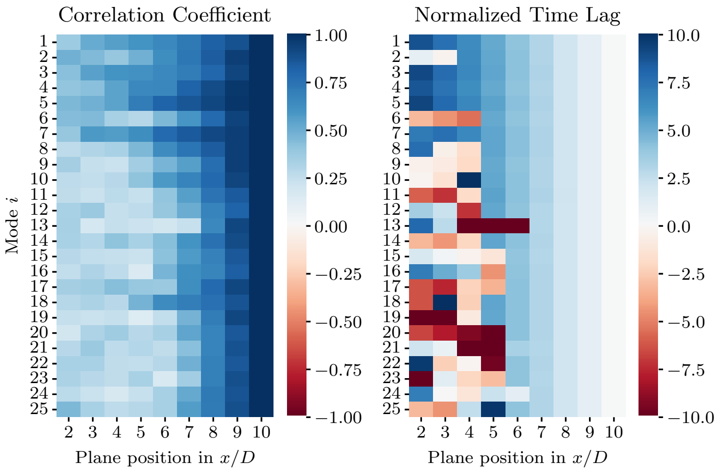

Figure 6.19: Correlations between the plane at $x = 10D$ and the upstream planes for the case ${}^{A}\!/_{D} = 0.04$, $St = 0.2$, $I_{in} = 2.5\%$

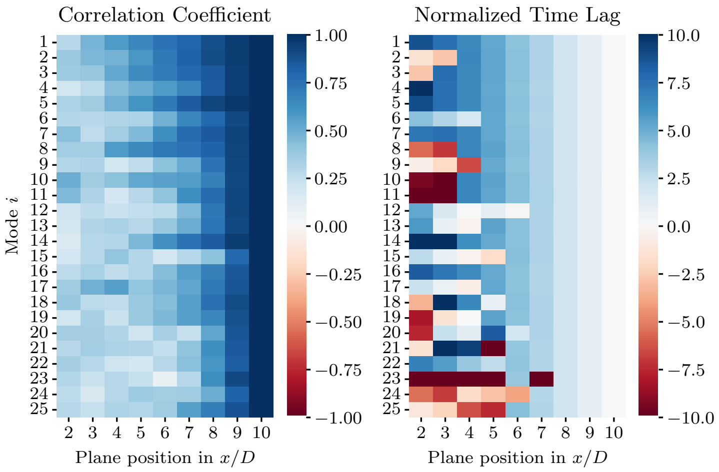

Figure 6.20: Correlations between the plane at $x = 10D$ and the upstream planes for the case ${}^{A}\!/_{D} = 0.04$, $St = 0.6$, $I_{in} = 2.5\%$

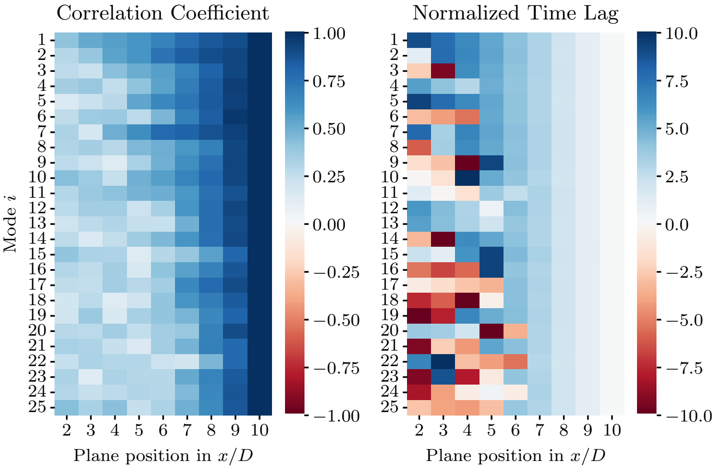

Figure 6.21: Correlations between the plane at $x = 10D$ and the upstream planes for the case $A/D = 0.04$, $St = 0.8$, $I_{in} = 2.5\%$

6.5.2 Comparison of Different Cases

As discussed in subsection 4.2.5, correlations of the modal time series of identical modes and planes between different flow cases have been computed in order to show the differences in the wake development for different variations of the motion parameters. Again, information from various results has been compressed using a threshold criterion. The full results that have been used to generate these compressed images are depicted in the following.

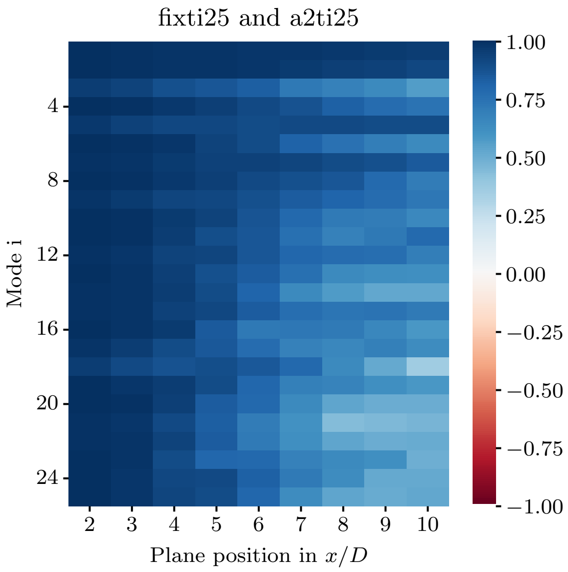

(a) Correlation between modal time series for identical plane and mode between the cases: fixed, $I_{in} = 2.5\%$ and ${}^{A}/{}_{D} = 0.02$, $St = 0.4$, $I_{in} = 2.5\%$

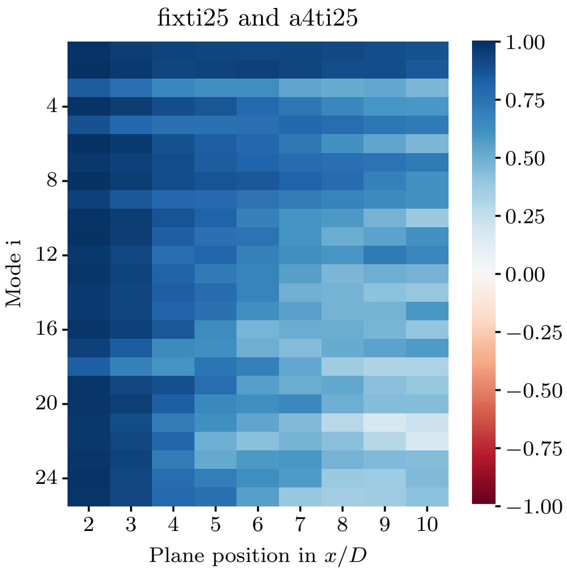

(b) Correlation between modal time series for identical plane and mode between the cases: fixed (${}^{A}/{}_{D} = 0$), $I_{in} = 2.5\%$ and ${}^{A}/{}_{D} = 0.04$, $St = 0.4$ $I_{in} = 2.5\%$

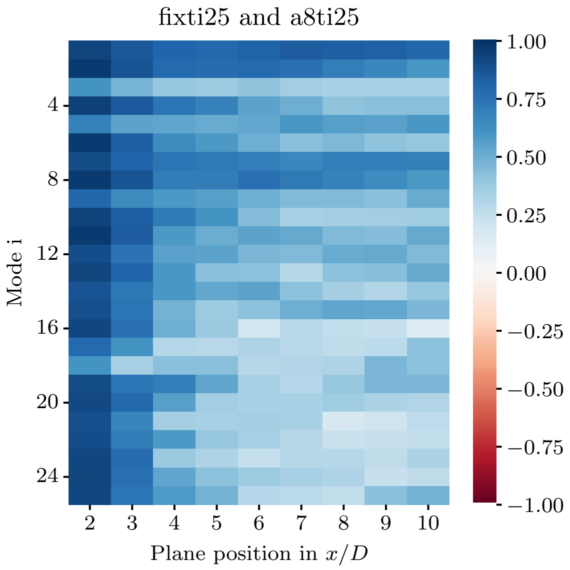

(a) Correlation between modal time series for identical plane and mode between the cases: fixed, $I_{in} = 2.5\%$ and $^A/_D = 0.08$, $St = 0.4$, $I_{in} = 2.5\%$

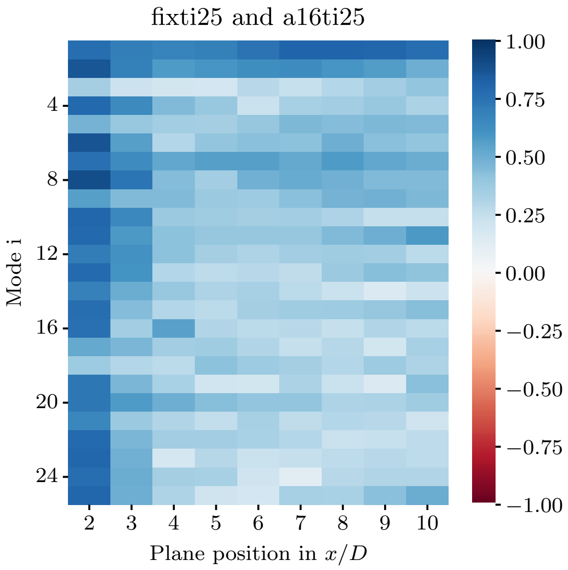

(b) Correlation between modal time series for identical plane and mode between the cases: fixed, $I_{in} = 2.5\%$ and $^A/_D = 0.16$, $St = 0.4$, $I_{in} = 2.5\%$

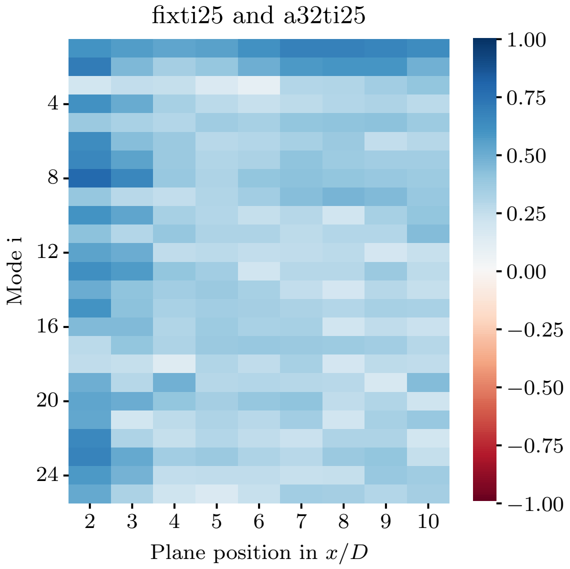

(a) Correlation between modal time series for identical plane and mode between the cases: fixed, $I_{in} = 2.5\%$ and $^A/_D = 0.32$, $St = 0.4$, $I_{in} = 2.5\%$

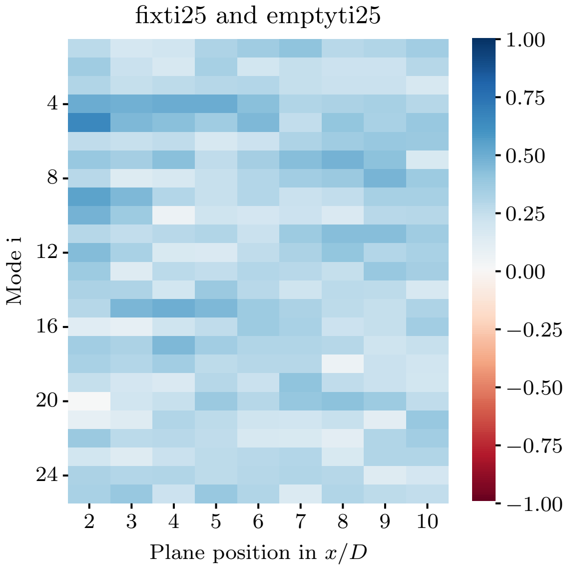

(b) Correlation between modal time series for identical plane and mode between the cases: fixed, $I_{in} = 2.5\%$ and empty channel flow at $I_{in} = 2.5\%$

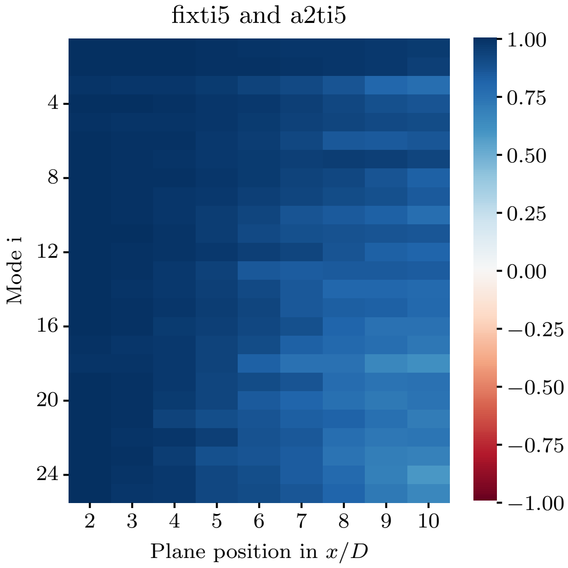

(a) Correlation between modal time series for identical plane and mode between the cases: fixed, $I_{in} = 5\%$ and $A/D = 0.02$, $St = 0.4$, $I_{in} = 5\%$

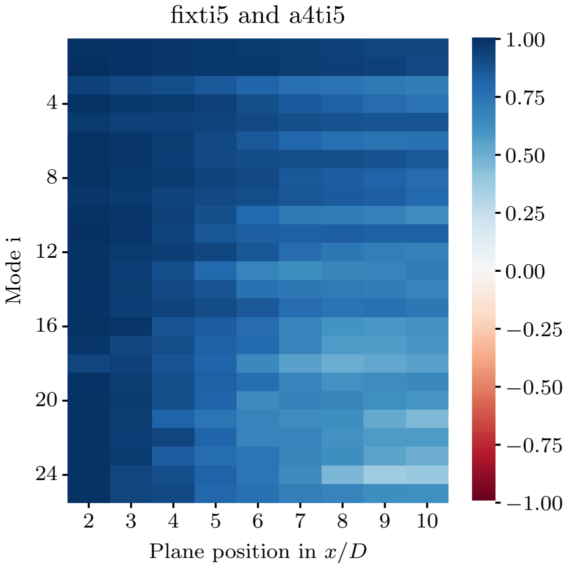

(b) Correlation between modal time series for identical plane and mode between the cases: fixed, $I_{in} = 5\%$ and $A/D = 0.04$, $St = 0.4$, $I_{in} = 5\%$

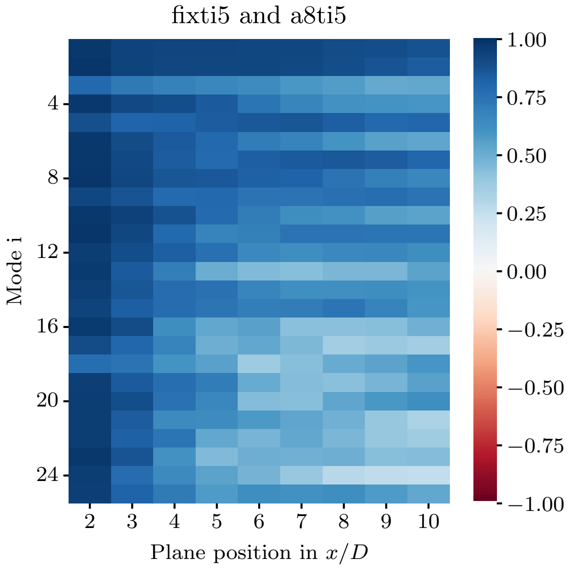

(a) Correlation between modal time series for identical plane and mode between the cases: fixed, $I_{in} = 5\%$ and $A/D = 0.08$, $St = 0.4$, $I_{in} = 5\%$

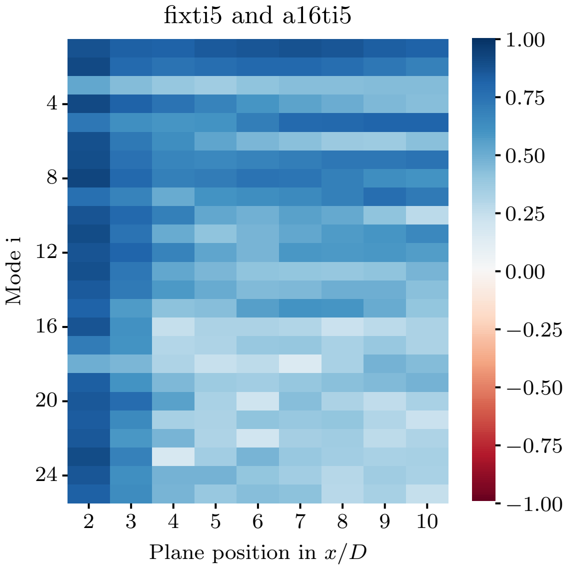

(b) Correlation between modal time series for identical plane and mode between the cases: fixed, $I_{in} = 5\%$ and $A/D = 0.16$, $St = 0.4$, $I_{in} = 5\%$

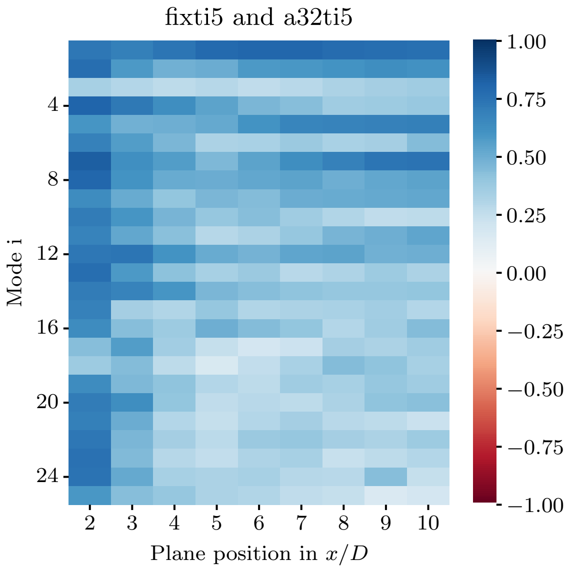

(a) Correlation between modal time series for identical plane and mode between the cases: fixed, $I_{in} = 5\%$ and $^{A}/_{D} = 0.32$, $St = 0.4$, $I_{in} = 5\%$

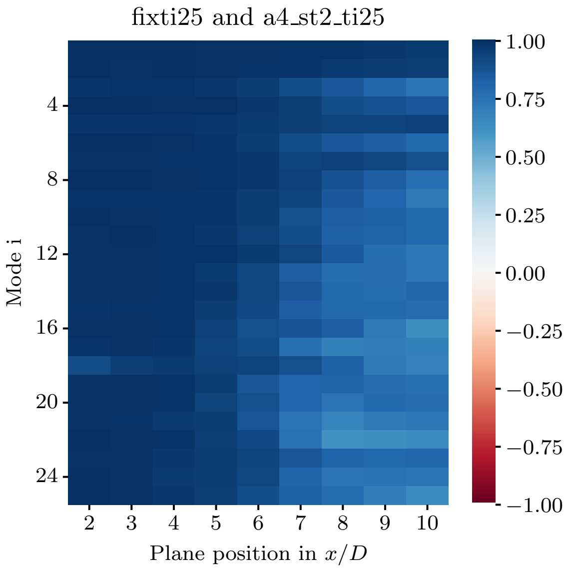

(b) Correlation between modal time series for identical plane and mode between the cases: fixed, $I_{in} = 2.5\%$ and $^{A}/_{D} = 0.04$, $St = 0.2$, $I_{in} = 2.5\%$

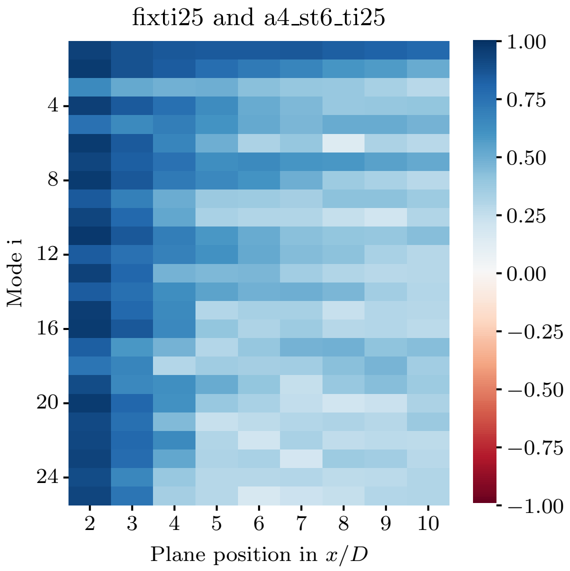

(a) Correlation between modal time series for identical plane and mode between the cases: fixed, $I_{in} = 2.5\%$ and $^{A}/_{D} = 0.04$, $St = 0.6$, $I_{in} = 2.5\%$

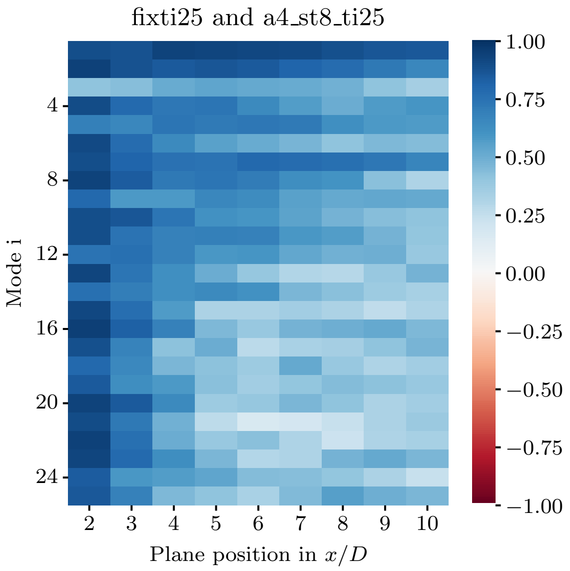

(b) Correlation between modal time series for identical plane and mode between the cases: fixed, $I_{in} = 2.5\%$ and $^{A}/_{D} = 0.04$, $St = 0.8$, $I_{in} = 2.5\%$

BIBLIOGRAPHY

Andersen, S. J. and J. P. Murcia Leon (2022). “Predictive and Stochastic Reduced-Order Modeling of Wind Turbine Wake Dynamics”. *Wind Energy Science* 7:5, pp. 2117–2133. ISSN: 2366-7443. DOI: `10.5194/WES-7-2117-2022`. (Visited on 10/24/2023).

Andersen, S. J., J. N. Sørensen, and R. Mikkelsen (2013). “Simulation of the Inherent Turbulence and Wake Interaction inside an Infinitely Long Row of Wind Turbines”. *Journal of Turbulence* 14:4, pp. 1–24. ISSN: 14685248. DOI: `10.1080/14685248.2013.796085`. (Visited on 09/19/2023).

Angelou, N., J. Mann, and C. Dubreuil-Boisclair (2023). “Revealing Inflow and Wake Conditions of a 6 MW Floating Turbine”. *Wind Energy Science* 8:10, pp. 1511–1531. ISSN: 23667443 (ISSN). DOI: `10.5194/wes-8-1511-2023`.

Bak, C., F. Zahle, R. Bitsche, T. Kim, A. Yde, L. C. Henriksen, A. Natarajan, and M. H. Hansen (2013). *Description of the DTU 10 MW Reference Wind Turbine*. Technical report I-0092.

Bastankhah, M. and F. Porté-Agel (2014). “A New Analytical Model for Wind-Turbine Wakes”. *Renewable Energy*. Special Issue on Aerodynamics of Offshore Wind Energy Systems and Wakes 70, pp. 116–123. ISSN: 0960-1481. DOI: `10.1016/j.renene.2014.01.002`. (Visited on 06/19/2024).

– (2016). “Experimental and Theoretical Study of Wind Turbine Wakes in Yawed Conditions”. *Journal of Fluid Mechanics* 806, pp. 506–541. ISSN: 0022-1120, 1469-7645. DOI: `10.1017/jfm.2016.595`. (Visited on 06/19/2024).

Belvasi, N., B. Conan, B. Schliffke, L. Perret, C. Desmond, J. Murphy, and S. Aubrun (2022). “Far-Wake Meandering of a Wind Turbine Model with Imposed Motions: An Experimental S-PIV Analysis”. *Energies* 15:20, p. 7757. ISSN: 1996-1073. DOI: `10.3390/en15207757`. (Visited on 04/10/2024).

Benard, P., A. Viré, V. Moureau, G. Lartigue, L. Beaudet, P. Deglaire, and L. Bricteux (2018). “Large-Eddy Simulation of Wind Turbines Wakes Including Geometrical Effects”. *Computers and Fluids* 173, pp. 133–139. ISSN: 00457930. DOI: `10.1016/j.compfluid.2018.03.015`. (Visited on 08/29/2023).

Celik, I., U. Ghia, P. Roache, C. Freitas, H. Coleman, and P. Raad (2008). “Procedure for Estimation and Reporting of Uncertainty Due to Discretization in CFD Applications”. *Journal of Fluids Engineering* 130:078001. ISSN: 0098-2202. DOI: `10.1115/1.2960953`. (Visited on 06/16/2024).

Combette, R. (2023). “Large-Eddy Simulation of a Floating Offshore Wind Turbine with Imposed Motion”. Delft: Delft University of Technology. URL: `https://repository.tudelft.nl/record/uuid:c89f950b-22f6-4fb3-a390-8039237f15f8`.

Davenport, A. G. (1965). “The Relationship of Wind Structure to Wind Loading”. *Proc. of Conf. on ’Wind Effects on Structures’, NPL, 1965, (ICWE-1)* 53.

DTU-Wind (2020). *HAWC Reference Models / Dtu-10mw-Rwt*. https://gitlab.windenergy.dtu.dk/hawc-reference-models/dtu-10mw-rwt. (Visited on 06/08/2024).

Epps, B. P. and A. H. Techet (2010). “An Error Threshold Criterion for Singular Value Decomposition Modes Extracted from PIV Data”. *Experiments in Fluids* 48:2, pp. 355–367. ISSN: 0723-4864, 1432-1114. DOI: 10.1007/s00348-009-0740-4. (Visited on 06/14/2024).

Gambuzza, S. and B. Ganapathisubramani (2023). “The Influence of Free Stream Turbulence on the Development of a Wind Turbine Wake”. *Journal of Fluid Mechanics* 963, A19. ISSN: 0022-1120, 1469-7645. DOI: 10.1017/jfm.2023.302. (Visited on 01/29/2024).

Gavish, M. and D. L. Donoho (2014). “The Optimal Hard Threshold for Singular Values Is 4/Sqrt (3)”. *IEEE Transactions on Information Theory* 60:8, pp. 5040–5053. ISSN: 0018-9448, 1557-9654. DOI: 10.1109/TIT.2014.2323359. (Visited on 06/14/2024).

Germano, M., U. Piomelli, P. Moin, and W. Cabot (1991). “A Dynamic Subgrid-Scale Eddy Viscosity Model”. *Physics of Fluids A* 3:7, pp. 1760–1765. ISSN: 0899-8213. DOI: 10.1063/1.857955.

Geuzaine, C. and J.-F. Remacle (2009). “Gmsh: A Three-Dimensional Finite Element Mesh Generator with Built-in Pre- and Post-Processing Facilities - Version 4.11.1”. *International Journal for Numerical Methods in Engineering* 79:11, pp. 1309–1331. (Visited on 01/25/2024).

Hodgkin, A., S. Laizet, and G. Deskos (2022). “Numerical Investigation of the Influence of Shear and Thermal Stratification on the Wind Turbine Tip-Vortex Stability”. *Wind Energy* 25:7, pp. 1270–1289. ISSN: 10954244 (ISSN). DOI: 10.1002/we.2728.

Hodgson, E. L., S. J. Andersen, N. Troldborg, A. M. Forsting, R. F. Mikkelsen, and J. N. S rensen (2021). “A Quantitative Comparison of Aeroelastic Computations Using Flex5 and Actuator Methods in LES”. *Journal of Physics: Conference Series* 1934:1, p. 012014. ISSN: 1742-6596. DOI: 10.1088/1742-6596/1934/1/012014. (Visited on 09/19/2023).

Hodgson, E. L., M. H. A. Madsen, and S. J. Andersen (2023). “Effects of Turbulent Inflow Time Scales on Wind Turbine Wake Behavior and Recovery”. *Physics of Fluids* 35:9, p. 95125. ISSN: 1070-6631. DOI: 10.1063/5.0162311. (Visited on 09/22/2023).

Houtin—Mongrolle, F., P. Benard, G. Lartigue, and V. Moureau (2021). “A Level-Set Framework for the Wind Turbine Wake Analysis: From High-Fidelity Unsteady Simulations to 1D Momentum Theory”. *Journal of Physics: Conference Series* 1934:1, p. 012011. ISSN: 1742-6588, 1742-6596. DOI: 10.1088/1742-6596/1934/1/012011. (Visited on 11/18/2023).

Hsu, S. A., E. A. Meindl, and D. B. Gilhousen (1994). “Determining the Power-Law Wind-Profile Exponent under Near-Neutral Stability Conditions at Sea”. *Journal of Applied Meteorology and Climatology* 33:6, pp. 757–765. ISSN: 1520-0450, 0894-8763. DOI: 10.1175/1520-0450(1994)033<0757:DTPLWP>2.0.CO;2. (Visited on 01/30/2024).

IEC (2005). *International Electrotechnical Commission Standard 61400-1*.

IEC Turbulence Simulator (2024). https://www.wasp.dk/software/wasp-engineering/iec-turbulence-simulator. (Visited on 06/27/2024).

Ivanell, S., R. Mikkelsen, J. Sørensen, and D. Henningson (2010). “Stability Analysis of the Tip Vortices of a Wind Turbine”. *Wind Energy* 13:8, pp. 705–715. ISSN: 10954244 (ISSN). DOI: 10.1002/we.391.

Kelly, M. (2018). “From Standard Wind Measurements to Spectral Characterization: Turbulence Length Scale and Distribution”. *Wind Energy Science* 3:2, pp. 533–543. ISSN: 2366-7451. DOI: 10.5194/wes-3-533-2018. (Visited on 01/30/2024).

Kerschen, G., J.-c. Golinval, A. F. Vakakis, and L. A. Bergman (2005). “The Method of Proper Orthogonal Decomposition for Dynamical Characterization and Order Reduction of Mechanical

Systems: An Overview”. *Nonlinear Dynamics* 41:1-3, pp. 147–169. ISSN: 0924-090X, 1573-269X. DOI: `10.1007/s11071-005-2803-2`. (Visited on 06/07/2024).

Kolmogorov, A. N. (1941). “The Local Structure of Turbulence in Incompressible Viscous Fluid for Very Large Reynolds’ Numbers”. *Akademiia Nauk SSSR Doklady* 30, pp. 301–305. ISSN: 0002-3264. (Visited on 01/25/2024).

– (1962). “A Refinement of Previous Hypotheses Concerning the Local Structure of Turbulence in a Viscous Incompressible Fluid at High Reynolds Number”. *Journal of Fluid Mechanics* 13:1, pp. 82–85. ISSN: 1469-7645, 0022-1120. DOI: `10.1017/S0022112062000518`. (Visited on 01/25/2024).

Kopperstad, K. M., R. Kumar, and K. Shoele (2020). “Aerodynamic Characterization of Barge and Spar Type Floating Offshore Wind Turbines at Different Sea States”. *Wind Energy* 23:11, pp. 2087–2112. ISSN: 1095-4244, 1099-1824. DOI: `10.1002/we.2547`. (Visited on 05/17/2024).

Kraushaar, M. (2011). “"Application of the Compressible and Low-Mach Number Approaches to Large-Eddy Simulation of Turbulent Flows in Aero-Engines"”. PhD thesis. Toulouse, France: University of Toulouse.

Larsen, G. C., H. A. Madsen, F. Bingöl, J. Mann, S. Ott, J. N. Sørensen, V. Okulov, N. Troldborg, M. Nielsen, K. Thomsen, T. J. Larsen, and R. Mikkelsen (2007). “Dynamic Wake Meandering Modeling”. *Risø National Laboratory, Denmark* Risoe-R No. 1607(EN). ISSN: 0106-2840.

Larsen, G. C., H. A. Madsen, K. Thomsen, and T. J. Larsen (2008). “Wake Meandering: A Pragmatic Approach”. *Wind Energy* 11:4, pp. 377–395. ISSN: 1099-1824. DOI: `10.1002/we.267`. (Visited on 06/19/2024).

Li, Y., A. Castro, T. Sinokrot, W. Prescott, and P. Carrica (2015). “Coupled Multi-Body Dynamics and CFD for Wind Turbine Simulation Including Explicit Wind Turbulence”. *Renewable Energy* 76, pp. 338–361. ISSN: 09601481 (ISSN). DOI: `10.1016/j.renene.2014.11.014`.

Li, Z., G. Dong, and X. Yang (2022). “Onset of Wake Meandering for a Floating Offshore Wind Turbine under Side-to-Side Motion”. *J. Fluid Mech* 934, p. 29. DOI: `10.1017/jfm.2021.1147`. (Visited on 10/24/2023).

Lilly, D. K. (1992). “A Proposed Modification of the Germano Subgrid-Scale Closure Method”. *Physics of Fluids A: Fluid Dynamics* 4:3, pp. 633–635. ISSN: 0899-8213. DOI: `10.1063/1.858280`. (Visited on 01/22/2024).

Mann, J. (1994). “The Spatial Structure of Neutral Atmospheric Surface-Layer Turbulence”. *Journal of Fluid Mechanics* 273, pp. 141–168. ISSN: 0022-1120, 1469-7645. DOI: `10.1017/S0022112094001886`. (Visited on 12/14/2023).

– (1998). “Wind Field Simulation”. *Probabilistic Engineering Mechanics* 13:4, pp. 269–282. ISSN: 02668920. DOI: `10.1016/S0266-8920(97)00036-2`. (Visited on 01/10/2024).

Marek, P., T. Grey, and A. Hay (2016). “A Study of the Variation in Offshore Turbulence Intensity around the British Isles”. *Proceedings of the Wind Europe Summit 2016*.

Martínez-Tossas, L. A. and C. Meneveau (2019). “Filtered Lifting Line Theory and Application to the Actuator Line Model”. *Journal of Fluid Mechanics* 863:NREL/JA-5000-72646. ISSN: 0022-1120. DOI: `10.1017/jfm.2018.994`. (Visited on 06/16/2024).

Messmer, T., M. Hölling, and J. Peinke (2024). “Enhanced Recovery Caused by Nonlinear Dynamics in the Wake of a Floating Offshore Wind Turbine”. *Journal of Fluid Mechanics* 984, A66. ISSN: 0022-1120, 1469-7645. DOI: `10.1017/jfm.2024.175`. (Visited on 04/25/2024).

Meyer Forsting, A., G. Pirrung, and N. Ramos García (2019). "A Vortex-Based Tip/Smearing Correction for the Actuator Line". *Wind Energy Science* 4, pp. 369–383. ISSN: 2366-7443. DOI: `10.5194/wes-4-369-2019`. (Visited on 06/16/2024).

Meyer Forsting, A. and N. Troldborg (2020). "Generalised Grid Requirements Minimizing the Actuator Line Angle-of-Attack Error". *Journal of Physics: Conference Series* 1618:5, p. 052001. ISSN: 1742-6588, 1742-6596. DOI: `10.1088/1742-6596/1618/5/052001`. (Visited on 06/17/2024).

Monin, A. S. and A. M. Obukhov (1954). "Basic Laws of Turbulent Mixing in the Surface Layer of the Atmosphere". *Contrib. Geophys. Inst. Acad. Sci. USSR*, 24.

Moureau, V., P. Domingo, and L. Vervisch (2011). "Design of a Massively Parallel CFD Code for Complex Geometries". *Comptes Rendus Mécanique* 339:2-3, pp. 141–148. ISSN: 16310721. DOI: `10.1016/j.crme.2010.12.001`. (Visited on 12/01/2023).

NASA (2024). *Examining Spatial (Grid) Convergence*. https://www.grc.nasa.gov/www/wind/valid/tutorial/spatconv.html. (Visited on 06/17/2024).

Pardo Garcia, L., B. Conan, S. Aubrun, L. Perret, T. Piquet, C. Raibaudo, and B. Schliffke (2022). "Experimental Analysis of the Wake Meandering of a Floating Wind Turbine under Imposed Surge Motion". In: *Journal of Physics: Conference Series*. Vol. 2265. Institute of Physics. DOI: `10.1088/1742-6596/2265/4/042003`.

Peña, A., S.-E. Gryning, and J. Mann (2010). "On the Length-Scale of the Wind Profile". *Quarterly Journal of the Royal Meteorological Society* 136:653, pp. 2119–2131. ISSN: 1477-870X. DOI: `10.1002/qj.714`. (Visited on 01/30/2024).

Poletto, R., T. Craft, and A. Revell (2013). "A New Divergence Free Synthetic Eddy Method for the Reproduction of Inlet Flow Conditions for LES". *Flow, Turbulence and Combustion* 91:3, pp. 519–539. ISSN: 1573-1987. DOI: `10.1007/s10494-013-9488-2`. (Visited on 06/25/2024).

Pollak, D. A. (2014). "Characterization of Ambient Offshore Turbulence Intensity from Analysis of Nine Offshore Meteorological Masts in Northern Europe". Technical University of Denmark. URL: `https://c2wind.com/f/content/daniel-pollak-edited.pdf`.

Porté-Agel, F., M. Bastankhah, and S. Shamsoddin (2019). "Wind-Turbine and Wind-Farm Flows: A Review". *Boundary-Layer Meteorology 2019 174:1* 174:1, pp. 1–59. ISSN: 1573-1472. DOI: `10.1007/S10546-019-00473-0`. (Visited on 09/19/2023).

Raibaudo, C., T. Piquet, B. Schliffke, B. Conan, and L. Perret (2022). "POD Analysis of the Wake Dynamics of an Offshore Floating Wind Turbine Model". In: *Journal of Physics: Conference Series*. Ed. by Watson S.J. and K. 1. TU Delft Wind Energy Institute Delft. Vol. 2265. Institute of Physics. DOI: `10.1088/1742-6596/2265/2/022085`.

Ramos-García, N., S. González Horcas, A. Pegalajar-Jurado, S. Kontos, and H. Bredmose (2022). "Investigation of the Floating IEA Wind 15-MW RWT Using Vortex Methods Part II: Wake Impact on Downstream Turbines under Turbulent Inflow". *Wind Energy* 25:8, pp. 1434–1463. ISSN: 10954244 (ISSN). DOI: `10.1002/we.2738`.

Richardson, L. F. and R. T. Glazebrook (1910). "IX. The Approximate Arithmetical Solution by Finite Differences of Physical Problems Involving Differential Equations, with an Application to the Stresses in a Masonry Dam". *Philosophical Transactions of the Royal Society of London. Series A, Containing Papers of a Mathematical or Physical Character* 210:459-470, pp. 307–357. DOI: `10.1098/rsta.1911.0009`. (Visited on 06/16/2024).

Sagaut, P. (2006). *Large Eddy Simulation for Incompressible Flows*. Third. Springer. ISBN: 978-3-540-26344-9.

Schliffke, B., S. Aubrun, and B. Conan (2020). "Wind Tunnel Study of a "Floating" Wind Turbine's Wake in an Atmospheric Boundary Layer with Imposed Characteristic Surge Motion". *Journal of Physics: Conference Series* 1618:6, p. 062015. ISSN: 1742-6596. DOI: `10.1088/1742-6596/1618/6/062015`. (Visited on 01/22/2024).

Schliffke, B., B. Conan, and S. Aubrun (2024). "Floating Wind Turbine Motion Signature in the Far-Wake Spectral Content – a Wind Tunnel Experiment". *Wind Energy Science* 9, pp. 519–532. DOI: `10.5194/wes-9-519-2024`.

Sebastian, T. and M. Lackner (2012). "Analysis of the Induction and Wake Evolution of an Offshore Floating Wind Turbine". *Energies* 5:4, pp. 968–1000. ISSN: 1996-1073. DOI: `10.3390/en5040968`. (Visited on 06/26/2024).

Sirovich, L. (1987). "Turbulence and the Dynamics of Coherent Structures Part I: Coherent Structures". *Quarterly of Applied Mathematics* 45:3, pp. 561–571. ISSN: 0033-569X. DOI: `10.1090/qam/910462`. JSTOR: `43637457`. (Visited on 01/23/2024).

Smagorinsky, J. (1963). "General Circulation Experiments with the Primitive Equations: I. The Basic Experiment". *Monthly Weather Review* 91:3, pp. 99–164. ISSN: 1520-0493, 0027-0644. DOI: `10.1175/1520-0493(1963)091<0099:GCEWTP>2.3.CO;2`. (Visited on 01/22/2024).

Sorensen, J. N., R. F. Mikkelsen, D. S. Henningson, S. Ivanell, S. Sarmast, and S. J. Andersen (2015). "Simulation of Wind Turbine Wakes Using the Actuator Line Technique". *Philosophical Transactions of the Royal Society A: Mathematical, Physical and Engineering Sciences* 373:2035. ISSN: 1364503X. DOI: `10.1098/RSTA.2014.0071`. (Visited on 09/12/2023).

Sørensen, J. N. and W. Z. Shen (2002). "Numerical Modeling of Wind Turbine Wakes". *Journal of Fluids Engineering* 124:2, pp. 393–399. ISSN: 0098-2202. DOI: `10.1115/1.1471361`. (Visited on 09/19/2023).

Taylor, G. I. (1938). "The Spectrum of Turbulence". *Proceedings of the Royal Society of London. Series A - Mathematical and Physical Sciences* 164:919, pp. 476–490. ISSN: 0080-4630, 2053-9169. DOI: `10.1098/rspa.1938.0032`. (Visited on 06/20/2024).

Troldborg, N., J. Sørensen, and R. Mikkelsen (2007). "Actuator Line Simulation of Wake of Wind Turbine Operating in Turbulent Inflow". In: *Journal of Physics: Conference Series*. Vol. 75. Institute of Physics Publishing. ISBN: 17426588 (ISSN). DOI: `10.1088/1742-6596/75/1/012063`.

Troldborg, N. (2009). "Actuator Line Modeling of Wind Turbine Wakes". PhD thesis.

Vermeer, L. J., J. N. Sørensen, and A. Crespo (2003). "Wind Turbine Wake Aerodynamics". *Progress in Aerospace Sciences* 39:6, pp. 467–510. ISSN: 0376-0421. DOI: `10.1016/S0376-0421(03)00078-2`. (Visited on 11/10/2023).

Wu, Y.-T. and F. Porté-Agel (2012). "Atmospheric Turbulence Effects on Wind-Turbine Wakes: An LES Study". *Energies* 5:12, pp. 5340–5362. ISSN: 19961073 (ISSN). DOI: `10.3390/en5125340`.

Xu, S., T. Zhuang, W. Zhao, and D. Wan (2023). "Numerical Investigation of Aerodynamic Responses and Wake Characteristics of a Floating Offshore Wind Turbine under Atmospheric Boundary Layer Inflows". *Ocean Engineering* 279. ISSN: 00298018 (ISSN). DOI: `10.1016/j.oceaneng.2023.114527`.

Zhou, Y., Q. Xiao, Y. Liu, A. Incecik, C. Peyrard, D. Wan, G. Pan, and S. Li (2022). "Exploring Inflow Wind Condition on Floating Offshore Wind Turbine Aerodynamic Characterisation and Platform Motion Prediction Using Blade Resolved CFD Simulation". *Renewable Energy* 182, pp. 1060–1079. ISSN: 09601481 (ISSN). DOI: `10.1016/j.renene.2021.11.010`.